

Zinc oxide thin films nanostructures metal organic chemical vapor deposition

Tan, Swee Tiam

2007

Tan, S. T. (2007). Zinc oxide thin films nanostructures metal organic chemical vapor deposition. Doctoral thesis, Nanyang Technological University, Singapore.

<https://hdl.handle.net/10356/3516>

<https://doi.org/10.32657/10356/3516>

Nanyang Technological University

Downloaded on 20 Mar 2024 18:40:33 SGT

Zinc Oxide Thin Films and Nanostructures by Metal Organic Chemical Vapor Deposition

Tan Swee Tiam

School of Electrical & Electronic Engineering

A thesis submitted to the Nanyang Technological University
in fulfillment of the requirement for the degree of
Doctor of Philosophy

2007

To my beloved parents
Tan Cheng Hai and Kong Sit Huang.

ACKNOWLEDGMENTS

I would like to take this opportunity to thank to my dissertation advisors Prof. Sun Xiaowei, Dr. Zhang Xinhai, and Dr. Lo Guoqiang and dissertation instructors Prof. Chua Soo Jin and Dr. Chen Baijun profusely for their guidance and advices during my research. Their enthusiasm and willingness to teach have made the research such a wonderful and an enriching experience. More importantly, under their supervision, I have built up the research interest and analytic ability, where I had my first taste of research and development.

I would like to thank all the staffs and students at the Nanoelectronics Lab I (formally known as Ion Beam Processing Lab), Institute of Materials and Research Engineering, Institute of Microelectronics and Polymer Lab. Special thank to Prof. Fan Weijun, Prof. Xu Chunxiang, Prof. Hu Xiao, and Dr. Yu Zhigen for their insight views and fruitful discussion; to Dr. Ji Xiaohong, Dr. Li Junfeng, Dr. Zhong Weihua, Dr. Li Zhiqing, Dr. Zhao Zhiwei, Dr. Lee Chea Beng, Liu Yanzun, Eunice Leong, Anna Yong, and all the friends from Nanoelectronics Lab I for their friendship, encouragement, inspirational discussions, and all the different kinds of assistance they gave me.

I would also like to extend my gratitude to Institute of Materials and Research Engineering, Singapore, for the postgraduate scholarship and the characterization facilities.

Finally, I wish to convey my profound gratitude to my beloved family for their never-ending moral support and patience during my studies at NTU. Particularly, I am greatly indebted to my parents, to whom I dedicate this thesis.

TABLE OF CONTENTS

ACKNOWLEDGMENTS	I
TABLE OF CONTENTS.....	II
SUMMARY	IV
LIST OF FIGURES	VII
LIST OF TABLES.....	XIII
ABBREVIATIONS	XIV
CHAPTER 1 INTRODUCTION	1
1.1 MOTIVATION.....	1
1.1.1 Semiconductor revolution.....	1
1.1.2 Potential market for wide bandgap semiconductors	4
1.1.3 Why ZnO?.....	6
1.1.3.1 Emission efficiency.....	7
1.1.3.2 Material and fabrication cost	9
1.1.3.3 Si-CMOS compatibility	10
1.1.3.4 Substrate availability / chemical & radiation resistance	10
1.1.4 Overview of ZnO	11
1.1.4.1 Bipolar doping of ZnO.....	11
1.1.4.2 Hydrogen in ZnO	13
1.1.5 Current status of ZnO research	14
1.2 OBJECTIVES	16
1.3 MAJOR CONTRIBUTIONS.....	17
1.4 ORGANIZATION.....	18
CHAPTER 2 ZNO QUANTUM DOTS EMBEDDED THIN FILMS BY MOCVD	20
2.1 BACKGROUND.....	20
2.2 MOCVD SYSTEM.....	23
2.3 ZNO QUANTUM DOTS EMBEDDED FILMS	25
2.3.1 MOCVD Reactor Setup	25
2.3.2 Experiment.....	26
2.3.3 Results and Discussion	26
2.3.4 Summary	38
2.4 QUANTUM CONFINEMENT OF ZNO QUANTUM DOTS EMBEDDED FILMS.....	39
2.4.1 Background	39
2.4.2 Experiment.....	39
2.4.3 Results and Discussion	41
2.4.4 Post-growth Thermal Annealing on ZnO QDs Embedded Films.....	46
2.4.5 Growth Mechanism of ZnO QDs Embedded Films	47
2.4.6 Summary	49
CHAPTER 3 HIGHLY C-AXIS OERIENTED ZNO THIN FILMS BY MOCVD	50

3.1	REACTOR DESIGN INVESTIGATION.....	50
3.2	HIGHLY C-AXIS ORIENTED ZNO THIN FILMS	52
3.2.1	Experiment.....	52
3.2.2	Results and Discussion	53
3.2.3	Summary	54
3.3	POST-GROWTH THERMAL ANNEALING ON HIGHLY C-AXIS ORIENTED ZNO THIN FILMS.....	56
3.3.1	Experiment.....	57
3.3.2	Results and Discussion	58
3.3.3	Summary	74
CHAPTER 4 REALIZATION OF P-TYPE ZNO THIN FILMS.....		75
4.1	BACKGROUND.....	75
4.1.1	Dopant choice I: Group-I elements (Li, Na, K).....	76
4.1.2	Dopant choice II: Group-V elements (N, P, As, Sb)	76
4.1.3	Self-compensation process in ZnO	78
4.2	P-TYPE NOMINAL UNDOPED AND N-DOPED POLYCRYSTALLINE ZNO THIN FILMS.....	82
4.2.1	Experiment.....	82
4.2.2	Results and Discussion	83
4.2.3	Summary	89
4.3	REVEALING P-TYPE IN CARBON-DOPED ZNO THIN FILMS.....	90
4.3.1	Experiment.....	90
4.3.2	Results and Discussion	91
4.3.3	Summary	99
CHAPTER 5 ZNO SELF-ASSEMBLED NANOSTRUCTURES.....		100
5.1	BACKGROUND.....	100
5.2	EXPERIMENT.....	101
5.3	RESULTS AND DISCUSSION.....	102
5.4	SUMMARY.....	112
CHAPTER 6 CONCLUSIONS AND RECOMMENDATIONS		113
6.1	CONCLUSIONS.....	113
6.2	RECOMMENDATIONS FOR FUTURE RESEARCH	115
JOURNAL PUBLICATIONS		118
CONFERENCE PRESENTATIONS		120
AWARDS		121
BIBLIOGRAPHY.....		122

SUMMARY

In this dissertation, the investigation on growth and post-growth annealing treatment of ZnO thin films, deposited by a home-made metal organic chemical vapor deposition (MOCVD), is presented. The growth of the ZnO thin films was studied with various growth parameters and reactor designs. With the first generation of MOCVD, the fabricated ZnO thin films consist of amorphous and crystalline phases. The optical bandgap of the nominal undoped ZnO thin films grown at low temperature was blue-shifted from 3.25 to 4.06 eV, which was attributed to the amorphous ZnO absorption. Furthermore, ZnO quantum dots (QDs) embedded films could be obtained by introducing large amount of precursors during the growth. The size of the QDs, estimated using high-resolution transmission electron microscopy (HRTEM), was found to be ~3-12 nm. The quantum confinement effect of ZnO QDs embedded films was evidently observed and validated in the broadening of near-band-edge emission that extended to 3.6 eV. The dependency of QDs bandgap on dot size and the growth mechanism were discussed in detail.

The pre-reaction of precursors in gaseous phase has greatly influenced the ZnO thin films deposited with the original reactor. In fact, with the appropriate flow rate of precursors and growth temperature, ZnO QDs embedded films were successfully demonstrated. In order to obtain high quality film, the MOCVD reactor and growth process have been systematically modified to eliminate the pre-reaction of the precursors. Using the modified reactor and growth process, highly c-axis oriented polycrystalline ZnO thin films were obtained. The quality of the fabricated ZnO thin films was found to be comparable to that of single crystalline ZnO thin films.

Thermal annealing is an important post-growth treatment in semiconductor industry. In this dissertation, detailed investigation on post-growth annealing was

carried out on the MOCVD-grown ZnO thin films. The nanoscale-sized sheets with random orientation on as-grown films changed to three-dimensional nanoneedles upon annealing. A coarsening kinetics developed by Lifshitz and Slyozov, and Wagner was used to estimate the activation energy of the coarsening process. The activation energy of the Ostwald ripening in ZnO thin films was estimated for the first attempt to be 1.33 eV, which is likely to be governed by Zn atom migration.

It is well known that the difficulty in getting *p*-type ZnO thin films has prevented the realization of ZnO-based opto-electronic devices. In this dissertation, substantial efforts have been devoted to the investigation on the intrinsic defects in ZnO thin films. Nominal undoped and N-doped *p*-type conduction ZnO thin films were successfully fabricated by controlling the Zn:O ratio in the range of 0.05 to 0.2. The obtained *p*-type ZnO thin films grown by the original reactor exhibit good electrical and optical properties but have relatively poor crystallinity. As a result, the investigation on the defect physics became complicating and challenging. Nevertheless, the demonstration of nominal undoped and N-doped ZnO thin films provides a guide for future work. Other than the as-grown *p*-type ZnO thin films, *p*-type nominal undoped ZnO thin film was obtained by post-growth thermal annealing. The unintentional carbon doping in MOCVD grown ZnO is unavoidable as it comes from the zinc precursor during MOCVD process. The doped carbon, which has been confirmed by secondary ion mass spectrometry (SIMS), immobilized the oxygen at the interstitial sites in ZnO thin films after annealing, which resulting in *p*-type conduction. By x-ray photoelectron spectroscopy (XPS), the O-C-O complex and oxygen interstitials were confirmed. The cryogenic photoluminescence of the carbon-doped *p*-type ZnO thin film showed an additional peak, which was attributed to neutral acceptor bound exciton located at 3.3564 eV.

As seen from a surge of a relevant number of publications, nanostructured materials have attracted considerable interest recently due to their unique and novel properties over their bulk counterparts. In this dissertation, the synthesis of ZnO hollow spheres and hexagonal stacking disks is presented. The growth was investigated as a function of time, and the peculiar structures were obtained in a narrow window of a near-zero oxygen partial pressure. The largest hollow sphere has a diameter up to 20 μm with a shell thickness of ~ 200 nm formed by nanocrystals or nanodisks. HRTEM shows that the hexagonal stacking disks are surrounded by a few nanometer-thick metallic Zn. The formation of hollow spheres and stacking disks was attributed to the accumulation and dissociation of diethylzinc through beta hydride elimination process in the near-zero oxygen partial pressure.

In summary, this dissertation addresses the growth and characterization of ZnO thin films and nanostructures by a home-made MOCVD. The work has provided some insights for designing a better MOCVD system and hence realizing the high-quality *p*-type ZnO thin films for opto-electronic devices.

LIST OF FIGURES

Figure 1-1 (a) From left to right, John Bardeen, William Shockley, and Walter Brattain at Bell Laboratories. (b) The first point contact germanium bipolar transistor.	1
Figure 1-2 Room-temperature bandgap energy versus lattice constant of common elemental and binary compound semiconductors. ⁴	2
Figure 1-3 Luminence efficiency versus emitted wavelength of visible LEDs made from phosphide, arsenide and nitride compound semiconductors. ⁴	3
Figure 1-4 Potential market for ZnO-based materials. ⁷	4
Figure 1-5 NASDAQ Market site at night. It consists of almost 19 millions high brightness LEDs.....	5
Figure 1-6 Stone Bridge at Regensburg, Germany with about 22,000 red and white LEDs.	5
Figure 1-7 (a) World's first violet LED on GaN:Mg. (b) Commercial GaInN/GaN blue LEDs array manufactured by Nakamura <i>et al.</i> , Nichia Corporation. ⁴	6
Figure 1-8 Lattice constant of ZnO, GaN and theirs related alloys. ⁴⁹	8
Figure 1-9 Energy bandgaps, lattice constants and crystal structures of selected II-VI compounds. ⁵⁰	8
Figure 1-10 Price of Indium. (Extracted from Compound Semiconductor magazine) ⁵¹	9
Figure 1-11 Wurtzite, hexagonal close packed (HCP) structure of ZnO.....	11
Figure 1-12 (a) Possible incorporation of hydrogen in ZnO. BC indicates the bond-center sites, and AB indicates the anti-bonding sites. (b) Relaxed atomic positions of hydrogen and host atoms in the BC _⊥ configuration. Ideal lattice positions without hydrogen incorporation are shown in dotted lines. ⁶⁵	13
Figure 2-1 Number of papers on MOCVD grown ZnO as a function of time. ¹⁰⁸	22
Figure 2-2 MOCVD system, consists of two metal organic sources (DMZn and TMGa), a gas oxidizer injection and a background gas line.	24
Figure 2-3 (a) Home-made MOCVD system, (b) Vertical reactor chamber and (c) MO bubbler in a coolant bath.....	24

Figure 2-4 Initial MOCVD reactor design. DMZn (carry by N ₂) and O ₂ gases were deliberately designed to flow parallel towards the substrates.....	25
Figure 2-5 XRD profiles of ZnO thin films fabricated on quartz substrates at various temperatures from (a) 200 to 350°C, (b) 400 to 500°C with an increment of 50°C.	27
Figure 2-6 XRD profiles of ZnO thin films fabricated on quartz substrates at 350°C and subsequently annealed at 500°C for 10 minutes.	29
Figure 2-7 Williamson-Hall plots for as-grown and annealed ZnO thin films.....	30
Figure 2-8 AFM images of ZnO thin films grown on quartz substrates at (a) 200°C, (b) 250°C, (c) 300°C, (d) 350°C, (e) 400°C, (f) 450°C, (g) 500°C, and (h) 350°C and annealing at 500°C for 10 minutes. The corresponding rms roughness of the films is indicated in the figure.....	31
Figure 2-9 Transmission spectra for the ZnO thin films fabricated on quartz substrates at various temperatures, (a) 200°C, (b) 250°C, (c); 300°C, (d) 350°C, (e) 400°C, (f) 450°C, (g) 500°C, (h) grown at 350°C and annealed at 500°C for 10 minutes.....	32
Figure 2-10 Plot of $(\alpha h\nu)^2$ versus photon energy for the ZnO thin films fabricated on quartz substrates at various temperatures, (a) 200°C, (b) 250°C, (c) 300°C, (d) 350°C, (e) 400°C, (f) 450°C, (g) 500°C, (h) grown at 350°C and annealed at 500°C for 10 minutes.	33
Figure 2-11 Room temperature PL spectra of the ZnO thin films fabricated on quartz substrates at various temperatures, (a) 200°C; (b) 250°C; (c) 300°C; (d) 350°C; (e) 400°C; (f) 450°C; (g) 500°C and (h) 350°C and annealing at 500°C for 10 minutes are shown.	36
Figure 2-12 Plot of $E_{(gap,nanocrystal)}$ obtained from PL measurement versus the nanocrystal radius R for ZnO thin films grown at various temperatures (○) and a theoretical fit using Eq. (2.5).	37
Figure 2-13 XRD profiles of (a) highly c-axis oriented ZnO thin film and (b) ZnO QDs embedded film.....	41
Figure 2-14 HRTEM images with (a) high magnification and (b) lower magnification of the ZnO QDs embedded film fabricated on Si substrates.....	42

Figure 2-15 Histogram of ZnO QDs distribution measured from Figure 2-14 (b). The dashed curve is the Gaussian fit of the ZnO QDs distribution.	42
Figure 2-16 PL spectra of (a) highly c-axis oriented ZnO thin film and (b) ZnO QDs embedded film measured at temperature of 80 K. The inset shows the room temperature PL of the QDs embedded film.....	43
Figure 2-17 Room temperature PL of QDs embedded films annealed at 800°C for (b) 10, (c) 30, (d) 60, and (e) 90 s, respectively. Room temperature PL of as-grown ZnO QDs embedded film is shown in (a) for reference.	47
Figure 2-18 Growth mechanism of the ZnO QDs embedded film. (a) Arriving of the precursors on the hot substrate. (b) Pre-reaction of the precursors facilitates the formation of nanocrystals, and in turn incorporates into the ZnO thin film.	48
Figure 3-1 Reactor with different design of precursors flow configuration, (a) original, (b) modification #1, and (c) modification #2 configuration.....	50
Figure 3-2 XRD (left) and PL (right) of ZnO grown on sapphire substrates by (a) original, (b) modification #1, and (c) modification #2 reactor design.....	51
Figure 3-3 Typical Properties of highly c-axis oriented ZnO thin films grown by MOCVD. (a) XRD profile with an inserted enlarged spectrum of (0002) peak; (b) Room temperature PL spectrum; (c) Transmission spectrum with an inserted absorption spectrum; and (d) AFM morphology on the ZnO thin films.	53
Figure 3-4 SEM topographs of (a) as-grown ZnO thin films and subsequently annealed at (b) 600°C, (c) 700°C, (d) 800°C, and (e) 900°C. The topographs at the left hand side show the topography of the surfaces while those at the right hand side show the topographs taken with a tilted angle of 45°. Arrowheads in (e) show the necks connecting two islands. All the scale bars are 200 nm in length.	59
Figure 3-5 2 μm \times 1 μm AFM topographs of (a) as-grown ZnO thin films and subsequently annealed at (b) 600°C, (c) 700°C, (d) 800°C, and (e) 900°C. All the topographs share the same color scare bar with the maximum height of 300 nm and the corresponding rms roughness of the films is indicated in the figure.	61

Figure 3-6 XRD profiles of the as-grown and annealed ZnO thin films. The (0002) peak position and its FWHM were recorded in the figure.....	62
Figure 3-7 Cartoons of mass transport mechanisms of coalescence phenomenon. (a) Ostwald ripening, (b) sintering, and (c) cluster migration.	64
Figure 3-8 Crystallite size distribution of the as-grown and annealed ZnO thin films estimated from SEM, and fitted with a Gaussian curve. The weighted average of grain diameter (\bar{d}) and particle density (n) of the samples were shown in the figure.....	67
Figure 3-9 Scaled PSD of the samples annealed at 600, 700, and 800°C.....	68
Figure 3-10 Plot of logarithm of $T(\bar{d}_t^3 - \bar{d}_0^3)$ vs $1/T$, and fitted with a line. The E_a yield from the slope is 1.33 eV.	69
Figure 3-11 Room temperature PL spectra of as-grown and annealed ZnO thin films. Inset is the plot of NBE to DLE ratio and FWHM versus annealing temperature.....	72
Figure 4-1 LDA defect formation enthalpies are shown in lines as a function of the Fermi energy E_F at the zinc-rich ($\mu_{Zn}=0$) and oxygen-rich ($\mu_{Zn}=-3.1$ eV) limits, respectively. The charge states of the defects are shown as – 2, -1, 0, and +2. Defect transition energies are shown as solid dots. ⁵⁹	79
Figure 4-2 Carrier concentration, Hall mobility, and resistivity of ZnO thin films as a function of Zn:O molar ratio. Filled symbol sample was grown with 5 sccm of N ₂ O.....	83
Figure 4-3 SIMS profile of the <i>p</i> -type ZnO thin films deposited on sapphire at 350°C (a) with N ₂ O and (b) without N ₂ O.....	85
Figure 4-4 X-ray diffraction profiles of ZnO thin films grown on sapphire at 350°C (a) with N ₂ O and (b) without N ₂ O.....	86
Figure 4-5 Transmittance spectra for the <i>p</i> -type ZnO thin films obtained (a) with N ₂ O and (b) without N ₂ O.	87
Figure 4-6 Plot of $(\alpha h\nu)^2$ versus photon energy for the ZnO thin films obtained (a) with N ₂ O and (b) without N ₂ O.....	87
Figure 4-7 Normalized room temperature PL spectra of obtained <i>p</i> -type ZnO thin films (a) with N ₂ O and (b) without N ₂ O.	88

Figure 4-8 Typical I-V characteristic of ZnO films in Hall measurement. Ohmic contact was established on both the connector 1 & 2 and connector 3 & 4 in four-point probe van der Pauw method.	92
Figure 4-9 Hole concentration versus temperature of <i>p</i> -type C-doped ZnO thin film.....	93
Figure 4-10 XRD spectra of as-grown and annealed ZnO thin films with different γ -scale. Peak position and FWHM of (0002) peak were indicated in the figure.	94
Figure 4-11 SIMS profile of as-grown and annealed ZnO thin films.....	95
Figure 4-12 XPS spectra of C 1s and O 1s of (a) O ₂ -annealed, (b) air-annealed, (c) N ₂ -annealed and (d) as-grown ZnO thin films.	96
Figure 4-13 Room temperature PL spectra of as-grown and annealed ZnO thin films.	97
Figure 4-14 PL spectra of as-grown and annealed ZnO thin films at 4.8 K.	98
Figure 5-1 Top view and 45° view of SEM image of ZnO structures grown for 5 minutes.....	102
Figure 5-2 SEM images of (a-b) an overview morphology on silicon wafer. (c-e) Typical ZnO spheres with shell composed of hexagonal disks and nanocrystals. (f-h) ZnO hexagonal stacking and lying disks. (i-k) Collapsed and broken ZnO spheres.	103
Figure 5-3 (a-b) TEM images of a broken cage and its SAED pattern (inset). (c-d) TEM images of a fine cage.....	105
Figure 5-4 (a-b) TEM image of a typical ZnO hexagonal disk. (c) SAED pattern of the hexagonal disk showing two sets of lattice. (d-e) Lattice reconstruction by performing IFFT operation on metallic Zn and ZnO diffraction pattern, respectively. The arrowheads show the clear distinction between the two reconstructions.....	106
Figure 5-5 Normalized XRD of ZnO structures grown with (a) 5; (b) 10; and (c) 12 minutes. The ZnO structures grown within 10 minutes show only ZnO related diffraction peaks.	107
Figure 5-6 Normalized PL of ZnO structures grown with 10 minutes and ZnO thin film.	108

Figure 5-7 A cartoon showing the growth mechanism for the ZnO hollow spheres and stacking disks structures. (a) Both the DEZn and O₂ reach the hot substrate. (b) The DEZn were dissociated in O-rich environment and resulting in the formation of a highly c-axis textured ZnO layer. (c) As the O₂ partial pressure became less due to the formation of ZnO, the DEZn vapor accumulates and dissociate via beta hydride elimination process. The DEZn will form hollow spheres or droplets as a result of surface energy minimization. (d) Subsequent oxidation on the DEZn hollow spheres and droplets form the ZnO hollow spheres and hexagonal stacking disks. The thin metallic Zn layer on the top of the disks might be due to the Zn wetting layer that not fully oxidized due to the near-zero O₂ partial pressure environment. 110

Figure 6-1 (a) Showerhead injection for MO and gas precursors. (b) Plasma ignition. (c) Rotational substrate holder with resistive coil heater that can heat up to 1000°C. 116

LIST OF TABLES

Table 1-1 ZnO-based heterojunction, and homojunction LEDs survey.	15
Table 2-1 Comparison table of various growth techniques for ZnO material.	21
Table 2-2 Estimated crystallite size of crystallographic plane (0002) of ZnO thin films at various growth temperatures.	28
Table 2-3 Estimated optical bandgap of ZnO thin films fabricated on quartz substrates at various growth temperatures.	34
Table 3-1 Estimated grain size of as-grown and annealed ZnO thin films from XRD, AFM, and SEM.	66
Table 3-2 Electrical properties of the as-grown and annealed ZnO thin films.	71
Table 4-1 Survey of <i>p</i> -type ZnO.	80
Table 4-2 Electrical property of ZnO thin films characterized by Hall effect measurement.	92

ABBREVIATIONS

AFM	Atomic Force Microscopy
CCD	Charge coupled device
CMOS	Complementary Metal Oxide Semiconductor
DMZn	Dimethylzinc
EL	Electroluminescence
EPM	Empirical pseudopotential method
eV	Electron volt
FWHM	Full width half maximum
HCP	Hexagonal close packed
LD	Laser diode
LED	Light-emitting diode
MBE	Molecular beam epitaxy
MOCVD	Metal organic chemical vapor deposition
PL	Photoluminescence
PLD	Pulsed laser deposition
PSD	Particle size distribution
RF	Radio frequency
rms	Root mean square
sccm	Standard cubic centimeter per minute
SEM	Scanning electron microscopy
SIMS	Secondary ion mass spectrometry
TMGa	Trimethylgallium
UV	Ultraviolet
XRD	X-ray diffraction

CHAPTER 1 INTRODUCTION

1.1 Motivation

1.1.1 Semiconductor revolution

The quantum revolution initiated at the beginning of the twentieth century, in conjunction with the invention of the vacuum tube, provided the inspiration for the invention of bipolar transistor in year 1947. The Nobel prize in Physics 1956 was awarded to John Bardeen, Walter Brattain, and William Shockley for their researches on semiconductors and invention of bipolar transistor (Figure 1-1).¹ The invention has initiated a new era in solid-state electronic and stirred up huge effort in semiconductor research. From then on, the semiconductor industry is dominated by silicon (Si) and germanium (Ge), which are considered as the first generation of the semiconductor materials. However, Si and Ge are not direct bandgap semiconductors, which have limited their application in opto-electronic and photonic devices.

Photons and phonons can be generated by the recombination of the excited electron-hole pairs in both direct and indirect bandgap semiconductors. However, the radiative recombination rate in indirect bandgap semiconductors is much lower than indirect bandgap semiconductors, such as Si and Ge.² For radiative recombination, the

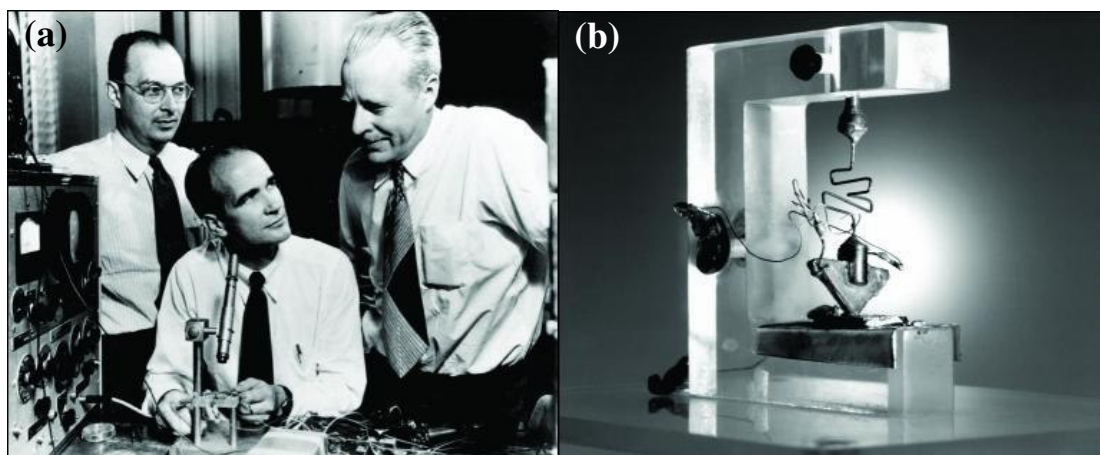


Figure 1-1 (a) From left to right, John Bardeen, William Shockley, and Walter Brattain at Bell Laboratories. (b) The first point contact germanium bipolar transistor.³

wavelength of the emitted photon can be calculated by the following equation:

$$\lambda = \frac{hc}{E_g} \quad (1.1)$$

where λ is the emitted wavelength, h is Planck's constant, c is the speed of light in vacuum, and E_g is the bandgap energy. Figure 1-2 shows the room-temperature bandgap energy versus lattice constant of common elemental and binary compound semiconductors.⁴

The demand on the current-driven light-emitting diodes (LEDs) and laser diodes (LDs) has motivated the development on semiconductors with direct bandgap. In the 1960s, the development of III-V compound semiconductors, such as gallium arsenic (GaAs), gallium phosphide (GaP), Indium phosphide (InP), and their alloys had brought a new revolution to the semiconductor industry. GaAs and related compounds have been used dominantly in the early 1990s for light emitters and high-speed electronics. The laser wavelengths of GaAs-based LDs range from infrared to the red region of the visible spectrum; while for GaP-based LEDs, the wavelengths range from green, orange and red region of the visible spectrum. Figure 1-3 shows the

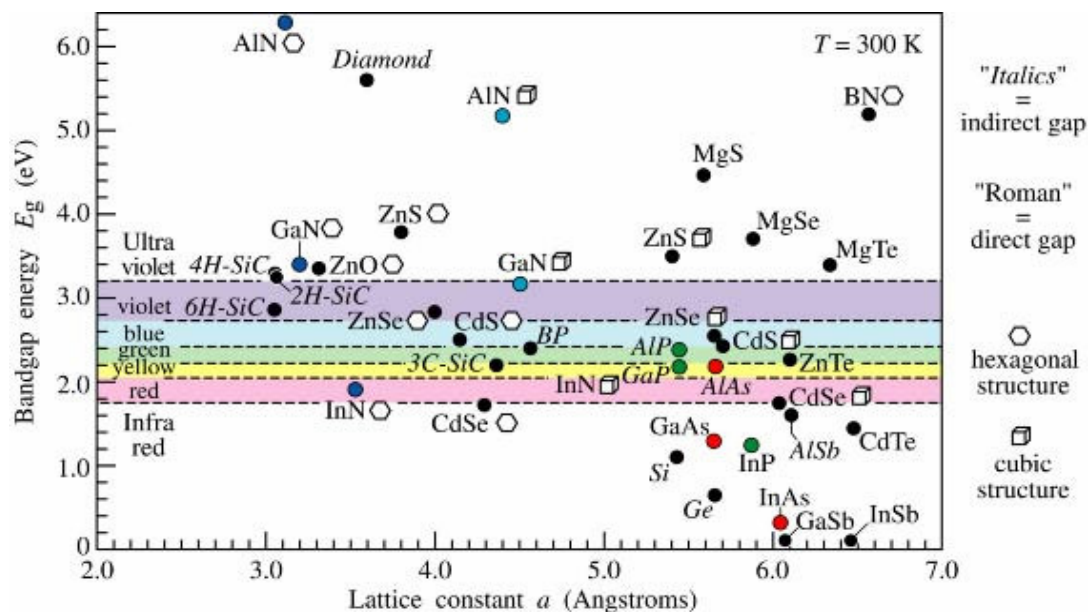


Figure 1-2 Room-temperature bandgap energy versus lattice constant of common elemental and binary compound semiconductors.⁴

CHAPTER 1 INTRODUCTION

luminescence efficiency versus emitted wavelength of visible LEDs made from phosphide, arsenide and nitride compound semiconductors.⁴ As is shown in Figure 1-3, phosphide and arsenide compound semiconductors could not emit blue or ultraviolet light. The quest for shorter wavelength (blue and ultraviolet) opto-electronic and photonic devices has been the focus of the compound semiconductor research in recent years.⁵

The wide bandgap semiconductors that have bandgap energy greater than 2.3 eV, such as diamond, silicon carbide (SiC), III-nitride (AlN, GaN), zinc selenide (ZnSe), and zinc oxide (ZnO) are regarded as the third generation semiconductors. Blue or even ultraviolet (UV) light can be emitted by the radiative recombination of the electron-hole pairs in the wide bandgap materials. The huge demand of the short-wavelength opto-electronic devices has stirred up the research on wide bandgap semiconductors.

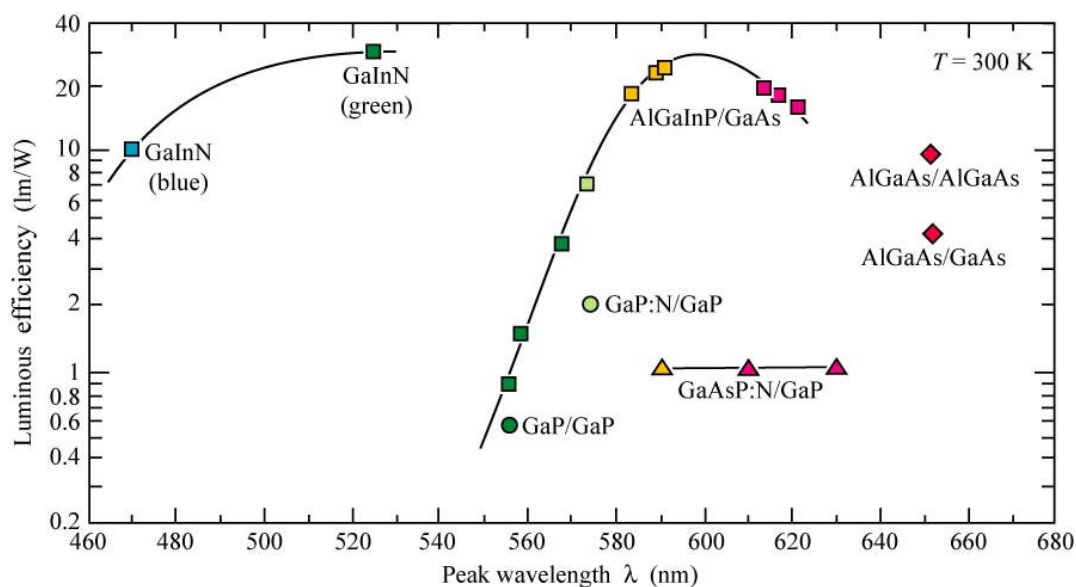


Figure 1-3 Luminescence efficiency versus emitted wavelength of visible LEDs made from phosphide, arsenide and nitride compound semiconductors.⁴

CHAPTER 1 INTRODUCTION

1.1.2 Potential market for wide bandgap semiconductors

The wide bandgap semiconductors have attracted much attention due to the strong demand of short-wavelength opto-electronic applications, such as blue and UV light-emitting diodes (LEDs) and laser diodes (LDs), high-density optical storage devices, full-color LED displays, electronic devices, and UV photodetectors, as shown in Figure 1-4.

Among the potential applications, blue and UV LEDs market is expected to grow from US\$ 1.5 billions in 2004 to US\$ 3 billions in 2010.⁶ Blue is one of the three primary colors (red, blue, and green) for display. The combination of primary color LEDs will generate white light, which can be used for solid state lighting. The LEDs are believed to be the lighting source in near future as LEDs have



Figure 1-4 Potential market for ZnO-based materials.⁷⁻¹⁵

CHAPTER 1 INTRODUCTION

advantages of longer lifetime and lower power consumption compared to the existing florescent light source. The emission efficiency of GaN-based white LED is as good as or better than that of the florescent lamps and it is expected to have great impact on display and solid-state lighting.¹⁶ Two good examples of the LED display are the world largest LED display NASDAQ market site and Stone Bridge, which is shown in Figure 1-5 and Figure 1-6, respectively.

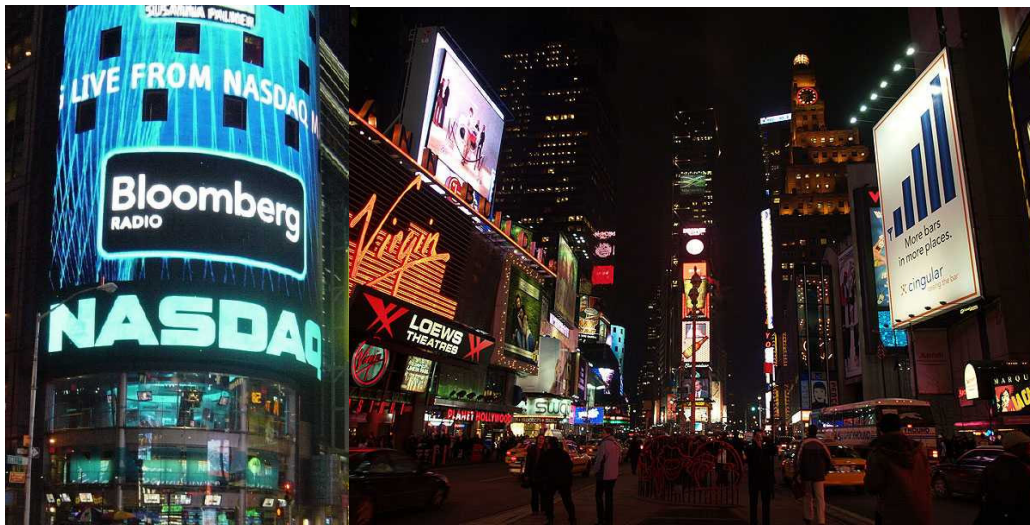


Figure 1-5 NASDAQ Market site at night. It consists of almost 19 millions high brightness LEDs.¹⁷



Figure 1-6 Stone Bridge at Regensburg, Germany with about 22,000 red and white LEDs.¹⁸

1.1.3 Why ZnO?

ZnO is a multifunctional material that has been investigated for many years and utilized in many applications, such as phosphor,^{19,20} varistor,^{21,22} solar cell,²³ transparent conductive thin film,^{24,25} gas sensor,^{26,27} thin film buffer,^{28,29} and thin film transistor.³⁰⁻³² Recently, ZnO has stimulated great interests because of its potential applications in blue and UV LEDs and LDs, owing to its wide direct bandgap of 3.37 eV at room temperature. As mentioned earlier, the strong demands on short-wavelength opto-electronic devices have attracted more and more attention on the research of wide bandgap semiconductors such as ZnSe, SiC, GaN, and ZnO. However, the asymmetry-doping problem of the wide bandgap semiconductors is still the main challenge presently. Among the wide bandgap semiconductors, remarkable progress has been achieved in III-nitride materials especially GaN-related materials in the past decade.³³ In 1989, Akasaki *et al.*³⁴ solved the *p*-type doping dilemma by Mg doping using a low-energy electron beam irradiation. In 1992, Nakamura *et al.*³⁵ further improved the *p*-type GaN films by using metal organic chemical vapor deposition. After that, they developed the commercial blue LEDs,³⁶ which are about 200 times as bright as previously available blue LEDs. In 1996, Nakamura *et al.* had successfully

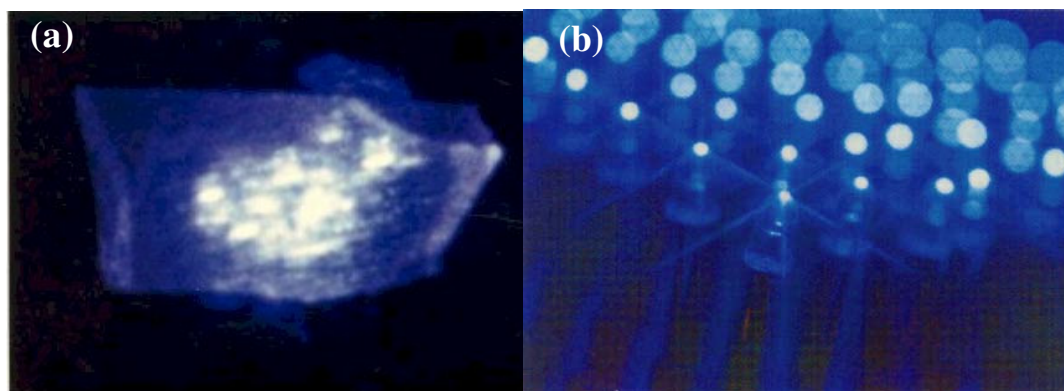


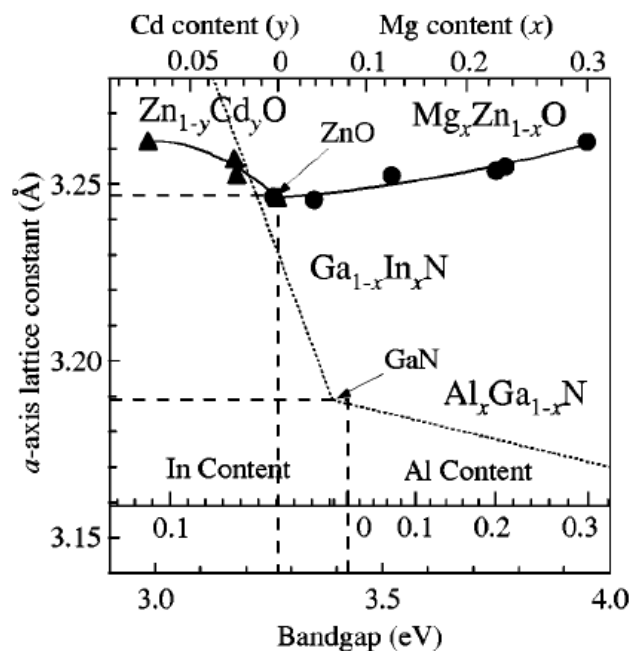
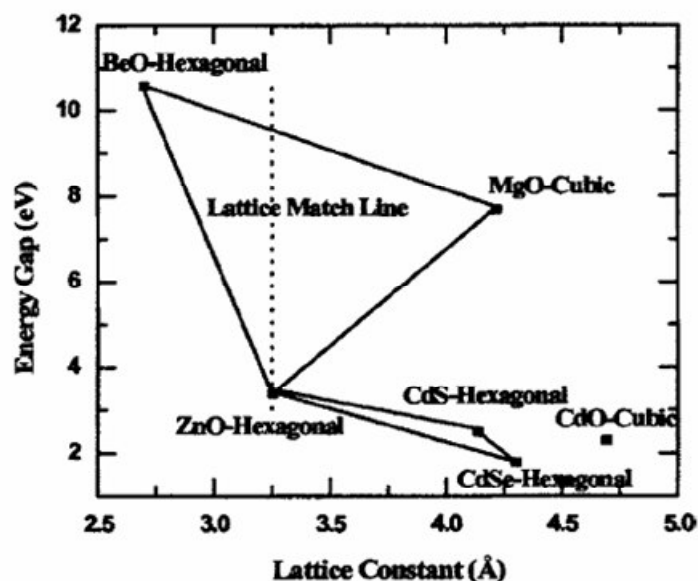
Figure 1-7 (a) World's first violet LED on GaN:Mg.³⁷ (b) Commercial GaInN/GaN blue LEDs array manufactured by Nakamura *et al.*, Nichia Corporation.⁴

fabricated the pulsed current-injection blue LDs^{38,39} and continuous wave (cw) operation LDs from InGaN-based material with over 10,000 hours of lifetime.⁴⁰ With the significant breakthrough on MOCVD growth of GaN-based materials, GaN-based optoelectronic devices are commercially available. Nevertheless, there are some major drawbacks of GaN-based materials compared with ZnO-based ones, making ZnO as another promising candidate for short-wavelength optoelectronic devices. A comparison of GaN and ZnO-based materials in various aspects such as emission efficiency, material and fabrication cost, Si-CMOS compatibility, and substrate availability, was made and elaborated in the following sections.

1.1.3.1 Emission efficiency

ZnO has a larger exciton binding energy (60 meV) compared with GaN (25 meV), and ZnSe (20 meV). The large exciton binding energy suggests that electron-hole pairs are well bounded even at room temperature ($kT = 26$ meV). Therefore, ZnO is expected to be a brighter emitter compared with other wide bandgap semiconductors. Besides, with a large exciton binding energy, ZnO-based blue and UV LEDs and LDs operating at room temperature can be expected, provided *p*-type ZnO is available.⁴¹⁻⁴³ In fact, room temperature lasing by optical excitation was demonstrated experimentally, which reveals the potential of ZnO as a blue or UV lasing material for the near future.⁴⁴⁻⁴⁸

The working device structure of a ZnO-based emitter would be in quantum well structure. The bandgap engineering in ZnO materials could be implemented by alloying magnesium (Mg) and cadmium (Cd), which increases and decreases the bandgap, respectively. Figure 1-8 shows the bandgap engineering of both ZnO and

Figure 1-8 Lattice constant of ZnO, GaN and their related alloys.⁴⁹Figure 1-9 Energy bandgaps, lattice constants and crystal structures of selected II-VI compounds.⁵⁰

GaN and their related alloys.⁴⁹ It can be seen that the a-axis lattice mismatch for ZnO ternary alloy films is much smaller than that of GaN ternary alloy films. More recently, Ryu *et al.*⁵⁰ proposed a new BeZnO ternary compound, which is expected to match ZnO lattice better as shown in Figure 1-9. Compared to GaN ternary alloy, the small lattice-mismatch of ZnO ternary alloy films will reduce the lattice-mismatch

induced strain and hence the piezoelectric field between the quantum well layers. This will in turn improve the emission efficiency and hence device performance of ZnO-based light-emitting devices.

1.1.3.2 Material and fabrication cost

GaN-based materials depend strongly on indium (In) alloying. It is known that both Ga and In are rare compared to Zn mineral. As reported in Compound Semiconductor magazine, the price of indium has risen ten-fold over the past two years (Figure 1-10).⁵¹ Moreover, high-purity of ammonia gas used in GaN fabrication is also relatively expensive than the oxidizer used for ZnO fabrication. As a result, the material cost for GaN-based materials is much more expensive than ZnO-based materials. Other than the raw material cost, the fabrication cost for GaN-based materials is also more expensive than that of ZnO-based materials. The deposition temperature required to grow GaN-based materials is about 1050°C, which is higher compared with ZnO-based materials of 500-800°C. The tight demanding on high deposition temperature of growing GaN-based materials makes the fabrication process costly and hence more expensive devices. As a result, ZnO-based LEDs and LDs are expected to be cheaper than GaN-based LEDs and LDs.



Figure 1-10 Price of Indium. (Extracted from Compound Semiconductor magazine)⁵¹

1.1.3.3 Si-CMOS compatibility

Low deposition temperature of ZnO materials (500-800°C) and possible wet-chemical processing enable the possibility of integrating the ZnO thin films on Si. This is particularly interesting since if the ZnO can be integrated on Si wafer, the available low-cost CMOS technology would further reduce the fabrication cost of the optoelectronic devices. Subsequently, it would be easier for LEDs to enter the lighting market and compete with florescent lamps. Also, there would be great impact on the display industry, data storage, telecommunication, consumer electronics, etc.

1.1.3.4 Substrate availability / chemical & radiation resistance

As GaN wafer is still not commercially available, GaN and related materials can only be epitaxially grown on certain substrates such as sapphire, ZnO or SiC by adopting buffer layer technology, while ZnO of reasonable quality can be grown on a wide variety of substrates such as ZnO, sapphire, Si, quartz, and even glass. The flexibility of substrate used in growing ZnO thin films has certainly broadened its possible applications. For example, the availability of large-area ZnO epi-ready substrates provides the best substrates for the growth of ZnO-based emitting devices. The deposition of ZnO on glass or indium tin oxide (ITO) opens up a window of transparent thin film transistor for display technology.

Furthermore, the chemical & radiation resistance for ZnO materials is better than GaN materials, which makes ZnO a possible candidate for space-based applications.

In summary, from intrinsic material properties to fabrication process, ZnO has advantages over GaN. As a result, ZnO has attracted much attention in the past

decade.⁵²⁻⁵⁵ In particular, significant effort has been devoted to the realization of *p*-type ZnO, which is the major bottleneck to be tackled in order to realize ZnO-based optoelectronic devices. Driven by this motivation, a MOCVD system was built-up for the growth of ZnO-based materials in this work.

1.1.4 Overview of ZnO

ZnO is one of the natural chemical forms of zinc. It is a II-VI compound semiconductor with a wide direct bandgap of 3.337 eV at room temperature and 3.44 eV at 4 K.^{56,57} ZnO has a wurtzite, hexagonal close packed (HCP) structure with lattice constants of $a=3.25 \text{ \AA}$ and $c=5.21 \text{ \AA}$, as shown in Figure 1-11. Two types of atoms, Zn and O, are tetrahedrally coordinated to each other and are therefore equivalent in position. The Zn-O distance is 1.992 \AA parallel to the *c*-axis and 1.973 \AA in the other three directions of the tetrahedral arrangement of nearest neighbors.

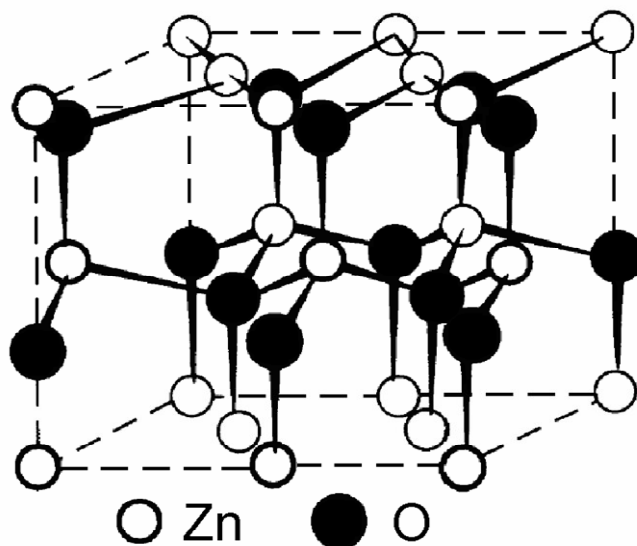


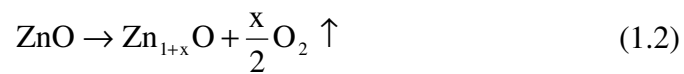
Figure 1-11 Wurtzite, hexagonal close packed (HCP) structure of ZnO.

1.1.4.1 Bipolar doping of ZnO

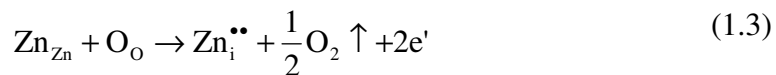
The most important property of semiconductors is the ability to change their conductivity through the addition of impurity atoms. The controlled addition of

impurities to alter the properties of a semiconductor is called “doping”. ZnO, like other wide bandgap semiconductors, has problem in bipolar doping, more specifically, it can be easily doped *n*-type but not *p*-type.⁵⁸⁻⁶¹ Also, it is well known that *p*-type doping in oxides and nitrides are very difficult, while efficient *n*-type doping is very difficult to achieve in ZnTe,^{62,63} and diamond.⁶⁴

The ZnO structure is relatively open, with all of the octahedral and half of the tetrahedral sites empty. It is, therefore, relatively easy to incorporate external dopants into the ZnO lattice. The open structure also influences the nature of defects and the mechanism of diffusion. Single crystal ZnO exhibits *n*-type conductivity. The reason for getting intrinsic *n*-type conduction in ZnO is the excess zinc that acts as a donor. The zinc excess results in a non-stoichiometric compound Zn_{1+x}O , which can be explained in the following chemical reaction:



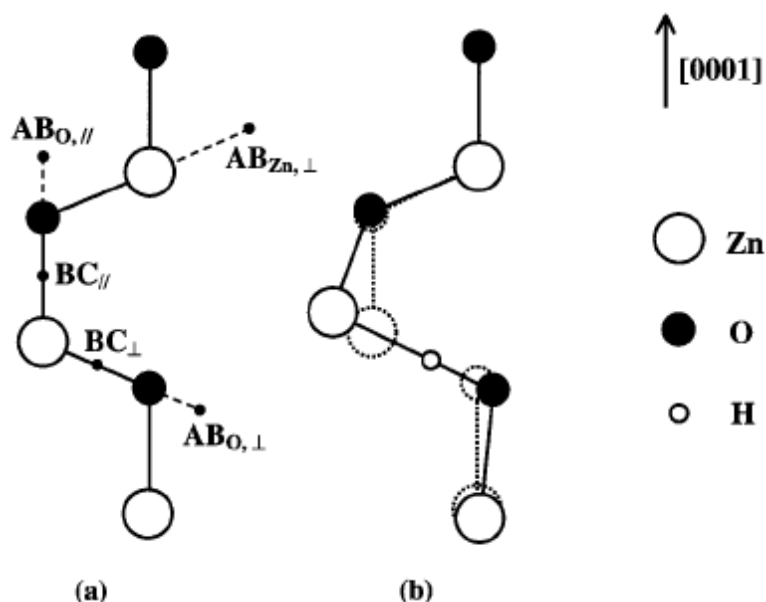
Using Kröger-Vink notation for lattice defects, the zinc interstitial (Zn_i) in ZnO can be directly ionized and give away electrons as Eq. (1.3) or subsequently be ionized and give away electron as Eq. (1.4) and Eq. (1.5). As a result, electrons of Zn_i and Zn_i^\bullet can be ionized and transferred to other part of crystal, which causes the intrinsic *n*-type conduction in ZnO.



1.1.4.2 Hydrogen in ZnO

Other than the intrinsic point defects, the conduction of the ZnO thin films is also governed by the impurities that incorporate into the films during deposition. Van de Walle has done a first principle calculation on the hydrogen (H) impurities in ZnO thin films and concluded that the H is also responsible for the *n*-type conduction in ZnO thin films, as shown in Figure 1-12.⁶⁵

Fortunately, the H impurities could be driven out from the ZnO thin films by high-temperature post-growth annealing ($>600^{\circ}\text{C}$).⁶⁶ However, the passivation of the *p*-type dopants caused by the H impurities might be a serious issue to look into.⁶⁷



1.1.5 Current status of ZnO research

After decades of research, there is no doubt that ZnO is close to a commercialization stage, where commercial ZnO-based devices are burgeoning. Table 1-1 has tabulated the ZnO-based heterojunction and homojunction LEDs demonstration from the research groups around the world.

Among them, Tsukazaki *et al.*⁷⁷ firstly demonstrated the ZnO-based homojunction LED by laser molecular beam epitaxy (laser MBE) in year of 2005. The *p*-type ZnO:N layers were fabricated using a repeated temperature modulation epitaxy and the electroluminescence (EL) spectrum consists of emission bands centered at 570 nm and 400 nm at room temperature. After that, homojunction LEDs were demonstrated in succession by several groups using different techniques and *p*-type dopants. Liu *et al.*,⁸⁶ Pan *et al.*,⁸⁷ and Xu *et al.*⁸⁸ realized the *p*-type ZnO:N layer and hence ZnO homojunction LED by metal organic chemical vapor deposition (MOCVD). The EL of their LEDs appears dominantly at 520 nm, 384 nm, and 450 nm, respectively. More recently, Ryu *et al.*⁸⁹ has even demonstrated the ZnO-based quantum-well structure LED, with a wall-plug efficiency of 0.1%. They tackled the *p*-type ZnO problem by hybrid beam deposition and employed arsenic (As) as *p*-type dopant.

From the ZnO homojunction LEDs demonstrations, it is obvious that the ZnO light-emitting devices could be realized by using either N, As, or P as *p*-type dopants. Moreover, all these devices were fabricated using either MBE or MOCVD, which clearly indicates the feasibility of these two deposition techniques. Comparing to MBE, MOCVD is a better tool for ZnO-based devices, as MOCVD enjoys lower cost, easy scaling up, and the successful story in producing GaN-based LEDs and LDs. It is

CHAPTER 1 INTRODUCTION

worth mentioning that to be commercial successful, ZnO LEDs have to be produced in a cheaper process compared to GaN LEDs, which can only be fulfilled by MOCVD.

Table 1-1 ZnO-based heterojunction, and homojunction LEDs survey.

Researchers (Year published)	Techniques	Structures	Dopants for <i>p</i> -type	Electroluminescence, EL (emission peak)
Aoki <i>et al.</i> (2000) ⁶⁸	Laser doping	<i>p</i> -ZnO/ <i>n</i> -ZnO	P	400 – 500 nm at 110 K
Hosono <i>et al.</i> (2002) ⁶⁹	PLD	<i>p</i> -SrCu ₂ O ₂ / <i>n</i> -ZnO	NIL	382 nm at RT
Yu <i>et al.</i> (2003) ⁷⁰	Laser ablation	<i>n</i> -ZnO/ <i>p</i> -GaN	NIL	384 nm at RT
Alivov <i>et al.</i> (2003) ⁷¹	CVD	<i>n</i> -ZnO/ <i>p</i> -GaN	NIL	430 nm at RT
Alivov <i>et al.</i> (2003) ⁷²	CVD	<i>n</i> -ZnO/ <i>p</i> -AlGaIn	NIL	389 nm at RT
Wang <i>et al.</i> (2003) ⁷³	RF magnetron sputtering	<i>n</i> -ZnO/ <i>p</i> -diamond	NIL	NIL
Ip <i>et al.</i> (2004) ⁷⁴	PLD	<i>p</i> -Zn _{0.9} Mg _{0.1} O/ <i>n</i> -ZnO	P	NIL
Osinsky <i>et al.</i> (2004) ⁷⁵	RF Plasma- assisted MBE	<i>n</i> -Mg _{0.1} Zn _{0.9} O/ <i>n</i> -ZnO/ <i>p</i> -Al _{0.16} Ga _{0.84} N/ <i>p</i> -GaIn	NIL	390 nm at RT
Chichibu <i>et al.</i> (2004) ⁷⁶	Helicon-wave- excited-plasma sputtering	<i>n</i> -ZnO/ <i>p</i> -CuGaS ₂	NIL	548 nm at RT
Tsukazaki <i>et al.</i> (2005) ^{77,78}	Laser MBE	ZnO <i>p-i-n</i>	N	400 nm at RT
Hazra <i>et al.</i> (2005) ⁷⁹	CVD	ZnO <i>p-n</i>	NIL	NIL
Xu <i>et al.</i> (2005) ⁸⁰	RF reactive sputtering	<i>p</i> -GaIn/ <i>i</i> -ZnO/ <i>n</i> -ZnO	NIL	386 nm at RT
Hwang <i>et al.</i> (2005) ⁸¹	RF magnetron sputtering	<i>p</i> -ZnO/ <i>n</i> -GaIn	P	409 nm at RT
Jang <i>et al.</i> (2005) ⁸²	Diffusion	ZnO <i>p-n</i>	P	NIL
Lee <i>et al.</i> (2005) ⁸³	Laser annealing	ZnO <i>p-n</i>	P	NIL
Yuen <i>et al.</i> (2005) ⁸⁴	Filtered cathodic vacuum arc technique	<i>n</i> -ZnO/ <i>p</i> -SiC(4H)	NIL	385 nm at RT
Jiao <i>et al.</i> (2006) ⁸⁵	Plasma-assisted MBE	ZnO <i>p-n</i>	N	410 nm at 11 K
Liu <i>et al.</i> (2006) ⁸⁶	MOCVD	ZnO <i>p-n</i>	N	372 nm and 520 nm at RT
Pan <i>et al.</i> (2006) ⁸⁷	MOCVD	ZnO <i>p-n</i>	N	384 nm at RT
Xu <i>et al.</i> (2006) ⁸⁸	MOCVD	ZnO <i>p-n</i>	N	430 – 600 nm at RT
Ryu <i>et al.</i> (2006) ⁸⁹	Hybrid beam deposition	Be _{0.2} Zn _{0.8} O-ZnO MQW	As	363 nm, 388 nm and 550 nm at RT

1.2 Objectives

This dissertation addresses the growth and characterization of ZnO thin films and nanostructures by MOCVD. The structural, optical, and electrical properties of ZnO thin films were studied in detail with the variation of growth parameters. Among the growth parameters, growth temperature, precursors flow rate, and gas flow configuration are crucial for obtaining good quality ZnO thin films.

One of the main objectives of this work is to set up a MOCVD system to accommodate the needs for growing ZnO thin films. As the Dimethylzinc (DMZn) reacts with oxygen (O_2) even at room temperature, the pre-reaction of the gaseous phase of precursors must be avoided. Therefore, conventional MOCVD reactor designs are not suitable for growing ZnO thin films. Besides the reactor design, other growth parameters such as temperature and flow rate will be evaluated in order to establish an optimum growth condition. The optical properties of the ZnO thin films, such as transmission spectra and photoluminescence (PL) will be studied and correlated with the structural properties. The growth conditions for obtaining polycrystalline, nanocrystal embedded, and highly *c*-axis oriented ZnO thin films have been investigated. ZnO nanostructures were also investigated in detail and the difference in growth condition of ZnO thin films and nanostructures was discussed.

The major technical difficulty in development of ZnO material is the fabrication of efficient and reliable *p*-type ZnO thin films. In this work, we will also look into the fundamental issues of the *p*-type doping of ZnO materials. The intrinsic defects induced by the non-stoichiometric growth are responsible for getting *n*-type conduction in ZnO thin films. The undoped ZnO thin films grown at various conditions were carefully examined in order to identify the origin of the problem.

1.3 Major contributions

This dissertation presents the investigation on the growth and characterization of ZnO thin films grown by MOCVD. A home-made MOCVD has been specifically built for ZnO growth and the reactor design has been investigated in the course of the work. The properties of the ZnO thin films grown by different reactor design were characterized in terms of structural, optical, and electrical properties. In the mean time, *p*-type doping issue on ZnO materials was also investigated.

Major contributions are summarized as followings:

- A home-made MOCVD has been specifically catered for ZnO growth and investigation. Various reactor designs have been implemented and their corresponding effects to the growth of ZnO thin films have been addressed and discussed. By accumulating the knowledge and experience during the modification, a second generation of MOCVD system was designed and it is being manufactured. The second generation MOCVD is expected to overcome most of the problems encountered in the first generation MOCVD.
- Post-growth annealing treatment on as-grown ZnO thin films has been investigated. Different type of the mass transport mechanisms are discussed and correlated with the experimental results. Ostwald ripening, together with sintering process were evidently observed and resulting in a transformation from ZnO thin films to nanoneedles. By using the coarsening kinetics developed by Lifshitz and Slyozov, and later Wagner, the activation energy of the Ostwald ripening in ZnO thin films was estimated for the first attempt.
- *P*-type doping in ZnO has been investigated during the course of the work. Nominal undoped and N-doped *p*-type ZnO thin films have been realized. The carbon, which is inevitable in MOCVD grown ZnO thin films, is proposed to

be the element that immobilize the oxygen interstitial, resulting in *p*-type conduction in ZnO thin films. The acceptor level of the oxygen interstitial was identified and reported.

- ZnO self-assembled hollow spheres and stacking disks have been fabricated without catalyst. The hollow spheres and stacking disks were fabricated at low growth temperature of 350°C. At such a low temperature, the evaporation mechanism that causes the formation of hollow spheres is unlikely to happen. In this dissertation, a possible growth mechanism of the ZnO hollow spheres and stacking disks was proposed and discussed.

1.4 Organization

The dissertation starts with chapter 1, which describes the motivation and the objectives of the research. Background of the semiconductors revolution has been briefed and the demand of wide bandgap semiconductors is illustrated. Also, the comparison of GaN and ZnO concluded that ZnO is a promising wide direct bandgap semiconductor for UV/blue emitting devices. In this chapter, we have also revealed the current research status of the ZnO materials.

Chapter 2 provides the background on various deposition techniques for ZnO growth. A home-made MOCVD system was specifically built for this work due to the advantages of MOCVD compared with other deposition techniques for ZnO growth. The growth and characterization of ZnO quantum dots embedded films and highly *c*-axis oriented ZnO thin films are presented.

In chapter 3, some reactor designs are depicted together with the characterization results of the ZnO thin films deposited. Growth, characterization, and post-growth thermal annealing treatment on the highly *c*-axis oriented ZnO thin films

CHAPTER 1 INTRODUCTION

are presented and discussed. The second generation of the MOCVD system is also introduced in this chapter.

The *p*-type doping issue of ZnO thin films is addressed in chapter 4. The realization of nominal undoped *p*-type ZnO thin films is investigated. Conversion of nominal undoped *n*-type ZnO thin films to *p*-type ZnO thin films by post-growth annealing is also presented in this chapter. The possible acceptor complex is proposed and discussed.

Chapter 5 shows some ZnO nanostructures grown by the MOCVD. The difference of the growth behavior of ZnO thin films and nanostructures is described and discussed. A possible growth mechanism for obtaining ZnO nanostructures is proposed.

























The dissertation ends in chapter 6 with a summary of the main results and recommendations for future work.

CHAPTER 2 ZNO QUANTUM DOTS EMBEDDED THIN FILMS BY MOCVD

2.1 Background

In the past decade, ZnO thin films have been prepared by various techniques such as metal organic chemical vapor deposition (MOCVD),⁹⁰⁻⁹³ molecular beam epitaxy (MBE),⁹⁴⁻⁹⁷ pulsed laser deposition (PLD),^{28,74} liquid phase epitaxy (LPE),^{98,99} filtered cathodic vacuum arc (FCVA),^{84, 100-104} sputtering,^{12,31, 105, 106} and ultrasonic spray pyrolysis.¹⁰⁷ The choice on the deposition techniques always depends on the quality of the film deposited, the feasibility in fabricating complex devices, such as multiple quantum well structures, the equipment cost which including maintenance and fabrication, and last but not least, the throughput of the equipment for productivity consideration. A comparison of various growth techniques in a few major aspects for ZnO was tabulated and shown in Table 2-1. Among the various aspects, film quality and feasibility in fabricating complex devices determine the effectiveness of the equipment, while the cost and throughput determine the potential ability of commercialization. Comparing the growth techniques, MOCVD has a clear advantage of being an advanced research tool for material and device physics, while reserving the potential of being a production tool for devices commercialization. Since the birth of MOCVD growth concept in mid-1980s, MOCVD has gone from primarily a research tool to the stage where it is now being practically used in microelectronic and optoelectronic industry, especially for GaN and related materials.^{35,36} The ease of scale-up in MOCVD system from laboratory to industrial tool has stimulated tremendous interest and research activity on MOCVD growth of ZnO material. In the opinion of the authors, MOCVD is a promising technique to be employed in ZnO

Table 2-1 Comparison table of various growth techniques for ZnO material.

Growth technique	Film quality	Feasibility in fabricating complex devices	Cost	Throughput	Target applications
MBE	 Excellent	 Excellent	 High	 Low	Emitting devices; transistors; spintronics
MOCVD	 Good	 Good	 Moderate	 High	Emitting devices; transistors; spintronics
LPE	 Excellent	 Moderate	 Low	 High	Emitting devices; transistors; spintronics
PLD	 Good	 Moderate	 Moderate	 Low	Emitting devices; transistors; spintronics
FCVA	 Good	 Good	 Moderate	 High	Emitting devices; transistors; spintronics
Sputtering	 Poor	 Poor	 Low	 High	Transparent conductors and thin film transistors

material research as it is a well-developed method to grow GaN films, which is isomorphic to ZnO.¹¹⁶

However, as mentioned in the previous section, commercial nitride-based MOCVD system could not be directly used to grow ZnO thin films. Therefore, research on MOCVD growth of ZnO thin films could not take full advantages of the mature nitride-based MOCVD technology. Nevertheless, the fruitful experiences of nitride-based MOCVD technology from past few decades will definitely accelerate the development of ZnO-based MOCVD. The two competing giants of the nitride-based MOCVD suppliers, Aixtron (Germany) and Emcore, which is now owned by Veeco (USA), have taken an active interest in oxide-based MOCVD development, especially for ZnO-related materials. Beside the two MOCVD giants, other research groups from universities or institutes have also shown interests in the realization of ZnO-based devices by MOCVD. Triboulet *et al.*¹⁰⁸ has tabulated and plotted the

number of papers reporting on the MOCVD growth of ZnO as a function of time, as shown in Figure 2-1. As Figure 2-1 was tabulated up to year 2003 only, we extended the data to year 2006. According to quick search in the ISI web of knowledge, the number of publications in year 2004, 2005 and 2006 on MOCVD growth of ZnO was 50, 70 and 52, respectively.¹⁰⁹ The sharp increase in papers published after year 2000 clearly indicates that MOCVD is being looked upon as a promising tool to fabricate ZnO thin films and ZnO-based devices. As a result, MOCVD is expected to make significant impact in ZnO growth just as before.

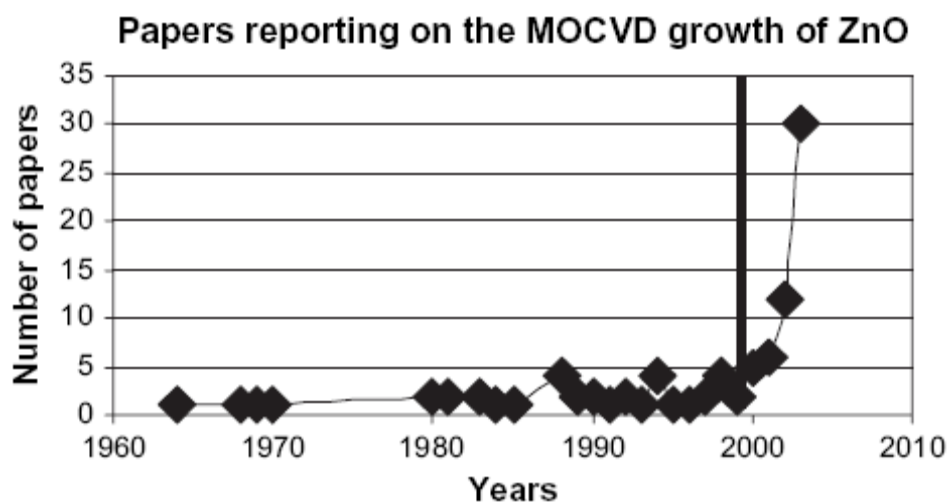


Figure 2-1 Number of papers on MOCVD grown ZnO as a function of time.¹⁰⁸

2.2 MOCVD System

In this work, we have specifically built a simple yet comprehensive MOCVD system for ZnO growth. The schematic of the MOCVD system is depicted in Figure 2-2, while the photos of the system are shown in Figure 2-3. In our MOCVD system, there are two metal organic lines for base and dopant. N₂ is used as carrier gas to transport the metal organic vapor into MOCVD reactor together with a separate gas oxidizer. Based on this setup, systematic study of MOCVD reactor design, associated with growth parameters, is conducted. The experiments revealed that the reactor design plays an important role in getting various types of ZnO thin films. With the first generation of reactor, thorough investigation has been carried out by varying all the growth parameters, such as growth temperature, growth pressure and precursors flow rate. From the material characterization results, it was found that ZnO quantum dots (QD) embedded films were repeatably fabricated. By modifying the reactor design, highly-oriented ZnO polycrystalline films were obtained. In the following chapters, key experiments and characterization results will be presented and discussed.

CHAPTER 2 ZNO QUANTUM DOTS EMBEDDED THIN FILMS BY MOCVD

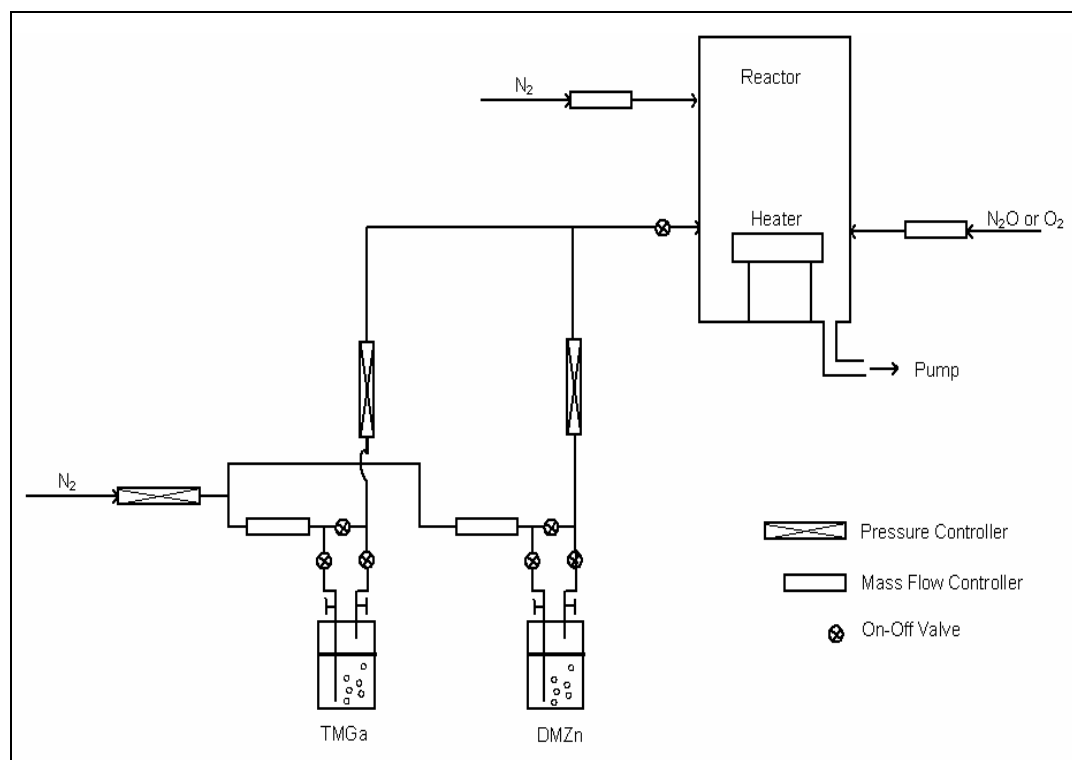


Figure 2-2 MOCVD system, consists of two metal organic sources (DMZn and TMGa), a gas oxidizer injection and a background gas line.

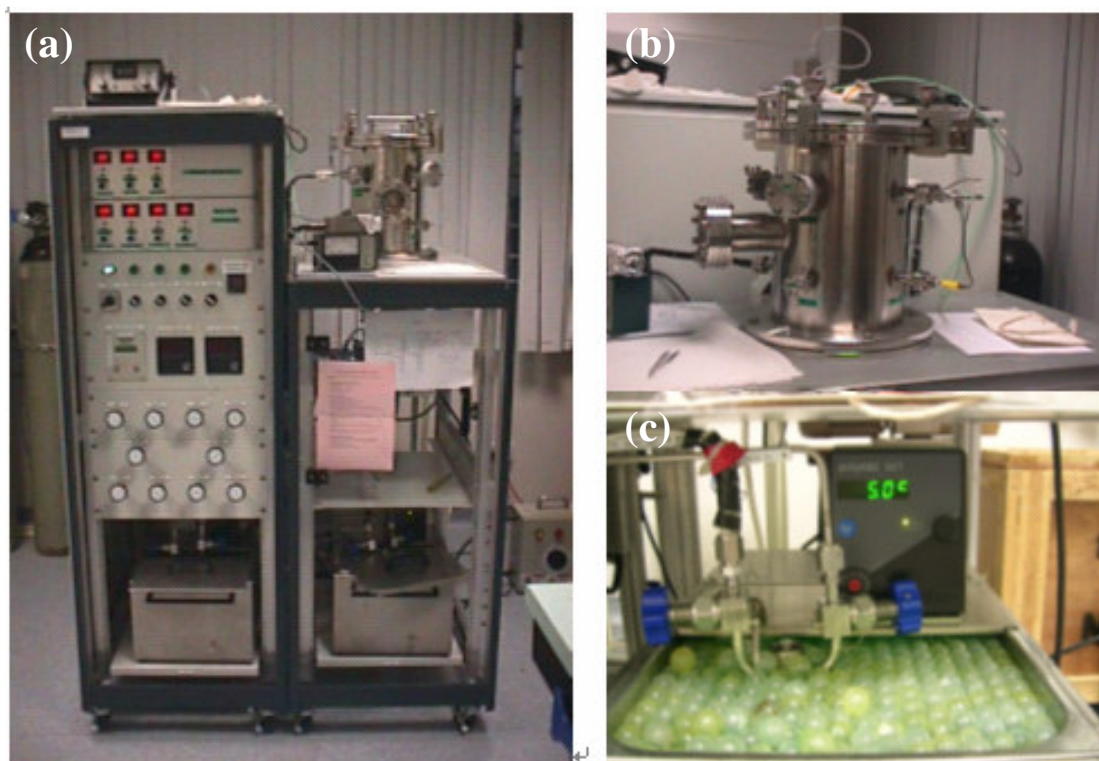


Figure 2-3 (a) Home-made MOCVD system, (b) Vertical reactor chamber and (c) MO bubbler in a coolant bath.

2.3 ZnO Quantum Dots Embedded Films

2.3.1 MOCVD Reactor Setup

The initial design of the MOCVD reactor was depicted in Figure 2-4. The DMZn, carried by N_2 gas, was deliberately designed to flow parallel with the O_2 nozzle towards the substrates. By using this setup, systematic study was carried out to grow ZnO thin films on various substrates such as Al_2O_3 (0001), quartz, and Si (100) by varying the growth parameters such as growth temperature, precursors flow rate, growth pressure. Post-growth annealing on the deposited films was also carried out to investigate the effect of annealing.

With the initial reactor design as shown in Figure 2-4, no epitaxial growth was demonstrated with even Al_2O_3 (0001) substrates. In fact, ZnO thin films grown on Al_2O_3 (0001) have similar structural, optical and electrical properties as ZnO thin films grown on quartz and Si (100). The experiments show that the growth is independent of the substrate used, indicating the inappropriate design of reactor. Nevertheless, these experiment data provide invaluable insights on the ZnO growth behavior which benefits the design of second generation MOCVD. In this section, some typical results of the ZnO films grown by the configuration in Figure 2-4 were discussed.

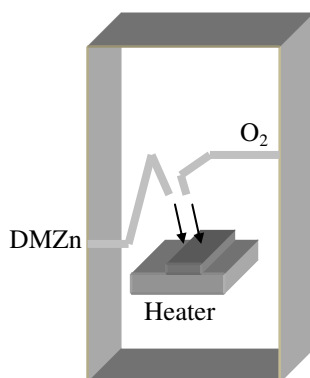


Figure 2-4 Initial MOCVD reactor design. DMZn (carry by N_2) and O_2 gases were deliberately designed to flow parallel towards the substrates.

2.3.2 Experiment

The ZnO thin films used in this study were grown on Al₂O₃ (0001), quartz, and Si (100) by the first generation of MOCVD system. The growth temperature was varied from 200 to 500°C with an increment of 50°C. DMZn, N₂ gas, and high-purity O₂ were used as zinc source, carrier gas, and oxidizing agent, respectively. The flows of DMZn and O₂ were set at 30 and 20 sccm, respectively. The DMZn bubbler was kept at -10°C in a coolant bath. The chamber pressure was maintained at about 30 mbar and the deposition time for all the samples was 10 min. Post-growth thermal annealing, if any, was carried out in a mixed O₂ and N₂ ambient at 500°C for 10 min.

The crystalline structure of the films was characterized by X-ray diffraction (XRD) measurement with CuK α radiation (Siemens D5005 X-Ray Diffractometer). The surface morphology of the ZnO thin films was investigated by a Digital Instruments NanoScope IIIa atomic force microscopy (AFM). The optical transmission spectra were measured with a UV-2501PC spectrophotometer at room temperature. The photoluminescence (PL) spectra were measured with a micro-PL excited by the 325 nm line of a 30 mW He-Cd laser and detected with a charge coupled device (CCD) array at room temperature.

2.3.3 Results and Discussion

Typical XRD data of the ZnO thin films grown on quartz substrates at various growth temperatures from 200 to 500°C with an increment of 50°C was shown in Figure 2-5 (a) and (b). It was found that all as-grown ZnO thin films exhibit polycrystalline structure, with the XRD peaks similar to that of ZnO powders.¹¹⁰ Using the background noise level as a reference, it can be seen that the

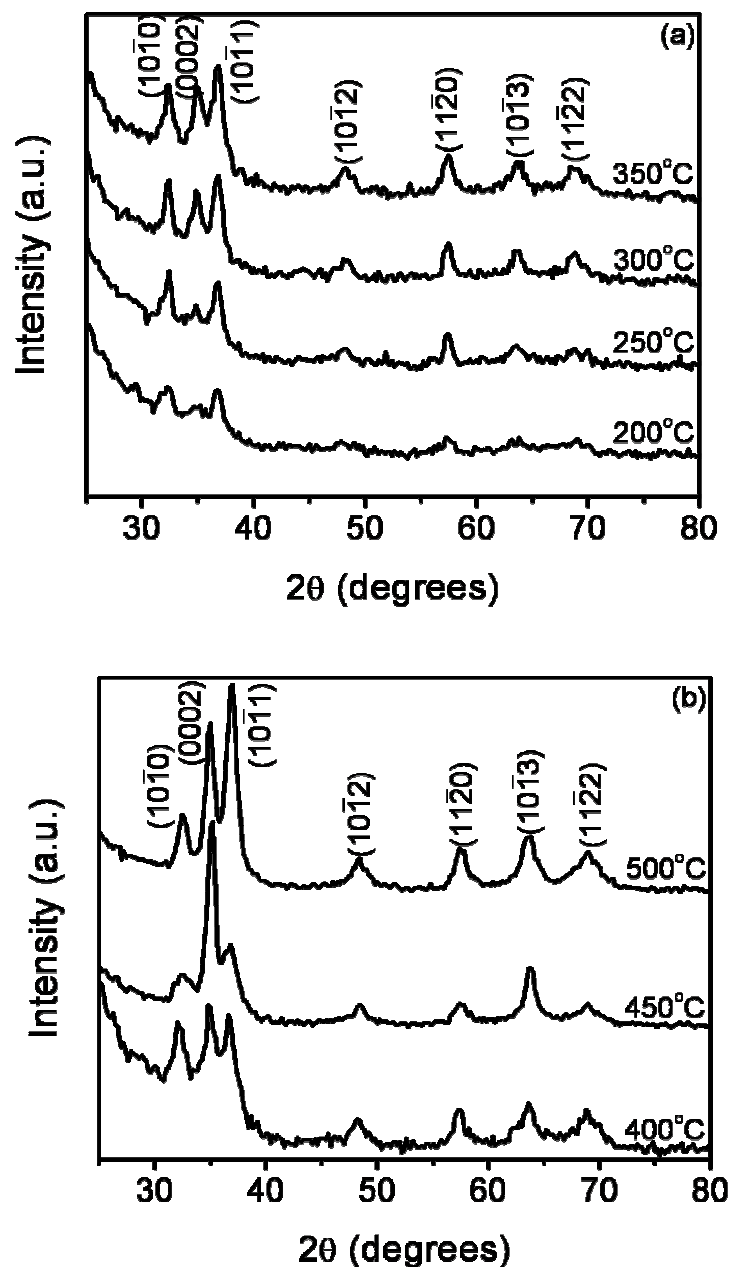


Figure 2-5 XRD profiles of ZnO thin films fabricated on quartz substrates at various temperatures from (a) 200 to 350°C, (b) 400 to 500°C with an increment of 50°C.

crystallinity of all the films grown at low temperature from 200°C to 400°C are poor, as shown in Figure 2-5 (a) and (b). The XRD measurements show that the ZnO thin films obtained contain nano-sized crystallites, vary from 5 nm to 13 nm according to Scherrer's formula:

Table 2-2 Estimated crystallite size of crystallographic plane (0002) of ZnO thin films at various growth temperatures.

Growth Temperature	Crystallite size (nm) in crystallographic plane (0002)
200°C	5.57
250°C	7.66
300°C	9.93
350°C	8.85
400°C	8.75
450°C	14.69
500°C	10.11
350°C+annealing at 500°C	13.55

$$t = \frac{C\lambda}{B \cos \theta} \quad (2.1)$$

where B is the full width at half maximum (FWHM in radians) of XRD yields, λ is the x-ray wavelength ($CuK_{\alpha} = 0.154 \text{ nm}$), θ is the Bragg diffraction angle and C is a correction factor which is taken as 1. The estimated crystallite size at crystallographic plane (0002) was summarized in Table 2-2. From Table 2-2, it can be seen that the estimated crystallite size ranges from 5 nm to 13 nm for crystallographic plane (0002). It should be mentioned that the crystallite size should not be uniform and the estimated value may not be exact, which can be seen from Table 2-2 that the crystallite size does not increase monotonically with temperature.

The poor crystal quality of the films grown at low temperature can be greatly improved by annealing. Figure 2-6 compares the XRD data of the 350°C as-grown sample and its subsequently annealed sample at 500°C in O_2 and N_2 ambient for 10 minutes. It can be seen that the c-axis orientation is improved significantly after the annealing process, with FWHM of (0002) reduces from 1.04 degrees to 0.68 degrees.

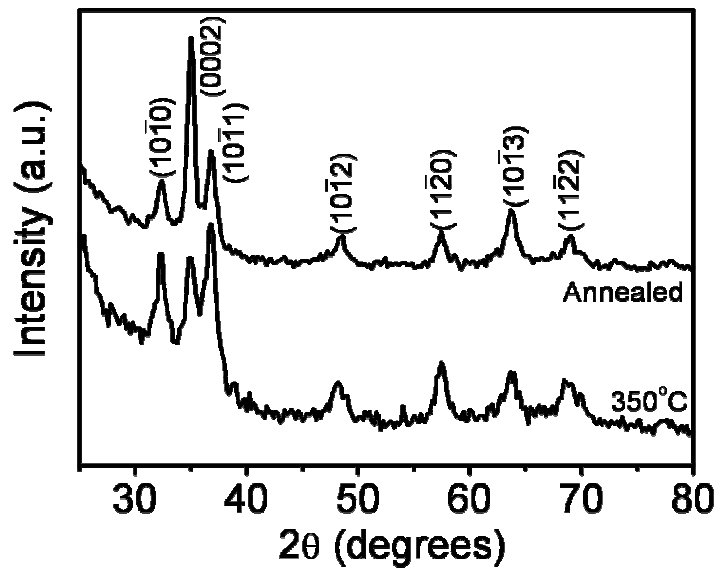


Figure 2-6 XRD profiles of ZnO thin films fabricated on quartz substrates at 350°C and subsequently annealed at 500°C for 10 minutes.

In order to distinguish the effect of crystallite-size induced broadening and strain induced broadening at FWHM of the XRD profile, the Williamson-Hall plot (Ref. 111) was performed and shown in Figure 2-7. The crystalline size and strain can be obtained from the intercept at the y-axis and the slope, respectively:

$$B \cos \theta = \frac{C\lambda}{t} + 2\varepsilon \sin \theta \quad (2.2)$$

where B is FWHM in radians, t is the grain size in nanometers, ε is the strain, λ is the x-ray wavelength in nanometer and C is a correction factor which is taken as 1. The grain size and strain of the as-grown sample were found to be 9.95 nm and 1.265×10^{-3} respectively. After annealing, the grain size increased to 13.9 nm while the strain reduced to 9.05×10^{-4} . Through the annealing process, the strain in ZnO structures was partially relaxed. However, as is seen from the Williamson-Hall plot (Figure 2-7), the strain values are very small and thus their effect on broadening is negligible. Thus, the

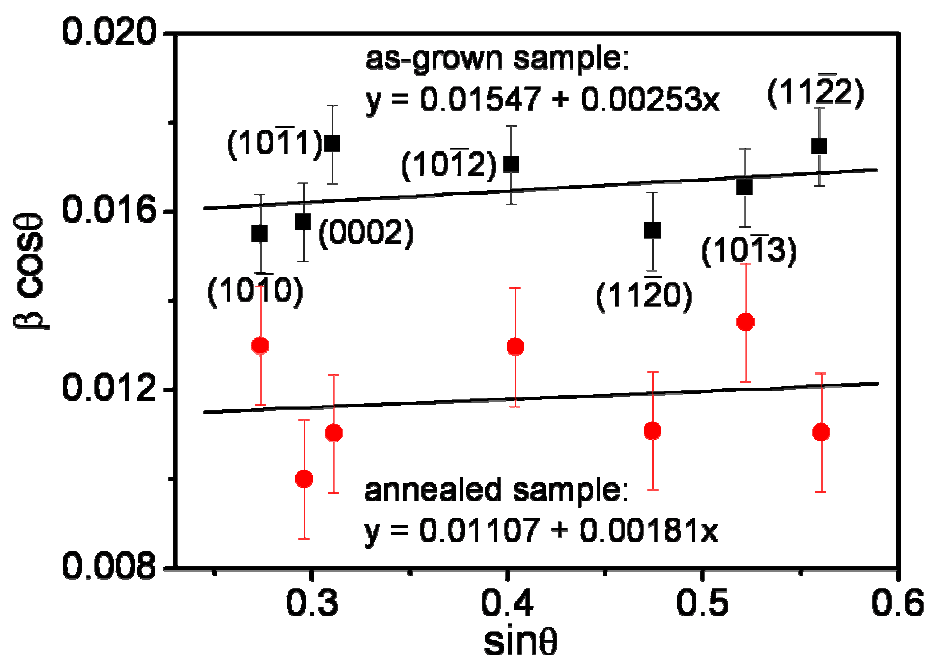


Figure 2-7 Williamson-Hall plots for as-grown and annealed ZnO thin films.

grain size estimation by Scherrer's formula, which is carried out without the consideration of strain relaxation, is accurate for polycrystalline and epitaxial films.^{112,113}

Surface morphology of the ZnO thin films grown by MOCVD was investigated by AFM. Comparison of AFM images of the ZnO thin films grown on quartz substrates at various temperatures are shown in Figure 2-8. The root-mean-square (rms) roughness of the corresponding image is also indicated in Figure 2-8. It can be seen that the surface becomes rougher at the lower growth temperature. The rms roughness of the film grown at 200°C was found to be 7.620 nm, which decreased to 4.284 nm upon increasing the growth temperature to 400°C. The pillar-like characteristic was also found to be weaker as the growth temperature increased, shown in Figure 2-8 (a) to (f). However, when the growth temperature was further increased to 500°C, more pillar-like structures appeared on the ZnO thin film surfaces, [Figure 2-8 (g)]. This is due to (1) violent reaction of precursors DMZn and O₂ at high

temperature, and (2) non-uniformity of films deposition at high growth rate, resulting in more pillar-like structures. After the annealing treatment on the as-grown sample [Figure 2-8 (d)] at 350°C in a mixed N₂ and O₂ ambient, the merging of the nanocrystal clusters enables the recrystallization process to occur. As a result, the rms roughness of the annealed film [Figure 2-8 (h)] was found to be only 2.543 nm, decreased from 5.407 nm for as-grown sample at 350°C.

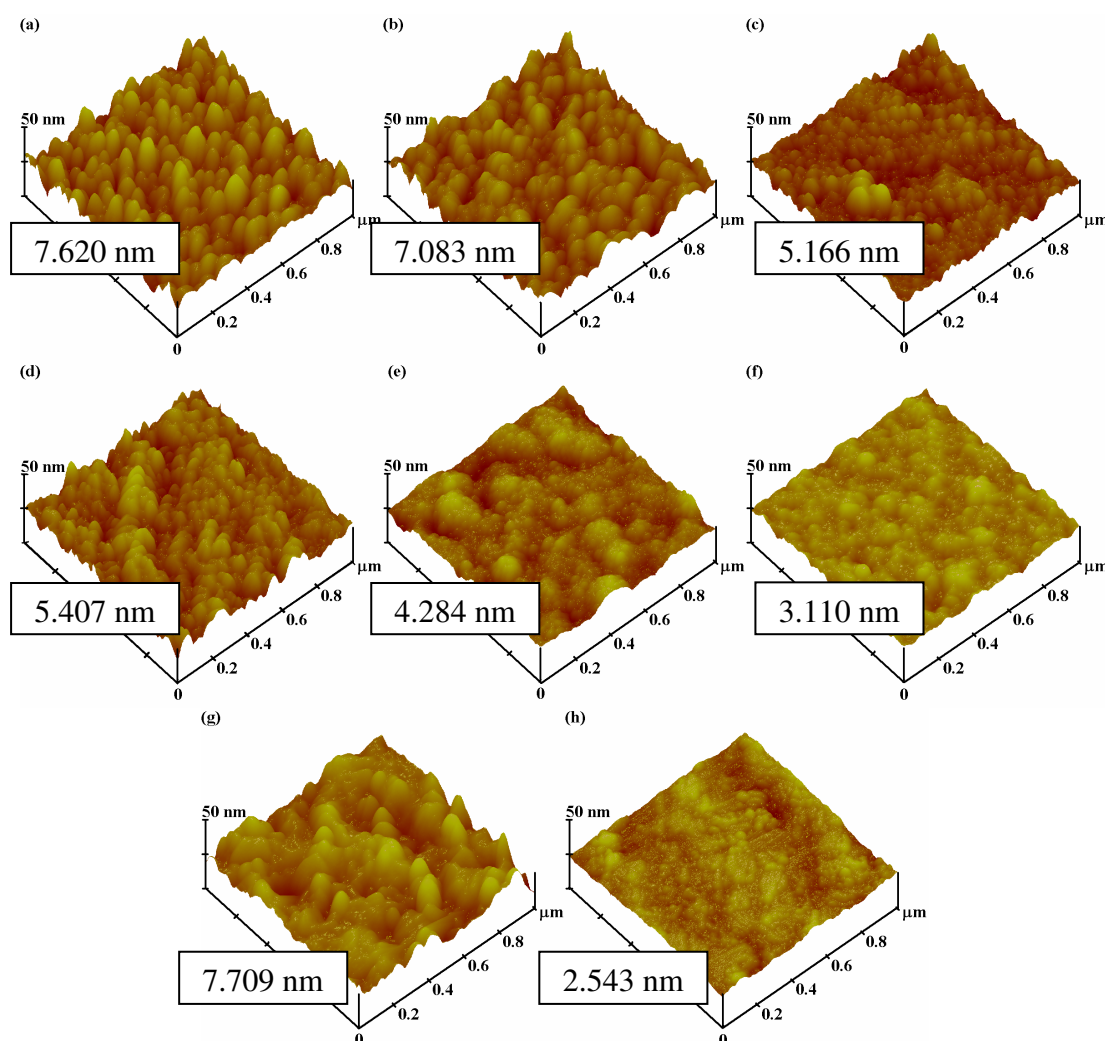


Figure 2-8 AFM images of ZnO thin films grown on quartz substrates at (a) 200°C, (b) 250°C, (c) 300°C, (d) 350°C, (e) 400°C, (f) 450°C, (g) 500°C, and (h) 350°C and annealing at 500°C for 10 minutes. The corresponding rms roughness of the films is indicated in the figure.

Optical transmission spectroscopy has been frequently used to determine the optical transmission/absorption and optical bandgap of semiconductor films. The typical transmission spectra of the ZnO thin films fabricated on quartz substrates at various growth temperatures from 200°C to 500°C are shown in Figure 2-9. The transmittances are over 80% in the visible region for all the samples except for films grown at 450°C, Figure 2-9 (f), and 500°C, Figure 2-9 (g). The interference fringes indicate that all the ZnO thin films had optically smooth surfaces and that the interface with the quartz substrate is also smooth. It can be seen from Figure 2-9 that an absorption tails near 280 nm is present for films grown below 400°C. Also, the absorption edge shifted to shorter wavelength as the growth temperature decreases. This phenomenon can be observed clearly in Figure 2-10, which shows the absorption coefficient as a function of photon energy.

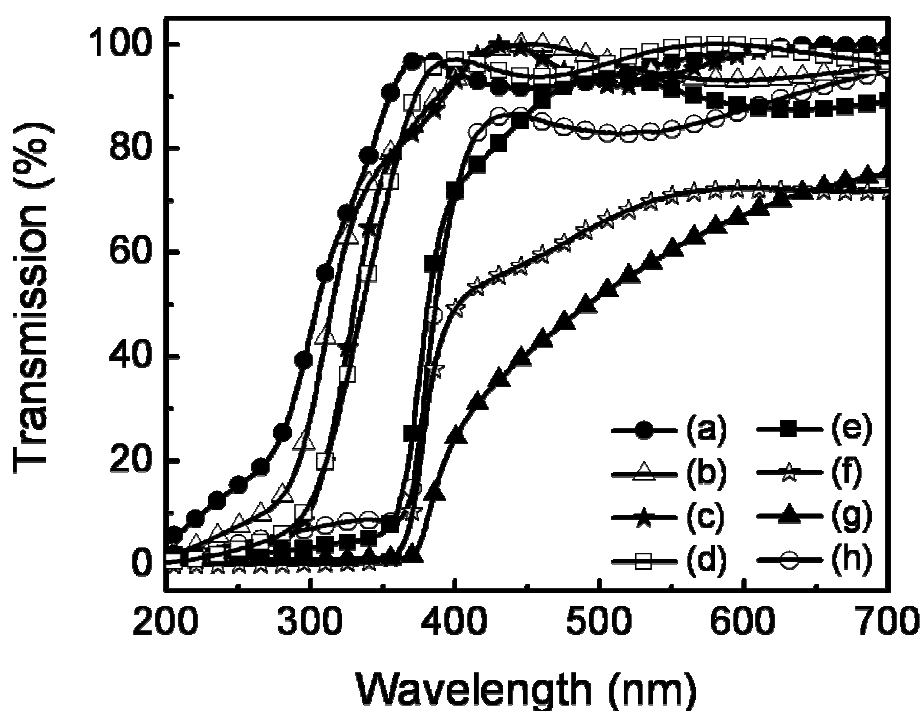


Figure 2-9 Transmission spectra for the ZnO thin films fabricated on quartz substrates at various temperatures, (a) 200°C, (b) 250°C, (c); 300°C, (d) 350°C, (e) 400°C, (f) 450°C, (g) 500°C, (h) grown at 350°C and annealed at 500°C for 10 minutes.

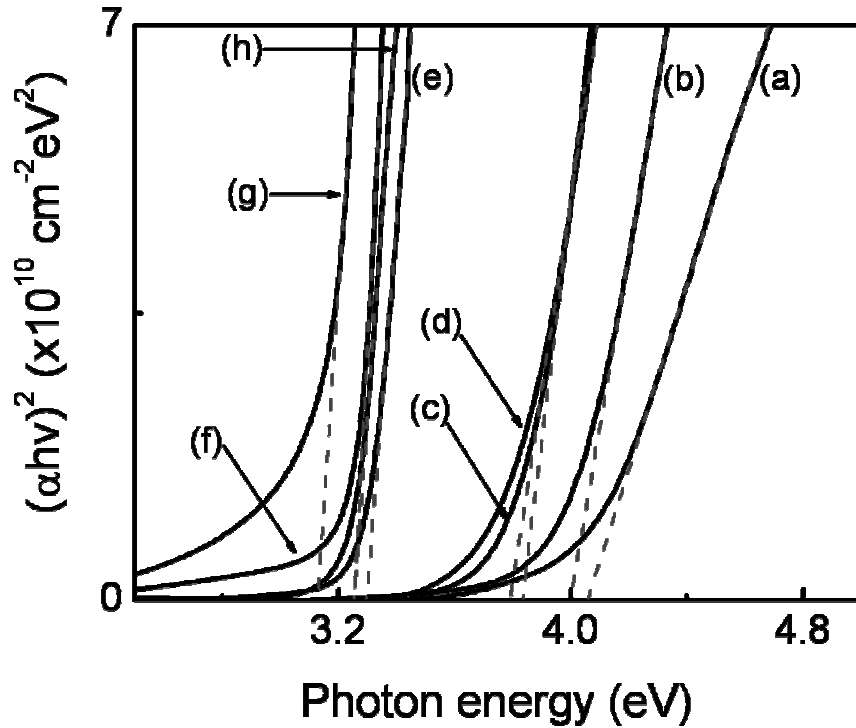


Figure 2-10 Plot of $(\alpha h\nu)^2$ versus photon energy for the ZnO thin films fabricated on quartz substrates at various temperatures, (a) 200°C, (b) 250°C, (c) 300°C, (d) 350°C, (e) 400°C, (f) 450°C, (g) 500°C, (h) grown at 350°C and annealed at 500°C for 10 minutes.

The absorption coefficient α can be calculated by:

$$T = A \exp(-\alpha d) \quad (2.3)$$

where T is the transmittance of thin film, A is a constant and d is the film thickness.

The constant A is approximately unity, as the reflectivity is negligible and insignificant near the absorption edge. The optical bandgap of the films is determined by applying the Tauc model,¹¹⁴ and Davis and Mott model¹¹⁵ in the high absorbance region:

$$\alpha h\nu = D (h\nu - E_g)^n \quad (2.4)$$

where $h\nu$ is the photon energy, E_g is the optical bandgap and D is a constant. For a direct transition, $n = 1/2$ or $2/3$ and the former value was found to be more suitable

Table 2-3 Estimated optical bandgap of ZnO thin films fabricated on quartz substrates at various growth temperatures.

Sample	Growth temperature	Estimated optical bandgap (eV)
(a)	200°C	4.06
(b)	250°C	4.00
(c)	300°C	3.84
(d)	350°C	3.79
(e)	400°C	3.30
(f)	450°C	3.25
(g)	500°C	3.13
(h)	350°C + Annealing at 500°C	3.25

for ZnO thin films since it gives the best linear curve in the band edge region.^{116,117}

The relationship between $(\alpha h\nu)^2$ and $h\nu$ is plotted in Figure 2-10. The E_g value can be obtained by extrapolating the linear portion to the photon energy axis in the figure. The optical bandgap values obtained are summarized in Table 2-3. As the growth temperature was reduced from 500 to 200°C, the optical bandgap blue-shifted from 3.13 eV to 4.06 eV. A similar blue-shift phenomenon of optical bandgap was also observed in ZnO thin film deposited on sapphire substrates.¹¹⁸

It was noticed that if the sample was annealed, there would be a red-shift of the bandgap. Figure 2-9 (d) shows the bandgap for a sample grown at 350°C while Figure 2-9 (h) shows the same sample after annealing. The absorption edge red-shifts from 3.79 eV to 3.25 eV (Table 2-3). The sample grown at 350°C was chosen as an example for clarity. In fact, all the annealed samples showed an optical bandgap of around 3.25 eV.

From the XRD results, we propose that the absorption edge blue-shift is due to the poor crystallinity of ZnO thin films grown at low temperature. The crystallinity of the ZnO thin films grown below 400°C was poor and exhibits polycrystalline structure.

The physical model of the structure can be viewed as various nanocrystalline islands embedded in a matrix of amorphous ZnO. Qualitatively, the interatomic spacing of amorphous structure would be relatively long and more disordered than crystalline structure due to the absence of long-range translational periodicity. As the fraction of amorphous ZnO phase increases in the films grown at low temperature, the extended localization in the conduction and valence bands increases. As a result, the absorption of photon is mainly contributed by amorphous ZnO and hence the absorption edge blue-shifted. On the other hand, for samples grown at higher temperature ($>400^{\circ}\text{C}$), the crystallinity of ZnO thin films becomes better. The optical bandgap reduces to that of the crystalline ZnO.

The PL of the ZnO thin films was measured at room temperature. Figure 2-11 (a) to (g) show the PL spectra for ZnO thin films grown on quartz substrates at temperature from 200°C to 500°C with an increment of 50°C , respectively. Figure 2-11 (h) shows the PL spectrum of the sample grown at 350°C [Figure 2-11 (d)] and annealed at 500°C . The observed fringes were due to the interference effect from the coating of charge coupled device (CCD) detector. All the ZnO thin films have good optical properties as they have strong band edge emission and weak green band emission as shown in Figure 2-11. Also, it can be seen that the luminescence property of the films does not improve proportionally with its crystallinity. This can be observed clearly that the samples grown at 350°C and 400°C [Figure 2-11 (d) and (e)] have stronger band edge emission but poorer crystallinity than the samples grown at 450°C and 500°C [Figure 2-11 (f) and (g)]. This might be due to the forming of trap centers during the growth with higher growth rate at higher growth temperature, which reduces the radiation recombination efficiency. However, the annealing treatment improved luminescence property as shown in Figure 2-11 (h).

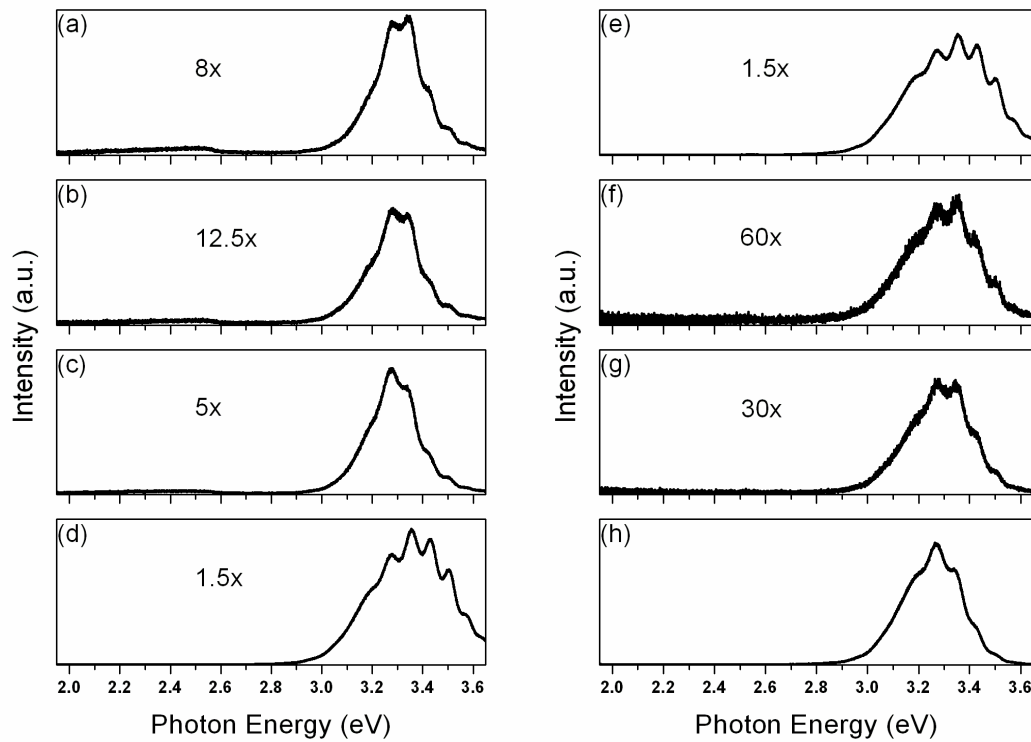


Figure 2-11 Room temperature PL spectra of the ZnO thin films fabricated on quartz substrates at various temperatures, (a) 200°C; (b) 250°C; (c) 300°C; (d) 350°C; (e) 400°C; (f) 450°C; (g) 500°C and (h) 350°C and annealing at 500°C for 10 minutes are shown.

Besides, it can be seen from the Figure 2-11 that all samples exhibit wide band edge emissions ranging from 3 eV to 3.6 eV, especially for the samples grown at 350 and 400°C [Figure 2-11 (d) and (e)]. The wide range of emission spectrum should be due to the nanocrystalline phase, as the amorphous phase should not emit well. The emission by the nanocrystalline structure will have the similar quantum size effect as quantum dots and can be described by the following equation:^{119, 120}

$$E_{(gap,nanocrystal)} = E_{(gap,bulk)} + \frac{\pi^2 \hbar^2}{2R^2} \left(\frac{1}{m_e^*} + \frac{1}{m_h^*} \right) - 0.248 E_{Ryd}^* \quad (2.5)$$

The bulk bandgap, $E_{(gap,bulk)}$ is taken as 3.2 eV¹²¹ and the bulk exciton binding energy, E_{Ryd}^* can be taken as 60 meV.²⁸ According to Beni and Rice (Ref. 122) and

Fan *et al.*,⁵⁷ the electron and hole effective masses are taken as $m_e^* = 0.24m_0$ and $m_h^* = 2.31m_0$, respectively. Additionally, h is the Planck's constant and R is the radius of ZnO nanocrystals.

Figure 2-12 shows a plot of the nanocrystal bandgap, $E_{(gap,nanocrystal)}$ versus the nanocrystal radius, R . The solid curve is the theoretical fit of Eq. (2.5), while the symbols (\circ) are the grain sizes estimated from XRD result (Table 2-2) and their corresponding bandgaps measured from PL. From Figure 2-12, it can be seen that the nanocrystal bandgap of all the samples measured from the PL fits the theoretical curve. It is noticed that, the bandgap does not show much variation with the crystallite size, which corresponds to various growth temperatures (Table 2-2). This is probably because the crystallite size is not small enough to show a marked confinement effect. It is clear from Figure 2-12 that, the PL emission does not show a blue-shift corresponding to the blue-shift in the transmission spectra in Figure 2-9. Hence, the

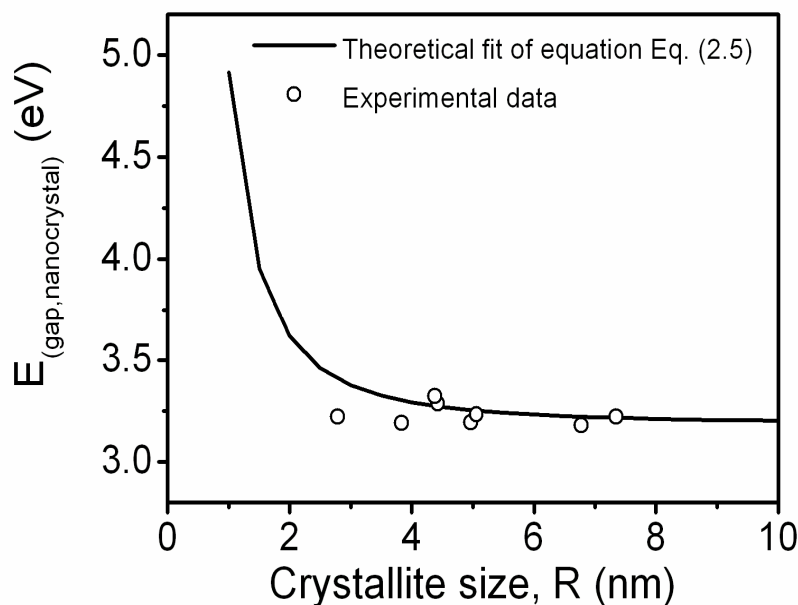


Figure 2-12 Plot of $E_{(gap,nanocrystal)}$ obtained from PL measurement versus the nanocrystal radius R for ZnO thin films grown at various temperatures (\circ) and a theoretical fit using Eq. (2.5).

PL measurement demonstrates that the emission comes from the ZnO nanocrystals, and the blue-shift in the transmission spectra (Figure 2-9) is due to the amorphous phase in the film.

2.3.4 Summary

In summary, the optical bandgap blue-shift of ZnO thin films made of amorphous and nanocrystalline phases was studied. The amorphous phase in ZnO thin films obtained in films deposited at low temperature is believed to be the main reason for the blue-shift of optical bandgap. The estimated optical bandgap of ZnO thin film blue-shifts from 3.13 eV to 4.06 eV as the growth temperature decreased from 500°C to 200°C. The optical bandgap shifts back to normal value after the annealing process. The PL emission does not blue-shift as in the transmission spectra indicating the existence of nanocrystals embedded in the amorphous matrix of the ZnO thin films.

2.4 Quantum Confinement of ZnO Quantum Dots

Embedded Films

2.4.1 Background

As mentioned in previous section, ZnO has relatively high exciton binding energy of 60 meV. In fact, this property makes ZnO a much more interesting and promising material for optoelectronics. It is expected that the significance of the exciton effect will become more prominent in nanostructures especially in zero-dimensional nanostructures, i.e. QDs. Hence, QDs are expected to have many interesting and useful properties for opto-electronic applications, for example, application of QDs in semiconductor lasers, which was firstly proposed by Arakawa and Sakaki [Ref.123] in 1982. Owing to this, ZnO QDs has been synthesized and investigated by various groups in the last decade.^{120,124-127}

The MOCVD reactor setup has been described in previous section and shown in Figure 2-4. As discussed previously, we have shown the blue-shift of optical bandgap due to the amorphous matrix of the ZnO thin films. Also, the slightly blue-shift of the PL peak and broad emission spectra that tail up to 3.6 eV clearly indicates the existence of QDs in the films. In this section, the fabrication and characterization of ZnO QDs embedded films are reported in detail. The dependency of QDs bandgap on dot size is investigated.

2.4.2 Experiment

The ZnO QDs embedded films were grown on Si (100). The Si wafer was cleaned by sequential ultrasonic baths of acetone, ethanol, and rinsed by de-ionized water. Hence, it is expected that a thin layer of oxide will form on the Si wafer especially when the wafer was heated up in the reactor chamber with the presence of

O₂. The growth temperature was set at 350°C. Again, DMZn, N₂ gas and high-purity O₂ were used as the Zn source, carrier gas and oxidizing agent, respectively. By tuning the precursors flow rate, ZnO QDs embedded films or highly c-axis oriented ZnO thin films could be obtained. Here, we chose the sample grown at 3 and 20 sccm of DMZn and O₂ each, respectively for demonstration. The flow rates of the DMZn (N₂ carrier gas) and O₂ were set at 20 sccm each for the QDs fabrication. The DMZn bubbler was kept at -10°C in a coolant water bath. The chamber pressure was maintained at about 30 mbar and the deposition time was 10 minutes. The QDs embedded ZnO thin films grown at 350°C have an average thickness of 290 nm. The sample used in this study has a thickness of 280 nm that was confirmed by the surface profile measuring system (TENCOR P-10). For comparison purpose, a highly c-axis oriented ZnO thin film was grown at 350°C with the flow rate of DMZn (N₂ carrier gas) and O₂ maintained at 3 sccm each. Besides the precursors flow rate, the experiment conditions for growing ZnO QDs and highly c-axis oriented ZnO thin films were exactly the same. The highly c-axis oriented ZnO thin film has a thickness of 260 nm. The growth rate for highly c-axis oriented films is comparable to that of QDs embedded films indicates the excess precursors used in the later growth. In fact, after the growth of QDs embedded films, the stainless steel wall of the reactor chamber was covered with a layer of white particles, which was confirmed as ZnO powder.

The crystal structure of the obtained films was characterized by X-ray diffraction (XRD) measurement with CuK α radiation (Siemens D5005 X-Ray Diffractometer). High-resolution transmission electron microscopy (HRTEM) with accelerating voltage of 300 kV was employed to observe the lattice structure (JEOL 3010). Photoluminescence (PL) of the ZnO thin films was measured with a micro-PL

system excited with the 325 nm line of a He-Cd laser with an output power of 30 mW and detected with a charge-coupled device (CCD) array.

2.4.3 Results and Discussion

Figure 2-13 (a) and (b) show the XRD profiles of ZnO thin films grown at 3 sccm and 20 sccm of DMZn and O₂ each, respectively. From Figure 2-13 (a), it can be seen that the ZnO thin film exhibits highly c-axis oriented structures, while the QDs embedded film is in poor crystallinity and exhibits polycrystalline structure with the existence of various crystallographic planes, as shown in Figure 2-13 (b). By using Scherrer's formula [Eq. (2.3)], the grain sizes corresponding to crystallographic plane (10 $\bar{1}$ 0), (0002), and (10 $\bar{1}$ 1) were estimated to be 3.45, 9.92, and 4.83 nm, respectively.

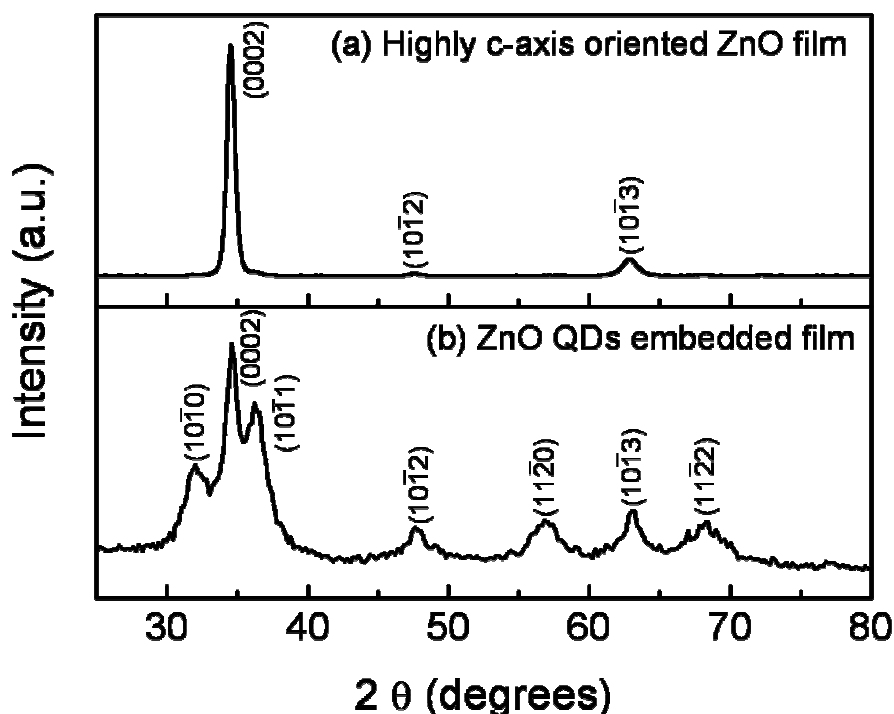


Figure 2-13 XRD profiles of (a) highly c-axis oriented ZnO thin film and (b) ZnO QDs embedded film.

The crystallite size estimated from the XRD was further proved by employing the HRTEM. The HRTEM images of the ZnO QDs embedded film grown on Si (1010) are shown in Figure 2-14. As seen from Figure 2-14 (a), the QDs are found embedded in the ZnO thin film grown on Si substrates. The size distribution of ZnO QDs embedded film can be observed clearly in the lower magnification of the HRTEM image, as shown in Figure 2-14 (b). The QDs were uniformly distributed in the film and the size of the QDs measured was in the range of 3 to 12 nm. The QDs size was estimated from Figure 2-14 (b) and the distribution was plotted as histogram as shown in Figure 2-15. The dashed curve is the Gaussian fitting of the QDs distribution. Most QDs were distributed at around 7 nm in diameter. The measured QDs sizes are in good agreement with the grain size estimated by using the Scherrer's formula from XRD data.

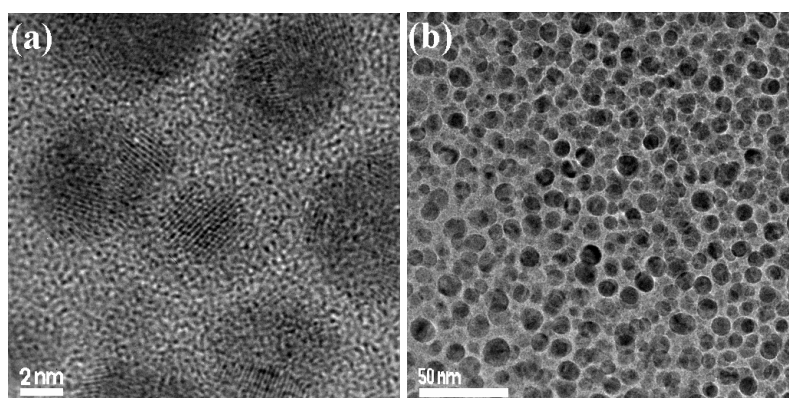


Figure 2-14 HRTEM images with (a) high magnification and (b) lower magnification of the ZnO QDs embedded film fabricated on Si substrates.

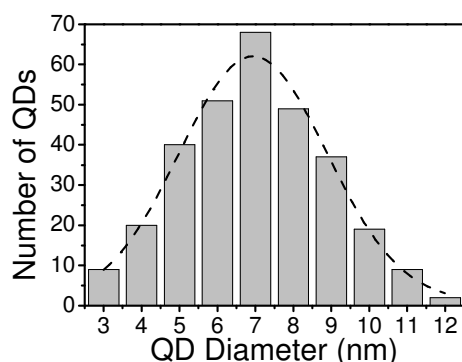


Figure 2-15 Histogram of ZnO QDs distribution measured from Figure 2-14 (b). The dashed curve is the Gaussian fit of the ZnO QDs distribution.

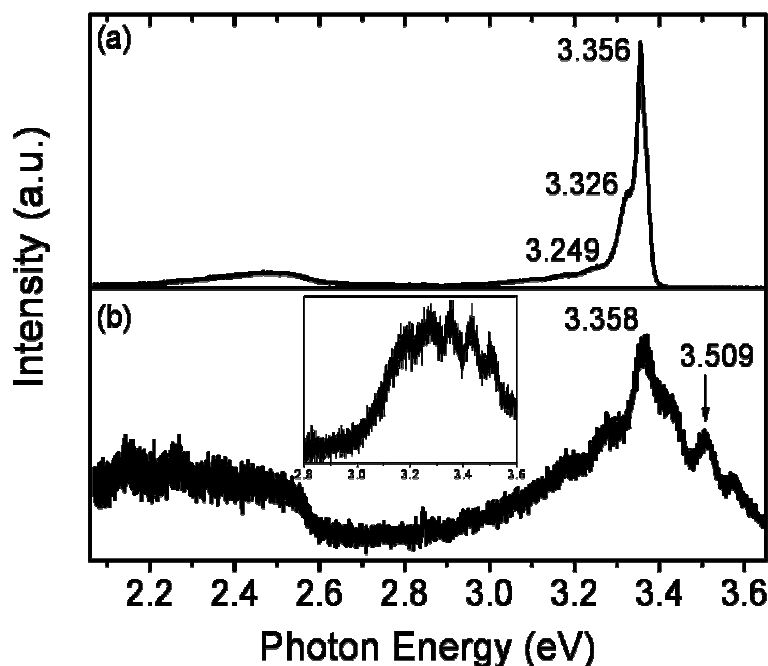


Figure 2-16 PL spectra of (a) highly c-axis oriented ZnO thin film and (b) ZnO QDs embedded film measured at temperature of 80 K. The inset shows the room temperature PL of the QDs embedded film.

In order to examine the quantum confinement of the ZnO QDs embedded films, PL measurement at temperature of 80 K was carried out. Figure 2-16 (a) and (b) show, respectively, the PL of the highly c-axis oriented ZnO thin film and QDs embedded film. The inset of Figure 2-16 (b) shows the room temperature PL of QDs embedded film. The PL spectrum of the highly c-axis oriented ZnO thin film shown in Figure 2-16 (a) is dominated by the near-band-edge emission (NBE) at 3.356 eV, which is attributed to the neutral donor-bound exciton (D^0X). The shoulder peaks at 3.326 and 3.249 eV are attributed to the deep bound exciton and donor-acceptor pair (DAP) emissions.^{128,129} The spectrum, however, shows drastic difference for QDs embedded film, as shown in Figure 2-16 (b). The emission spectrum of the QDs embedded film measured at 80 K shows a broad NBE with a tail up to 3.6 eV and peaking at around 3.358 eV, which is attributed to D^0X . As the transverse optical (TO) and longitudinal optical (LO) phonon energy is 51.3 and 71.9 meV [Ref. 130],

respectively, the shoulder peaks observed on the spectrum [Figure 2-16 (b)] are clearly not the phonon-assisted emission. Since the room temperature PL of the QDs embedded film also exhibits several peaks [Figure 2-16 (b) inset], we believed that these shoulder peaks are due to the interference effect from the coating of CCD detector. However, comparing the PL of QDs embedded film measured at 80 K and room temperature [Figure 2-16 (b)], there is an obvious change in the NBE shape. At temperature of 80 K, the emission peaks at 3.358 eV (D^0X) and 3.509 eV can be identified even with the presence of the interference noise.

The quantum confinement effect of the band tail emission could be observed from PL measurement and the size-dependence of the QDs bandgap ($E_{(gap,QDs)}$) can be described by the following equation:^{119,120}

$$E_{(gap,nanocrystal)} = E_{(gap,bulk)} + \frac{\pi^2 \hbar^2}{2R^2} \left(\frac{1}{m_e^*} + \frac{1}{m_h^*} \right) - 0.248 E_{Ryd}^* \quad (2.6)$$

The bulk bandgap, $E_{(gap,bulk)}$ is taken as 3.377 eV and the bulk exciton binding energy, E_{Ryd}^* is taken as 60 meV. According to Beni and Rice [Ref. 122] and Fan *et al.*⁵⁷, the electron and hole effective masses are taken as $m_e^* = 0.24 m_0$ and $m_h^* = 2.31 m_0$, respectively. Additionally, \hbar is the Planck's constant and R is the radius of ZnO QDs. Using the Eq. (2.5), the QDs bandgap ($E_{(gap,QDs)}$) of the dot size of 3 to 12 nm was calculated to be 4.130 to 3.425 eV, respectively. Owing to the fact that Eq. (2.5) was derived with the assumption that the electrons and holes are completely confined in the well by the infinite potential barrier, the actual quantum confinement effect should be less significant, as is seen in Figure 2-16 (b). Besides, due to the presence of smaller percentage of 3 nm QDs, as shown in Figure 2-15, their contribution to the emission is weak. Hence, its corresponding emission could not be

observed in the PL measurement. Meanwhile, for the most distributed QDs with diameter of 7 nm shown in Figure 2-15, the corresponding emission calculated was 3.503 eV. It can be seen from Figure 2-16 (b) that the emission peak at 3.509 eV, due to 7nm QDs, can be clearly identified even with the presence of interference.

Other than the NBE, the deep-level emission (DLE) was observed for both the highly c-axis oriented and QDs embedded ZnO thin films as shown in Figure 2-16. The DLE for highly c-axis oriented ZnO thin film peaking at 2.5 eV while the QDs embedded film has a DLE centered at 2.26 eV. It is generally accepted that the DLE at around visible spectrum is attributed to the recombination of a photogenerated hole with electron in singly ionized oxygen vacancy in ZnO thin film.^{19,120,131} Ratio of NBE to DLE is always used to evaluate the concentration of structural defects in ZnO thin films. The NBE to DLE ratio of the highly c-axis oriented film is 17 while for the QDs embedded film is only about 2. The PL efficiency of the QDs embedded films is inferior, which is expected. The incorporation of the nanocrystals deteriorates the crystallinity of the films, which in turn degrades the luminescence efficiency. The defects concentration is expected to be higher in the QDs embedded films compared to highly c-axis oriented film. Moreover, with a comparable thickness of both samples, the PL of the QDs embedded film is much inferior due to the fact that the amorphous ZnO (matrix) should not emit well.¹¹⁶

The relative quantum yield of the highly c-axis oriented and QDs embedded ZnO thin films was estimated by integrating the area under the PL spectra. The quantum yield of the QDs embedded film is around 5 % compared to the highly c-axis oriented ZnO thin films. The quantum yield is low due to the fact that the QDs embedded films are poor in crystallinity. Also, it is worth mentioning that even the thickness of the two films is about the same, the relative quantum yield could not

reveal the actual quantum efficiency of the QDs embedded film. This is because the QDs embedded film is in the form of ZnO nanocrystals embedded in the ZnO amorphous matrix. In other words, most of the phase in QDs embedded film is amorphous rather than crystalline. As a result, the PL efficiency of the ZnO QDs embedded films is definitely poorer than those crystalline films since amorphous phase should not emit well. Therefore, in our opinion, the relative quantum yield (5 % in this case) of the QDs embedded film compared to highly c-axis oriented ZnO thin films could be underestimated.

2.4.4 Post-growth Thermal Annealing on ZnO QDs Embedded Films

Figure 2-17 (a) shows the room temperature PL of the ZnO as-grown QDs embedded film. The PL of the post-growth annealed films, carried out at 800°C in atmosphere for 10, 30, 60, and 90 seconds are shown in Figure 2-17 (b) to (e), respectively. The PL intensity increased by a factor of 10 upon the annealing for 90 s. It is noticed that the quantum confinement effect (photon energy greater than line B) decreased as the annealing time increased and completely disappeared after 90 s of annealing. While the intensity at the lower energy band (photon energy smaller than line A) gradually decreased as the annealing time increased. The change in PL is related to the crystallinity of the ZnO thin films. The QDs that embedded in the films were combined and formed larger grains upon annealing. Hence, the quantum confinement effect completely disappears after the annealing for 90 s. The decrease in intensity at the lower energy band (photon energy smaller than line A) is correlated to the crystallinity. Generally, the amorphous phase semiconductor has an ambiguous bandgap due to the extended localization in the conduction and valence band.¹¹⁸ The post-growth annealing enhanced the film crystallinity and in turn decreased the

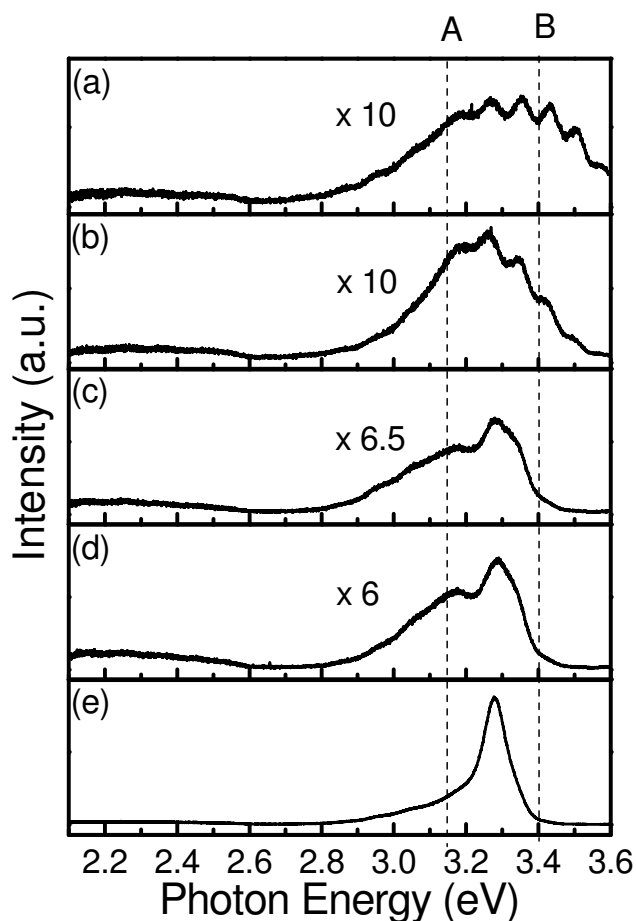


Figure 2-17 Room temperature PL of QDs embedded films annealed at 800°C for (b) 10, (c) 30, (d) 60, and (e) 90 s, respectively. Room temperature PL of as-grown ZnO QDs embedded film is shown in (a) for reference.

localization in the conduction and valence band. As a result, the radiative recombination through defects decreased and the free exciton recombination increased after the post-growth annealing.

2.4.5 Growth Mechanism of ZnO QDs Embedded Films

From XRD measurement (Figure 2-13), it can be seen that as the precursors flow rate increased from 3 to 20 sccm each, the film crystallinity degraded significantly. We proposed that the QDs are formed in gaseous phase and then incorporated into the ZnO thin film during the growth. The proposed growth

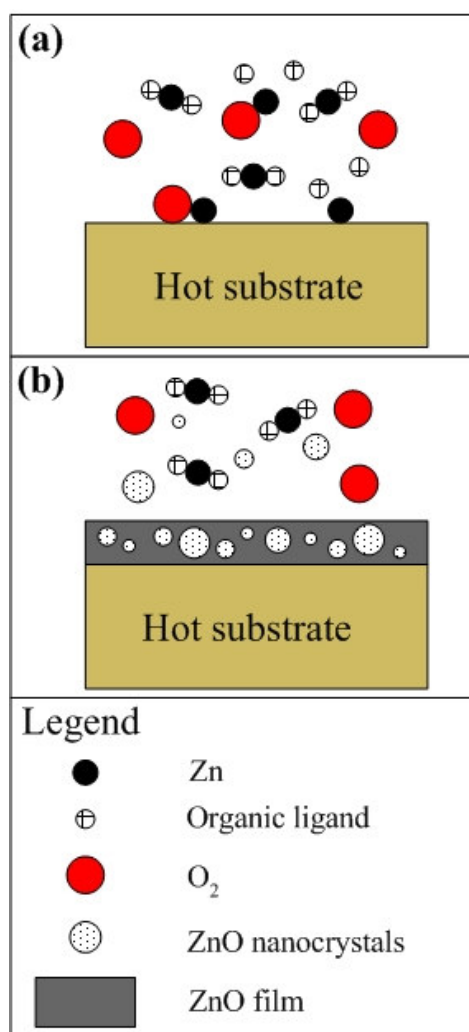


Figure 2-18 Growth mechanism of the ZnO QDs embedded film. (a) Arriving of the precursors on the hot substrate. (b) Pre-reaction of the precursors facilitates the formation of nanocrystals, and in turn incorporates into the ZnO thin film.

mechanism is illustrated in Figure 2-18. It is well known that the DMZn reacts vigorously with oxygen even at room temperature.¹³² Hence, the pre-reaction of the precursors can easily happen during the growth, especially when a large amount of precursors is introduced into the chamber, as shown in Figure 2-18. The pre-reaction of the precursors in gaseous phase facilitates the formation of nanocrystals, which is then incorporated into the ZnO thin film [Figure 2-18 (b)]. The QDs formed in gaseous phase and incorporated in the film during the growth, resulting in poor film crystallinity, as shown in Figure 2-13 (b). Also, as the incorporation of the ZnO QDs

takes place randomly, the various crystallographic planes were formed and detected, which are similar to ZnO powders detection.¹¹⁰ In fact, white ZnO nanocrystals were deposited on the stainless steel wall of the reactor chamber after the experiment, suggesting a severe pre-reaction that occurs during the growth and therefore leads to the formation of ZnO QDs embedded films. The formation of QDs embedded in film grown on quartz and sapphire substrates was also observed in our work.^{116,118} Hence, it is very clear that the formation of QDs is independent of the substrates. This acts as a strong evidence that the QDs are formed in gaseous phase, which is due to the pre-reaction of the precursors.

2.4.6 Summary

ZnO QDs embedded films were fabricated by MOCVD. The QDs were incorporated into the films during the growth due to the vigorous reaction of the precursors. The QDs size ranged from 3 to 12 nm was found embedded in film from the HRTEM characterization. The PL spectrum measured at 80 K shows that the broadening of NBE with a tail up to 3.6 eV is due to the quantum confinement effect of the QDs. Post-growth thermal annealing was carried out on the ZnO QDs embedded films. As expected, the quantum confinement effect was quenched by post-growth thermal annealing, which is due to the ripening or coarsening of the QDs.

CHAPTER 3 HIGHLY C-AXIS OERIENTED ZNO THIN FILMS BY MOCVD

3.1 Reactor Design Investigation

In previous chapter, we have shown the ZnO thin films deposited with various growth conditions. Nevertheless, epitaxy growth of the ZnO thin films has not been demonstrated even with sapphire substrates. The pre-reaction of Zn precursor and O₂ has greatly affected the crystallinity of the ZnO thin films. In fact, the pre-reaction of Zn precursor and O₂ has facilitated the formation of a homogeneous ZnO QDs embedded films as discussed in the previous chapter.¹¹⁸ In order to obtain high quality ZnO thin films, the pre-reaction of the precursors in gaseous phase has to be minimized or even eliminated by modifying the growth reactor and growth process.

During the course of the reactor design, crystallinity and optical property are used to qualify the effectiveness of the reactor design. Figure 3-1 depicts the reactor with different design of precursors flow configuration, (a) original, (b) modification #1, and (c) modification #2 configuration, respectively. The original precursors flow configuration was designed such that the precursor DMZn and O₂ were flow parallel to the substrates. For modification #1 reactor [Figure 3-1 (b)], the direct flow tube of

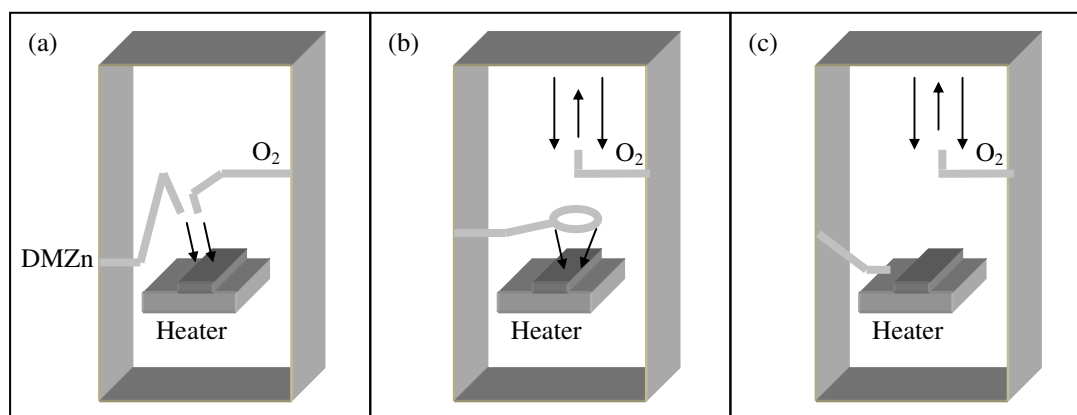


Figure 3-1 Reactor with different design of precursors flow configuration, (a) original, (b) modification #1, and (c) modification #2 configuration.

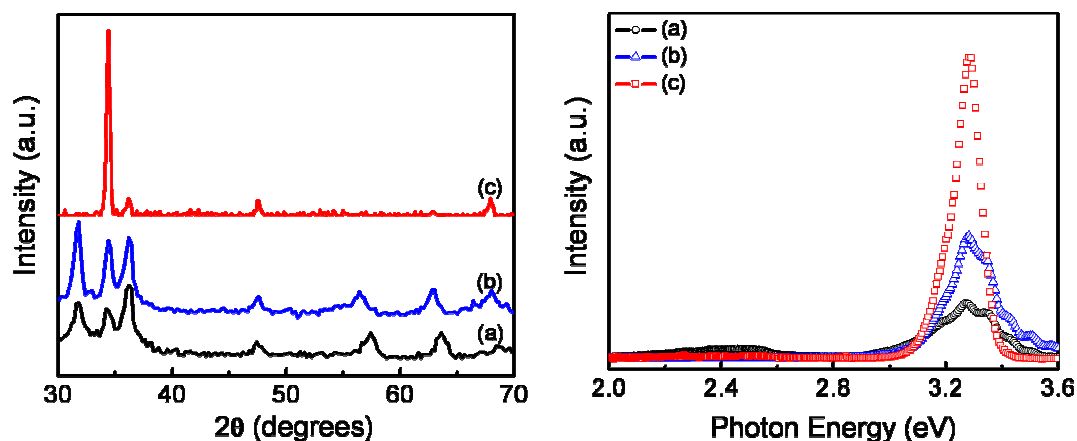


Figure 3-2 XRD (left) and PL (right) of ZnO grown on sapphire substrates by (a) original, (b) modification #1, and (c) modification #2 reactor design.

precursor DMZn was changed to a circular flow tube and placed on top of the substrates. Also, the O_2 flow was directed upward for more uniform O_2 supply. Figure 3-1 (c) shows the modification #2 reactor configuration. For this design, the flow of precursor DMZn was directed horizontally towards the substrate in order to simulate a laminar flow and hence restrict the chemical reaction on the substrate surface.

Figure 3-2 shows the XRD and PL of ZnO thin films grown on sapphire by (a) original, (b) modification #1, and (c) modification #2 reactor, respectively. The flow rate for both DMZn and O_2 were fixed at 10 sccm and the growth temperature was fixed at 350°C for the experiments. It is seen that the XRD of ZnO thin films grown by original and modification #1 reactor exhibit polycrystalline structures with no preferential orientation of crystal growth. By using modification #2 reactor, the crystallinity of the ZnO thin films shows great improvement with a highly c-axis orientation.

Room temperature PL was carried out to investigate the emission property of the ZnO thin films grown with various reactor designs, as shown in Figure 3-2. The broad PL emission that tail up to 3.6 eV of the ZnO thin films grown by original and

modification #1 reactors is due to the quantum confinement effect of ZnO QDs, as described in the previous chapter. The XRD and PL measurements clearly indicate that the pre-reaction was severe during the growth in original and modification #1 reactors. While for the films grown by modification #2 reactor, the PL spectrum shows great improvement in excitonic-related emission and no tail emission is observed. This strongly suggests that the ZnO thin films grown by modification #2 reactor have better structural and optical properties. However, the pre-reaction of Zn precursor and O₂ in gaseous phase is yet to be totally eliminated by modification #2 reactor.

3.2 Highly c-axis Oriented ZnO thin films

3.2.1 Experiment

In previous section, we have shown that the modification #2 reactor is capable of growing high quality ZnO thin films. However, the growth was not optimized and hence the ZnO thin films suffer from the pre-reaction of the precursors. In order to obtain high quality epitaxial films, the growth process has been modified to eliminate the pre-reaction of the precursors. In the modified growth process, the O₂ source for the growth of ZnO thin films was obtained from the residual gas inside the chamber rather than continuously supplying O₂ gas. The chamber was firstly evacuated to 5×10^{-2} Torr, and the growth was then conducted at 350°C for 10 minutes under a pressure of 25 Torr with N₂ background gas. The flow rate of the DEZn was maintained at 6 sccm and the DEZn source was kept at 5°C in a coolant water bath.

The crystal structure was characterized by x-ray diffraction (XRD) using Siemens D5005 x-ray diffractometer with CuK α radiation. The photoluminescence (PL) spectra of the ZnO thin films were measured with a rapid photoluminescence

mapping system (Accent RPM2000). The optical transmission spectra were measured with a UV-2501PC spectrophotometer at room temperature. The surface morphology of the ZnO thin films was investigated by a Digital Instruments NanoScope IIIa atomic force microscopy (AFM). Electrical resistivity, carrier density and mobility were measured with a magnetic field of 0.32 T by a four-point probe van der Pauw method at room temperature.

3.2.2 Results and Discussion

Highly c-axis oriented ZnO thin films have been fabricated using the modified reactor and growth process. The typical properties of the ZnO thin films are shown in

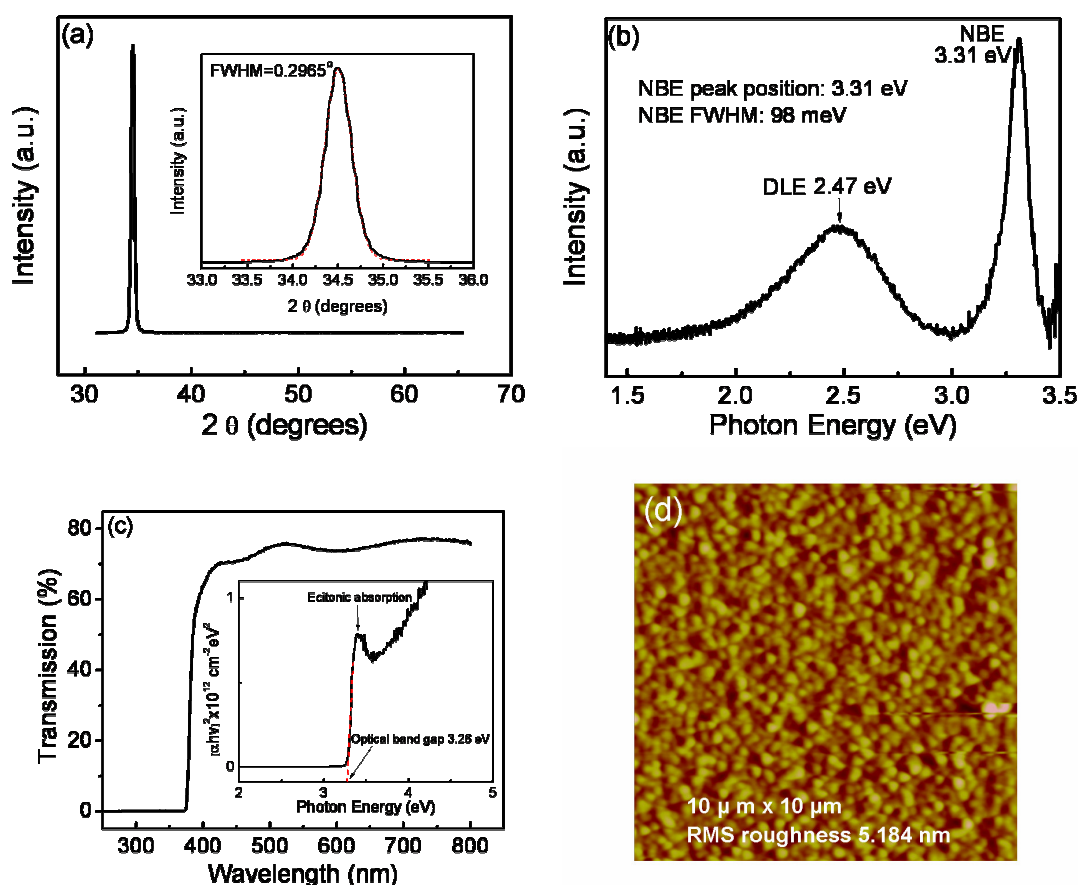


Figure 3-3 Typical Properties of highly c-axis oriented ZnO thin films grown by MOCVD. (a) XRD profile with an inserted enlarged spectrum of (0002) peak; (b) Room temperature PL spectrum; (c) Transmission spectrum with an inserted absorption spectrum; and (d) AFM morphology on the ZnO thin films.

Figure 3-3. Figure 3-3 (a) shows the typical XRD profile of the as-grown ZnO thin films grown on sapphire substrates. The enlarged spectrum of (0002) peak was inserted with a Gaussian fitting. The FWHM of the (0002) peak was determined to be 0.2965 degrees.

Figure 3-3 (b) shows the typical room temperature PL of the as-grown ZnO thin films. The ZnO thin films, excited by the 325 nm line of a He-Cd laser (1.8 mW), exhibit two emission bands that commonly observed in other ZnO thin films. The near-band-edge emission (NBE) positioned at 3.31 eV with a FWHM of 98 meV is an excitonic-related emission. The broad deep-level emission (DLE) centered at 2.47 eV is generally attributed to the radiative recombination of a photogenerated hole with an electron in singly ionized oxygen vacancy in ZnO thin films.^{19,131,133}

The optical transmission measurement was carried out to examine the transmittance and optical bandgap of the ZnO thin films. Figure 3-3 (c) shows the typical transmission spectrum with an inserted absorption spectrum. The as-grown ZnO thin films are highly transparent in the visible wavelength region. The typical transmittance is about 80 % as shown in Figure 3-3 (c). From the insert in Figure 3-3 (c), the excitonic absorption was clearly observed in the as-grown ZnO thin films and the optical bandgap was determined to be 3.26 eV by using the Eq. (2.4).

The surface morphology of the typical as-grown ZnO thin films were characterized by AFM and shown in Figure 3-3 (d). As is seen, the as-grown ZnO thin films are in granular form with a rms surface roughness of 3 ~ 8 nm.

3.2.3 Summary

From the experimental results, it is seen that the ZnO thin films grown by the modified reactor and growth process exhibit good optical and structural properties.

CHAPTER 3 HIGHLY C-AIXS ORIENTED ZNO THIN FILMS BY MOCVD

The obtained ZnO thin films were highly c-axis oriented but epitaxial growth is yet to be established. The possible reasons of not getting epitaxial films could be due to the non-uniform growth that arised from the non-rotational substrate holder and non-laminar flow of precursors. Depsite of the over-simplified growth reactor, the optical quality of the fabricated ZnO thin films is comparable to that of single crystalline ZnO thin films. The design of experiments in growth reactor provides not only the knowledge and physics on the growth behaviour of ZnO material, but more importantly, it provides a firm guideline for the design of second generation MOCVD system.

3.3 *Post-growth Thermal Annealing on Highly c-axis*

Oriented ZnO thin films

Thermal annealing is an important post-growth treatment that has been applied in many fields such as metallurgical and semiconductor industry. Typically, it results in softening of the metal through removal of defects and the internal stresses caused by the defects. In semiconductor industry, the controlled addition of impurities to alter the properties of a semiconductor, which is also known as doping, is one of the most important technologies. Most of the semiconductor films are annealed in order to activate the dopant atoms and hence change the conductivity. Other than the traditional applications, there are reports on fabrication of nanostructures by thermal annealing.^{134,135} The study on coarsening process of MOCVD grown ZnO thin films will be beneficial in understanding the processes in improving film quality and dopants activation, which are crucial for ZnO optoelectronic devices, such as LEDs and LDs. Especially, as proved in practice, MOCVD is the most viable tool for LEDs and LDs. However, it is lack of study on the coarsening process of MOCVD grown ZnO by thermal annealing.

Generally, Ostwald ripening is one of the coalescence phenomena that always associates with thermal annealing treatment and has been studied for over a decade.¹³⁶ Lifshitz and Slyozov [Ref. 137] and later Wagner,¹³⁸ developed an analytic mean-field theory, which is also known as LSW theory to describe the coarsening kinetics. The theory predicts the mean radius of particles increases as:

$$\bar{r}^3(t) - \bar{r}^3(t_0) = K_{LSW} (t - t_0) \quad (3.1)$$

where $\bar{r}^3(t_0)$ and $\bar{r}^3(t)$ are the mean radius of particles at time t_0 and t , respectively, and K_{LSW} is a temperature and material dependence constant. The LSW theory also

predicts that the particle size distribution (PSD) exhibits the self-similarity behavior when it is scaled by the mean particle size.

Although the LSW theory was built with several premises such as spherical shape of particles, near zero volume fraction, and diffusion-growth without convection, those premises generally do not alter the power law of coarsening [Eq. (3.1)].¹³⁹⁻¹⁴⁴ In this section, the morphology evolution of ZnO thin films from nanosheets to nanoneedles structures by post-growth thermal annealing is reported and discussed. The LSW theory is employed to estimate the activation energy of the coarsening process. Also, the electrical and optical properties of the ZnO thin films are investigated and correlated to the coarsening.

3.3.1 Experiment

The ZnO thin films used in the post-growth thermal annealing were deposited on sapphire [Al_2O_3 (0001)] substrates by MOCVD at 350°C. The film thickness was controlled at around 300 nm and confirmed by the Tencor P-10 surface profiler. The detail growth has been described in the previous section.

The ZnO thin films used in this study were grown in a Zn-rich condition. Energy-dispersive x-ray spectroscopy (EDX) attached to the scanning electron microscopy (SEM) was employed to determine the element composition of the ZnO thin films. It was found that the Zn/O ratio for the as-grown film was 1.5868, indicating the film is not stoichiometric, and formation of zinc sub-oxide (ZnO_x , where $x < 1$). In fact, the zinc sub-oxide films have been reported by several groups with various growth techniques.¹⁴⁵⁻¹⁴⁷ It is worth mentioning that the Zn/O ratio is not exactly determined from the EDX result, it provides only a clue for non-stoichiometry. The as-grown sample was cut into pieces and one of them was used as a reference of

the as-grown sample. The rest of the samples were annealed in a temperature range from 600 to 900°C with an increment of 100°C. The post-growth thermal annealing was performed in a N₂ ambient and at atmospheric pressure for 1 hour. The samples were loaded into the heated chamber and pulled out immediately after the annealing and kept in the N₂ ambient to cool down.

The surface morphology of the ZnO thin films was investigated by a JEOL JSM-6700F field-emission gun scanning electron microscopy (FEG-SEM) and Digital Instruments NanoScope IIIa atomic force microscopy (AFM). The crystal structure was characterized by x-ray diffraction (XRD) using Siemens D5005 x-ray diffractometer with CuK α radiation. Electrical resistivity, carrier density and mobility were measured with a magnetic field of 0.32 T by a four-point probe van der Pauw method at room temperature. The photoluminescence (PL) spectra of the ZnO thin films were measured with Renishaw 2000 micro-PL setup excited with a 325 nm line of He-Cd laser at room temperature.

3.3.2 Results and Discussion

The SEM topographs of the as-grown ZnO thin films, and subsequently annealed at 600, 700, 800, and 900°C for 1 hour are presented in Figure 3-4 (a) to (e), respectively. The topographs at the left hand side show the topography of the surfaces while those at the right hand side show the topographs taken with a tilted angle of 45°. It can be observed from Figure 3-4 (a) that the surface morphology of the as-grown film consists of nanosheet structures, with an average thickness of less than 30 nm. It is also noticed that there are some spherical crystallites with radius ranging from 10 to 50 nm distributed in the matrix of nanosheets. After annealing at 600°C, most of the nanosheets remained [Figure 3-4 (b)]. However, it is observed that the size and

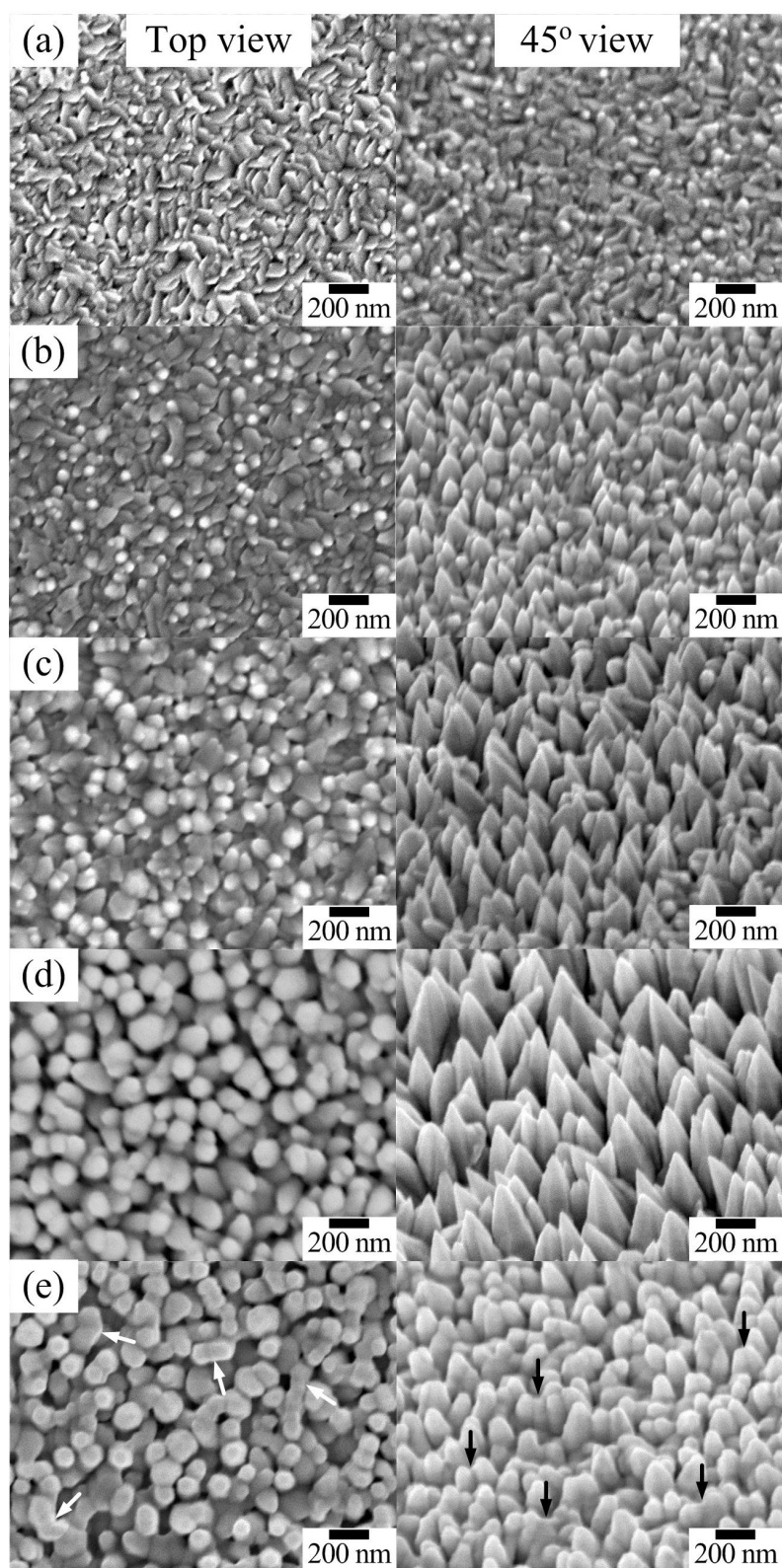


Figure 3-4 SEM topographs of (a) as-grown ZnO thin films and subsequently annealed at (b) 600°C, (c) 700°C, (d) 800°C, and (e) 900°C. The topographs at the left hand side show the topography of the surfaces while those at the right hand side show the topographs taken with a tilted angle of 45°. Arrowheads in (e) show the necks connecting two islands. All the scale bars are 200 nm in length.

density of the spherical crystallites increases. The diameter of the crystallites of the film annealed at 600°C is in the range of 50 to 80 nm. As the annealing temperature increased to 700°C, the surface morphology of the film changed completely from nanosheets to fine three-dimensional (3D) nanoneedles and became well developed at 800°C as shown in Figure 3-4 (c) and (d), respectively. The nanoneedles have an average base diameter ranging from 150 to 200 nm. The diameter of the needles decreased as the height is building up, resulting in the tip sharpening as observed in the tilted SEM topograph. Interestingly, quasi-hexagonal shape of the nanoneedles can be observed in the tilted SEM topograph, which reveals the wurtzite structures of the ZnO crystal. From the tilted SEM topograph [Figure 3-4 (d)], the average height of the nanoneedles can be estimated to be in the range of 200 to 300 nm. With further temperature increment to 900°C, the nanoneedles show little difference with the one annealed at 800°C from the SEM topograph. Nevertheless, it is observed that the height of the nanoneedles reduced and the tip of the needles changed to dome shape. Some joints or necks connecting two or more islands as indicated by the arrowheads in Figure 3-4 (e) are also observed.

The AFM topographs of the films were also taken in order to observe the height and roughness evolution with annealing temperature. The AFM topographs of the as-grown and annealed films are shown in Figure 3-5 with a scanning area of 2 $\mu\text{m} \times 1 \mu\text{m}$. The inset in Figure 3-5 (a) shows a color scale bar with a maximum height of 300 nm for all samples. The root-mean-square (rms) roughness of the ZnO thin films was measured using the Nanoscope III software (attached to the AFM machine) and indicated in the figure too. It is clearly seen from the AFM topographs [Figure 3-5 (b) to (d)] that, the height and size of nanoneedles is building up as the annealing temperature is increased from 600 to 800°C. It should be noted that the tips

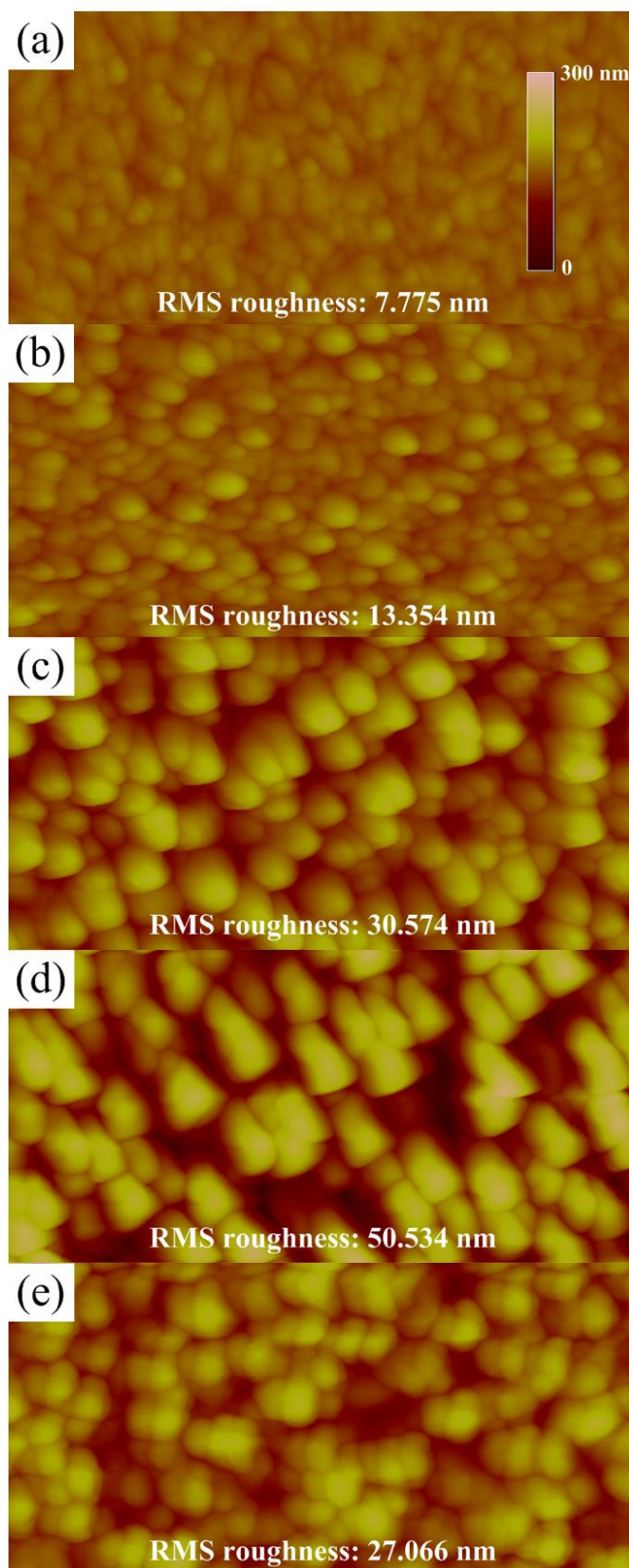


Figure 3-5 2 $\mu\text{m} \times 1 \mu\text{m}$ AFM topographs of (a) as-grown ZnO thin films and subsequently annealed at (b) 600°C, (c) 700°C, (d) 800°C, and (e) 900°C. All the topographs share the same color scare bar with the maximum height of 300 nm and the corresponding rms roughness of the films is indicated in the figure.

of the sample annealed at 700 and 800°C are too sharp to be resolved by AFM. Hence the AFM topographs do not reveal the exact morphology, as we can compare with the SEM topographs. Nevertheless, the density and height of the nanoneedles can still be well identified and represented in the topographs. As the temperature was further increased to 900°C, the height and size of the nanoneedles decreased compared to the one annealed at 800°C. The sample annealed at 800°C has a rms roughness of 50.534 nm, which is much larger than that of the as-grown film (7.775 nm). The rms roughness of the film annealed at 900°C decreased to 27.066 nm due to the tip flattening as observed in SEM topographs.

X-ray diffraction was carried out to confirm the crystal structure of the films. The XRD data of the as-grown ZnO thin films and those subsequently annealed at various temperatures are shown in logarithm scale in Figure 3-6. The inset shows the peak position of (0002) orientation with its corresponding full width at half maximum (FWHM). It can be seen from Figure 3-6 that, all the films exhibit strong (0002) peak

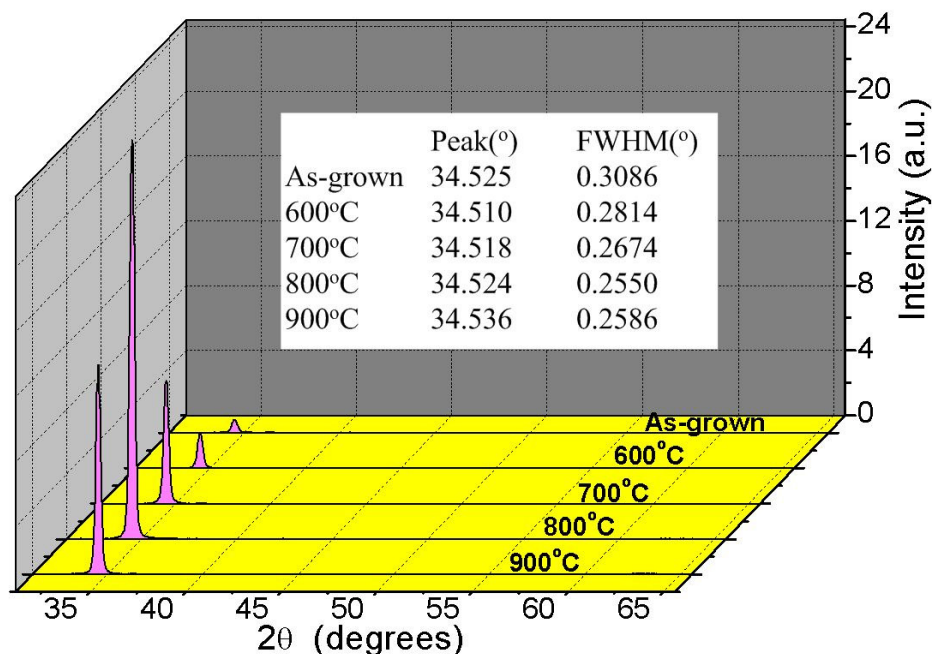


Figure 3-6 XRD profiles of the as-grown and annealed ZnO thin films. The (0002) peak position and its FWHM were recorded in the figure.

with a minor peak at $(10\bar{1}1)$, which is in good agreement with SEM measurement that the growth direction of the nanoneedles is in $[0001]$ direction. It is also noticed that the crystallinity is improved as the annealing temperature increased from 600 to 800°C. In comparison, the FWHM of (0002) peak decreases from 0.3086° for the as-grown film to 0.255° for the 800°C annealed film. It is believed that the narrowing of the FWHM is due to the improved crystallinity after annealing since the strain relaxation by annealing was found negligible in narrowing XRD peaks.¹¹⁸ Hence, the effect of strain in the coarsening process was neglected in this analysis.

The nucleation and growth process of films have been well established. It generally involves the process of nuclei formation, growth, and coalescence. At a lower growth temperature, the formation of small crystallites is kinetically favored. The formation of small crystallites reduces the supersaturation, and hence the possibility of the coalescence. During the post-growth thermal annealing, the grains gain sufficient thermal energy to initiate the coalescence. Several mass transport mechanisms have been proposed to account for the coalescence phenomenon, namely Ostwald ripening, sintering, and cluster migration.¹⁴⁸ The cartoons of the mass transport mechanisms are shown in Figure 3-7. In the Ostwald ripening mechanism, the larger particles grow or “ripen” at the expense of the smaller particles. The size of the smaller particles will shrink or even disappear due to the net atomic transport to larger particles. On the other hand, sintering is a coalescence mechanism involving particles in close proximity. A neck forms between the particles in order to reduce the total surface energy of the system. The last mechanism, cluster migration occurs as a result of collisions between separate particles as they move in random motion under excitation. Generally, the cluster migration mechanism is primarily limited to small particles with diameter of 5 to 10 nm.^{148,149} Hence, the coalescence process will be

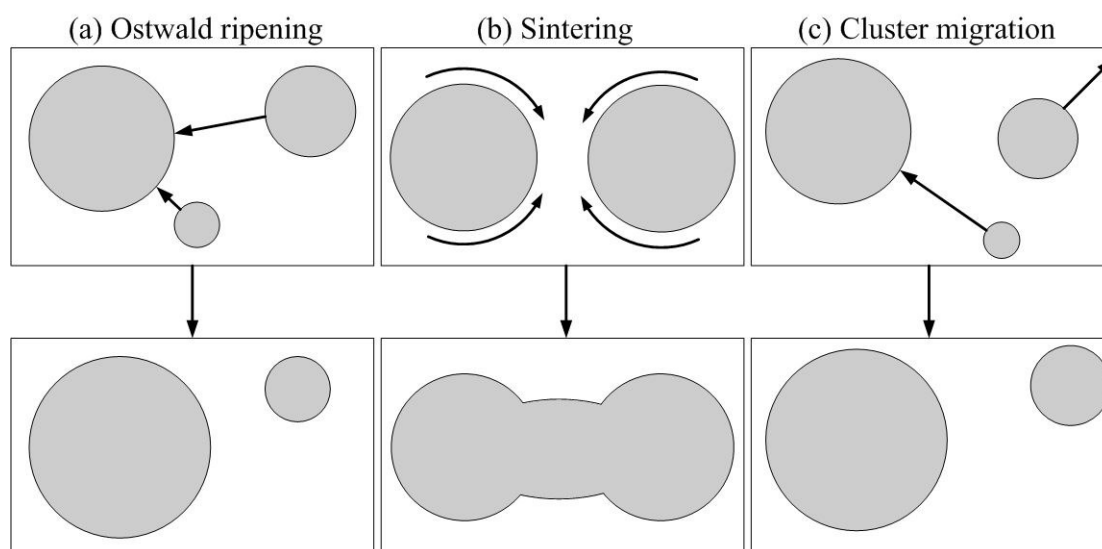


Figure 3-7 Cartoons of mass transport mechanisms of coalescence phenomenon. (a) Ostwald ripening, (b) sintering, and (c) cluster migration.

dominated by Ostwald ripening and sintering mechanism.

The grain growth is a thermally activated coarsening process. In our experiment, the temperature threshold of the coarsening process is observed to be in the range of 600 to 700°C (Figure 3-4). The Ostwald ripening is a thermal energy dependent process and hence it became significant as the temperature is increased, especially for the film annealed at 800°C. In the temperature range of 600 to 800°C, we did not observe the sintering mechanism as most of the islands appeared independently from one another [Figure 3-4 (b)-(d)]. However, as the temperature was further increased to 900°C, there are some necks connecting the islands as observed in Figure 3-4 (e). Hence, it is believed that both the Ostwald ripening and sintering mechanism occur simultaneously. These experimental results indicated that the sintering mechanism might need higher activation energy than Ostwald ripening. Also, the height of the nanoneedles reduces and the tip changed to dome shape at an annealing temperature of 900°C. It is believed that at this temperature, the evaporation rate is significant due to the fact that (1) nanosized material has a much lower melting

point than its bulk counter part;^{150,151} (2) the melting temperature of ZnO_x is generally much lower than that of the ZnO bulk (1975°C).¹⁵² As a result, during the thermal annealing, the evaporation process might happen simultaneously with the coalescence process, which complicated the analysis. This is especially obvious at the annealing temperature of 900°C, at which the evaporation process is significant, resulting in flattening of the nanoneedles. Hence, the sample annealed at 900°C will not be included and discussed in the later study of coarsening.

Grain size of the as-grown and annealed ZnO thin films was estimated from XRD, AFM, and SEM for comparison. The estimated grain sizes are summarized in Table 3-1. The grain size estimation from XRD was performed using the Scherrer's formula [Eq. (2.1)]. The grain size estimation from AFM topographs in an area of 5 $\mu\text{m} \times 5 \mu\text{m}$ was performed using the Nanoscope III software. Separation of the island clustering was performed additionally by using Line function in the software in order to minimize the estimation error. While the grain size estimation from SEM topographs was performed manually. It can be seen from Table 3-1 that the grain size estimated from different schemes increases monotonically with the annealing temperature except for the film annealed at 900°C. It should be noticed that the islands observed on the surface under the microscopes are actually the aggregation of smaller grains. Hence, larger grain size was observed in SEM and AFM compared to that determined from XRD. Nevertheless, the grain size estimated from XRD correlates well with the surface morphology observed in SEM and AFM. It shows the same trend that the grain grows larger with the increase of annealing temperature except for the one annealed at 900°C. It is also observed from Table 3-1 that the grain size estimated from AFM is close to the one estimated from SEM, except for the as-grown sample. It is worth mentioning that the grain size estimation on as-grown film

CHAPTER 3 HIGHLY C-AIXS ORIENTED ZNO THIN FILMS BY MOCVD

Table 3-1 Estimated grain size of as-grown and annealed ZnO thin films from XRD, AFM, and SEM.

Annealed temperature (°C)	Grain size (nm) in crystallographic plane (0002) from XRD	Grain size (nm) estimated from AFM topographs	Grain size (nm) estimated from SEM topographs
As-grown	29.94	59.36	29.67
600	32.84	67.52	61.53
700	34.55	94.57	98.33
800	36.24	127.96	139.08
900	35.74	104.06	119.66

from SEM is tough due to the fact that it consists of irregular shape of crystallites. Hence, the grain size estimated from AFM is more reliable to represent the mean grain size of the as-grown film by assuming circular shape of crystallites. In the later study of coarsening kinetics, grain size estimated from AFM was adopted to calculate the activation energy of coarsening.

For the ease of explanation, the size distribution of the crystallites estimated from SEM for as-grown and annealed ZnO thin films was tabulated in Figure 3-8. The value of the weighted average diameter (\bar{d}) and the density (n) of the crystallites are shown in Figure 3-8 too. It can be seen from Figure 3-8 that the size of the crystallites increases with annealing temperature from 600 to 800°C. The weighted average diameter increases from 61.53 nm for 600°C-annealed sample to 139.08 nm for 800°C-annealed sample. The density of the crystallites, on the other hands, decreases from $58.88 \times 10^6 \text{ cm}^{-2}$ for 600°C-annealed sample to $38.4 \times 10^6 \text{ cm}^{-2}$ for 800°C-annealed sample. The density distribution, associated with the size distribution, evidently shows that the Ostwald ripening and sintering occur during the thermal annealing.

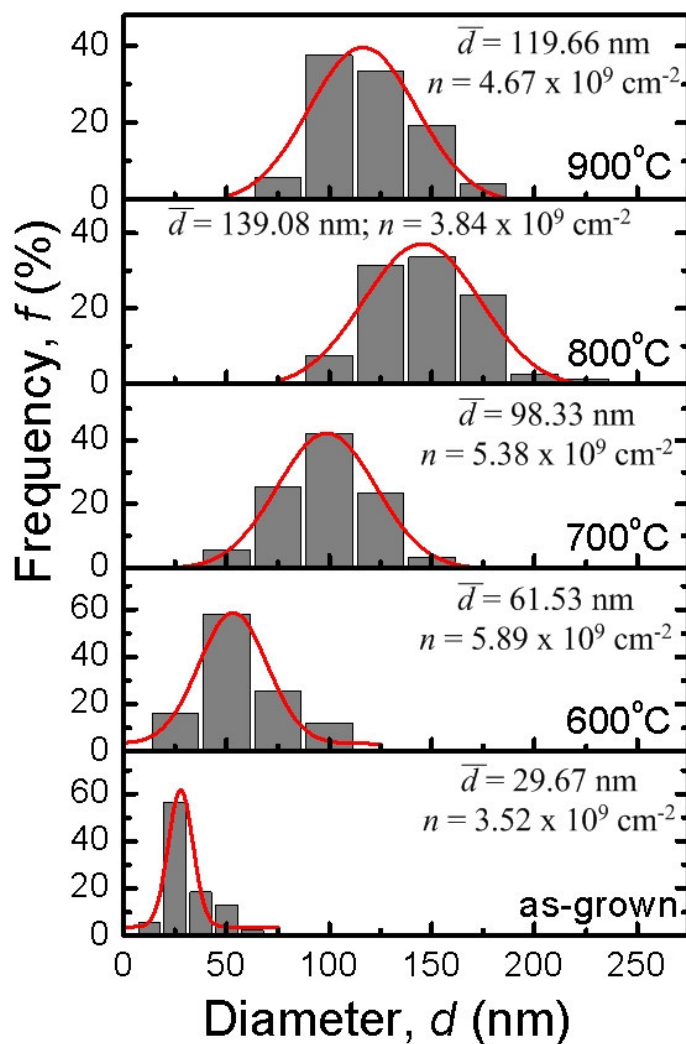


Figure 3-8 Crystallite size distribution of the as-grown and annealed ZnO thin films estimated from SEM, and fitted with a Gaussian curve. The weighted average of grain diameter (\bar{d}) and particle density (n) of the samples were shown in the figure.

The scaled particle size distribution (PSD) of the samples annealed at 600, 700, and 800°C is shown in Figure 3-9, where $g(\rho)$ is the normalized product of frequency and average crystallite diameter and ρ is the normalized diameter. It can be seen from Figure 3-9 that, the PSD narrows as the annealing temperature is increased from 600 to 800°C. Ardell suggested that the PSD broadens with the increase of volume fraction.¹⁴⁰ It is well known that the growth rate along the c-axis is the fastest for ZnO.¹⁵³ From the XRD data, the c-axis is along the film thickness direction. Through

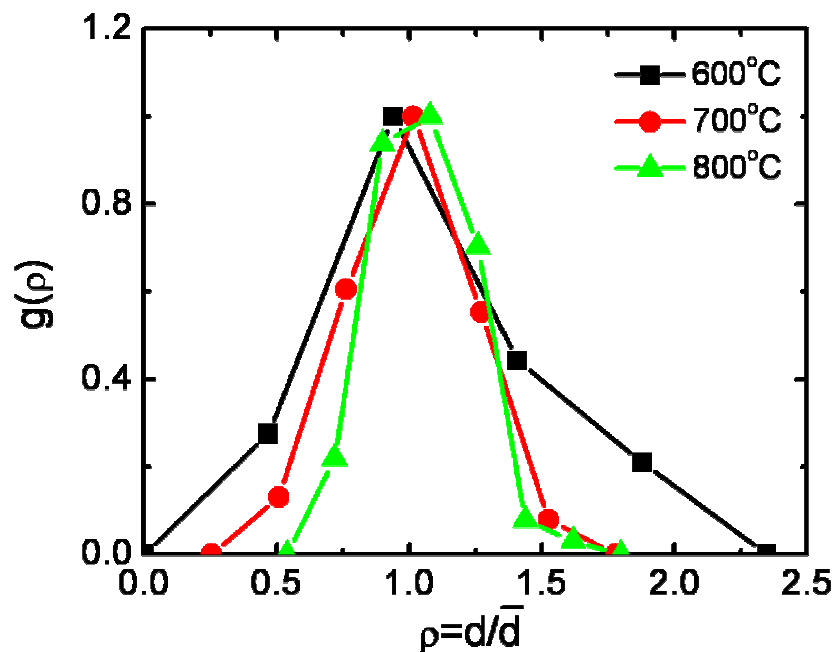


Figure 3-9 Scaled PSD of the samples annealed at 600, 700, and 800°C.

the ripening process, small crystallites diffuse to the larger crystallites, larger crystallites will then grow bigger and taller to form needle-like structures, which are along c-axis. Thus, annealing will result in a “thicker” film with a larger volume of voids (Figure 3-5), i.e. a reduction in volume fraction. Therefore, the volume fraction of the 800°C-annealed sample is definitely smaller than the one of 600°C-annealed sample, which accounts for the narrowed PSD curve with the increase of annealing temperature shown in Figure 3-9. It is worth mentioning that the data points that constructed the scaled PSD are too scarce to reveal the actual PSD. However, the self-similarity behavior of the scaled PSD agrees with the existence of Ostwald ripening during the annealing.

According to LSW theory, the coarsening kinetics of spherical crystallites can be described by:^{137,138}

$$\bar{d}_t^3 - \bar{d}_0^3 = K \frac{DC_{eq}t}{T} \quad (3.2)$$

where \bar{d}_0 and \bar{d}_t are the average crystallite diameters for the as-grown and annealed samples at specific temperature T , respectively, K is a constant, t is annealing time, D is the coefficient of particle diffusion in the matrix, and C_{eq} is the equilibrium particle composition in the matrix. In our experiment, the annealing temperature is varied while the annealing time is fixed. Hence, Eq. (3.2) can be rewritten by letting the product DC_{eq} proportional to $\exp(-E_a/k_bT)$.^{142,143}

$$T(\bar{d}_t^3 - \bar{d}_0^3) \propto e^{-(E_a/k_bT)} \quad (3.3)$$

where E_a is the activation energy for coarsening process, and k_b is the Boltzmann constant. The E_a can be obtained from the slope by plotting the logarithm of $T(\bar{d}_t^3 - \bar{d}_0^3)$ versus $1/T$, as shown in Figure 3-10. The activation energy E_a was calculated to be 1.33 eV. To our best knowledge, this is the first attempt to estimate the activation energy of Ostwald ripening in ZnO thin film. The origin of the migration species that govern the Ostwald ripening is unclear at the moment.

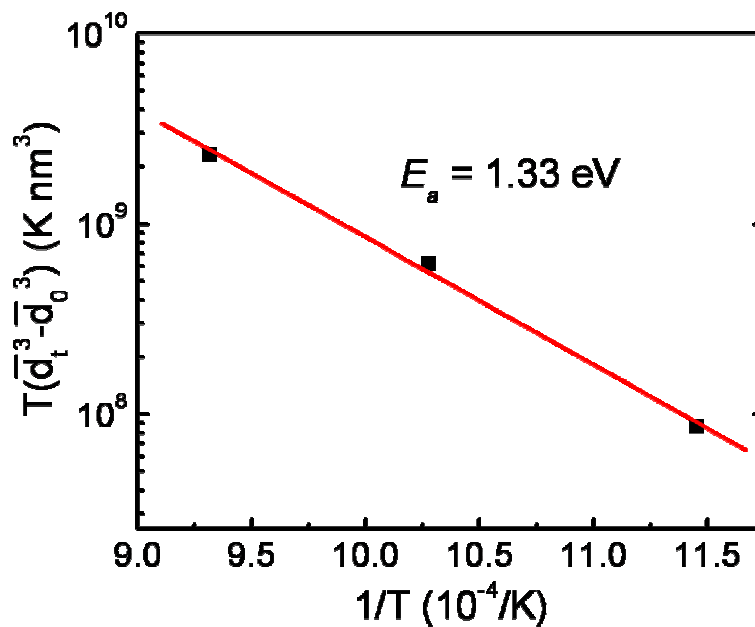


Figure 3-10 Plot of logarithm of $T(\bar{d}_t^3 - \bar{d}_0^3)$ vs $1/T$, and fitted with a line. The E_a yield from the slope is 1.33 eV.

However, the obtained activation energy of 1.33 eV is very close to the migration enthalpy of +2 charged Zn interstitial ($\text{Zn}_i^{\bullet\bullet}$), which was reported to be 1.35 eV (Ref. 154 and therein). Since the intrinsic defect of Zn_i is abundant in as-grown film (see electrical properties for detail), it is very likely that the Ostwald ripening is governed by the migration of Zn_i .

Krost *et al.*¹⁵⁵ had also reported the Ostwald ripening on ZnO thin films during the in situ annealing at 900°C in a mixed N_2 and O_2 ambient (200 mbar). The islands they obtained have a height and rms roughness of 150 and 41 nm, respectively. Also, they found that the Ostwald ripening only occurs in the very beginning of the annealing (within 2 minutes) and the origin of the conversion from 3D to 2D morphology is still unclear yet. In our study, the annealing time is fixed. Therefore, we could not observe the phenomenon reported by Krost *et al.* However, after 1 hour of annealing, fine 3D structures were observed and found dependent on annealing temperature, which suggesting the Ostwald ripening occurs during the whole annealing process up to at least 1 hour in our experiment.

Electrical properties of the as-grown and annealed ZnO thin films were measured and summarized in Table 3-2. The as-grown film exhibits *n*-type conduction behavior with electron concentration of $8.08 \times 10^{18} \text{ cm}^{-3}$, resistivity of 0.022 $\Omega\text{-cm}$ and Hall mobility of 36 $\text{cm}^2/\text{V-s}$. The conduction of the undoped ZnO is generally attributed to the intrinsic defects and/or unintentionally doped dopants. It has been calculated that the formation enthalpy for Zn interstitial (Zn_i) is low especially under Zn-rich condition, making the shallow donors abundant.¹⁵⁶ Also, most of the theoretical works show that the O vacancy (V_o) is a deep donors that it is unlikely to be the cause of the unintentional *n*-type conductivity.¹⁵⁶⁻¹⁵⁸ On the other hand, Van de Walle¹⁵⁹ has presented the theoretical evidence that hydrogen(H) acts as

CHAPTER 3 HIGHLY C-AIXS ORIENTED ZNO THIN FILMS BY MOCVD

Table 3-2 Electrical properties of the as-grown and annealed ZnO thin films.

Annealed temperature (°C)	Resistivity (Ohm-cm)	Hall mobility (cm ² /V-s)	Concentration (cm ⁻³)	Conduction type
As-grown	0.022	36	8.08×10^{18}	n
600	High	NA	NA	NA
700	22.3	0.208	1.35×10^{18}	n
800	0.469	8.55	1.56×10^{18}	n
900	0.831	8.94	8.40×10^{17}	n

a shallow donor in ZnO. While H is one of the by-products of the DEZn pyrolysis, which is inevitable in MOCVD.^{67,131} Hence, the low resistivity of the *n*-type as-grown film indicates that the film consists of shallow intrinsic defects (Zn_i) and unintentionally doped donors (H). It has been proven that the H can be driven out from the film after the post-growth annealing at temperature as low as 600°C.⁶⁶ In our experiment, we found out that the film annealed at 600°C show highly resistivity, and hence reliable Hall effect measurement could not be performed. The outdiffusion of H and Zn_i after the annealing at 600°C is believed to be the main reason to obtain high resistive ZnO thin films. However, as the annealing temperature was further increased, the resistivity decreased dramatically. The resistivity of the film annealed at 700, 800 and 900°C is 22.3, 0.469 and 0.831 Ω-cm, respectively. It is also noticed from Table 3-2 that the Hall mobility and carrier concentration decreased after the annealing. Comparing the as-grown film, the Hall mobility decreased from 36 to 0.208 cm²/V-s at an annealing temperature of 700°C. The decrease in Hall mobility might directly related to the surface morphology of the film. Both the SEM and AFM topographs show that the 3D islands were formed densely on the surface after the annealing. Hence, the well-established grain boundaries might act as scattering center and reduced the mobility of the electrons in the films. With further temperature increment to 800 and 900°C, the Hall mobility of the ZnO thin films is about 40 times higher

($8.5\sim 9\text{ cm}^2/\text{V}\cdot\text{s}$) compared to the one annealed at 700°C , indicating the crystallinity improved after annealing. Meanwhile, the carrier concentration of the films decreases from 8.08 to $1.56 \times 10^{18}\text{ cm}^{-3}$ after the annealing at 800°C . Unlike the single crystalline ZnO thin films, where the carrier concentration increases after the high-temperature annealing,¹⁶⁰ the decrease of carrier concentration in our textured films might be due to the suppression of H donors and intrinsic defects, such as Zn_i . In fact, the decrease of carrier concentration by annealing at high temperature was previously observed by Kang *et al.*¹⁶¹ and was attributed to the suppression of Zn_i .

PL measurement was carried out to observe the effect of the annealing on the optical properties. The PL of the ZnO thin films carried out at room temperature exhibits two emitting bands, namely the near-band-edge emission (NBE) and deep-level emission (DLE) as shown in Figure 3-11. The NBE in ultra violet (UV) range is attributed to the excitonic emission, due to the fact that ZnO has a large excitonic binding energy of 60 meV . The origin of the green color DLE in ZnO thin films still remains debatable. However, it is well accepted that the green color DLE is due to the

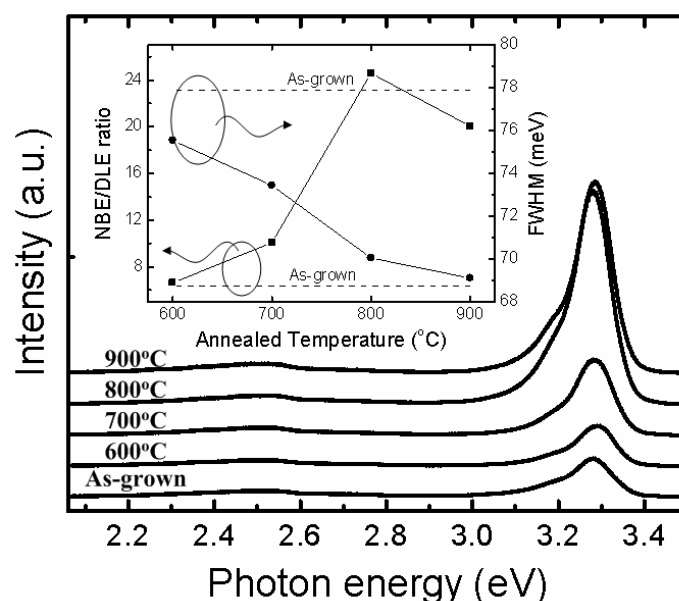


Figure 3-11 Room temperature PL spectra of as-grown and annealed ZnO thin films. Inset is the plot of NBE to DLE ratio and FWHM versus annealing temperature.

radiative recombination of a photogenerated hole with an electron in singly ionized oxygen vacancy in ZnO thin films.^{19,131,133} It can be seen from Figure 3-11 that both the NBE and DLE appears in the PL with peak positions at 3.28 and 2.5 eV, respectively. The intensity of the NBE increases with the increase of annealing temperature, while the DLE does not change much after the annealing. The FWHM of the NBE and the NBE to DLE ratio was plotted against the annealing temperature as an inset in Figure 3-11 for a better observation. The FWHM of the NBE is narrowed with the increase of annealing temperature. A 70 meV FWHM was achieved for the sample annealed at 800°C, compared to a FWHM of 75.5 meV for the as-grown sample. NBE to DLE ratio is always used to evaluate the concentration of structural defects in ZnO thin films. The NBE to DLE ratio for the as-grown sample is only 6.35 (Figure 3-11 inset). The ratio of the sample annealed at 600°C is comparable to the as-grown film, revealing the fact that the film has little improvement in crystallinity upon annealing. The film annealed at 800°C has the highest NBE to DLE ratio of 24, which can be correlated well with the structural properties of the films. The photon emission efficiency was estimated by integrating the area of the PL emission spectra. It was found that the photon emission efficiency of the 800°C-annealed film increased about four times compared to the as-grown ZnO thin film. The increase of photon emission efficiency suggests that the annealed film has less intrinsic defects, which act as non-radiative recombination centers. The enhancement of photon emission efficiency correlates well with the electrical measurement that annealed film has lower carrier concentration compared to the as-grown film.

3.3.3 Summary

In summary, post-growth thermal annealing was carried out on MOCVD grown ZnO thin films. The surface morphology changed drastically from nanosheets to nanoneedles after annealing due to the well-known Ostwald ripening in the temperature range of 600 to 800°C. The size and height of the nanoneedles are building up as the annealing temperature is increased from 600 to 800°C. As the annealing temperature was further increased to 900°C, other than Ostwald ripening, sintering mechanism was evidently observed. The activation energy for the Ostwald ripening was estimated to be 1.33 eV, which is likely to be governed by Zn atom migration. The experimental results suggest that the sintering mechanism might require higher activation energy compared to Ostwald ripening. Also, the thermal evaporation was observed and resulted in flattening of the nanoneedles. The outdiffusion of H atoms after annealing is responsible for the high resistive ZnO thin films obtained at 600°C annealing. The subsequent annealing at higher temperatures (700 to 900°C) improved the crystallinity and in turn increased the Hall mobility compared to 600°C-annealed film. PL measurement at room temperature shows that the luminescence efficiency improves with crystallinity after annealing.

CHAPTER 4 REALIZATION OF P-TYPE ZNO THIN FILMS

4.1 Background

Currently, asymmetry doping problem in ZnO is the main obstacle that hindered the realization of ZnO-based current injection LEDs and LDs. Therefore, a lot of efforts have been devoted to the doping engineering of ZnO in order to realize ZnO-based opto-electronic devices.

In general, there are three main factors that could limit the dopability in a material. (i) The dopants have a low solubility in the bulk material. (ii) The dopants have good solubility but it forms deep acceptor or donor level, which are not readily ionized at the desired operating temperature. (iii) The dopants have good solubility and are readily ionized, but the self-compensation effect limits the material to be *n*-type or *p*-type.¹⁶²

For ZnO material, the possible *p*-type dopants includes of group-I elements lithium (Li), sodium (Na), and potassium (K) and group-V elements nitrogen (N), phosphorus (P), arsenic (As), and antimony (Sb). Kobayashi *et al.*¹⁶³ revealed that among the group-V elements, N is the best candidate of *p*-type dopants in ZnO. Recently, Park *et al.*⁶¹ extended the first principle calculation to the group-I elements. In their finding, group-I elements, Li, Na, and K that substitute on the Zn site are predicted to have acceptor energy levels of 0.09, 0.17, and 0.32 eV, respectively. While the group-V elements, N, P, and As that substitute on the O site have acceptor energy levels of 0.40, 0.93, and 1.15 eV, respectively. From their calculation, group-I elements are predicted to be better dopants than group-V elements in terms of the shallowness of the acceptor levels. However, group-I elements have low doping

efficiency which is limited by the formation of compensating interstitials. So the best *p*-type dopant for ZnO was concluded to be N since N has the smallest ionization energy among the group-V dopants.

4.1.1 Dopant choice I: Group-I elements (Li, Na, K)

Li and Na doping in ZnO thin films was known to lead to semi-insulating (SI) behaviour.^{164,165} While for K doping, the formation of V_O donors will hinder the formation of *p*-type ZnO thin films.⁶¹ However, Lee and Chang revealed that the solubility of group-I elements for Li and Na could be greatly enhanced by hydrogenation and a subsequent annealing process, which will lead to the activation of passivated acceptors.¹⁶⁶ On the other hand, Wardle *et al.*¹⁶⁷ further investigated the dopant Li in ZnO thin films and concluded that $Li_{Zn}-Li_i$ is formed more readily than any isolated defects. Hence, the self-compensation between Li impurities would be the limiting factor to obtain Li-doped *p*-type ZnO thin films. The theoretical prediction suggested that group-I dopants are not the ideal choice for *p*-type dopants in ZnO thin films. Nevertheless, *p*-type Li-doped ZnO thin films have been experimentally demonstrated by using sputtering and PLD recently.^{205,206,217}

4.1.2 Dopant choice II: Group-V elements (N, P, As, Sb)

From theoretical point of view, N seems to be the best dopant for ZnO materials.^{61,163} However, the difficulty in realizing *p*-type ZnO:N films experimentally has always amazed and humbled the researchers. The low doping efficiency of N acceptors was addressed theoretically and attributed to the compensation effect by N_2 complexes, which behaves as a double donor.¹⁶⁸ Nevertheless, a great deal of effort has been devoted to the development of *p*-type ZnO thin films especially on ZnO:N.

The first *p*-type ZnO:N was reported by Minegishi *et al.*¹⁶⁹ in year 1997. Subsequently, most of the attempts to produce *p*-type ZnO have employed N as the acceptor (see Table 4-1, page 100). In year 1999, Yamamoto *et al.*¹⁷⁰⁻¹⁷² investigated the electronic structures of *n*- or *p*-type doped ZnO based on *ab initio* electronic band structure calculations. They proposed a codoping method, in which the acceptor (N) and donor (Ga, Al, In) are simultaneously doped into ZnO thin films in order to increase the solubility of N. Several codoping methods have been reported to prepare the *p*-type ZnO thin films by different donors, such as Ga, Al, and In as seen in Table 4-1.

Due to large difference in ionic size between P and O, theoretical calculation predicted that P_O should have a deeper acceptor level at 0.93 eV, as compared to 0.40 eV for N_O.⁶¹ Nevertheless, Aoki *et al.*⁶⁸ have fabricated a homojunction ZnO diode with light emission (370 – 380 nm and 400 – 500 nm) at 110 K using laser doping of P from Zn₃P₂. Recently, Kim *et al.*¹⁷³ have used P₂O₅ to fabricate ZnO:P films and produced *p*-type ZnO:P films by thermal annealing. However, the microscopic structure of dominant acceptors in P-doped ZnO is not yet established. Moreover, the difference in doping efficiency between two dopant sources, P₂O₅ and Zn₃P₂, is not clearly understood.²⁰⁹

For As doping, Ryu *et al.*¹⁷⁴ have successfully demonstrated *p*-type As-doped ZnO layers on Al₂O₃ substrates with an activation energy of about 120 meV. More recently, Look *et al.*¹⁷⁵ prepared *p*-type As-doped ZnO thin films by evaporating Zn₃As₂ and subsequent sputtering of ZnO. Theoretical investigation has suggested that an As_{Zn}-2V_{Zn} complex, in which the As atom occupying a Zn site gives a shallow acceptor level by forming a complex with two Zn vacancies, would be the origin of *p*-type conduction.¹⁷⁶ Wahl *et al.*¹⁷⁷ have also revealed that As does not occupy

substitutional O sites but in its large majority substitutional Zn sites. However, Vaithianathan *et al.*¹⁷⁸ have shown that As substitutionally replaces O in the ZnO lattice, i.e. As_O to contribute *p*-type conductivity, by using x-ray absorption near-edge structure (XANES) spectroscopy. All these interesting but contradicting results must be subject to further experimental verification.

In addition to N, P, and As, another group-V element Sb has been investigated as a *p*-type dopant in ZnO materials. Xiu *et al.*¹⁷⁹ have demonstrated high-mobility Sb-doped *p*-type ZnO thin films by MBE. The *p*-type ZnO:Sb films have mobility as high as 20 cm²/V-s, with hole concentration of 1.7×10^{18} cm⁻³. More recently, Kang *et al.*²¹² have also investigated on *p*-type ZnO thin films by employing Ag as acceptor. They revealed that the acceptors were formed by substitution of Ag for Zn and the ZnO:Ag films have hole concentration of $4.9 \times 10^{16} - 6.0 \times 10^{17}$ cm⁻³. These interesting finding on the new dopant sources might provide a new clue in *p*-type ZnO thin films investigation.

4.1.3 Self-compensation process in ZnO

After the discussion on the dopant choice and their solubility in ZnO, another important issue that limits the *p*-type doping in ZnO is self-compensation process. The donor-like native defects, such as zinc interstitial (Zn_i) and oxygen vacancy (V_o), are dominant in ZnO, resulting in *n*-type behavior. In order to achieve *p*-type conduction in ZnO, these donor-like native defects have to be suppressed or even eliminated. According to Zhang *et al.*⁵⁹ and Lee *et al.*,¹⁸⁰ the donor-like defects can be suppressed at the oxygen rich (O-rich) condition and hence it is possible to obtain intrinsic *p*-type conduction in ZnO. However, as seen from Figure 4-1, under the O-rich condition, the concentration of acceptor-like defects, such as zinc vacancy

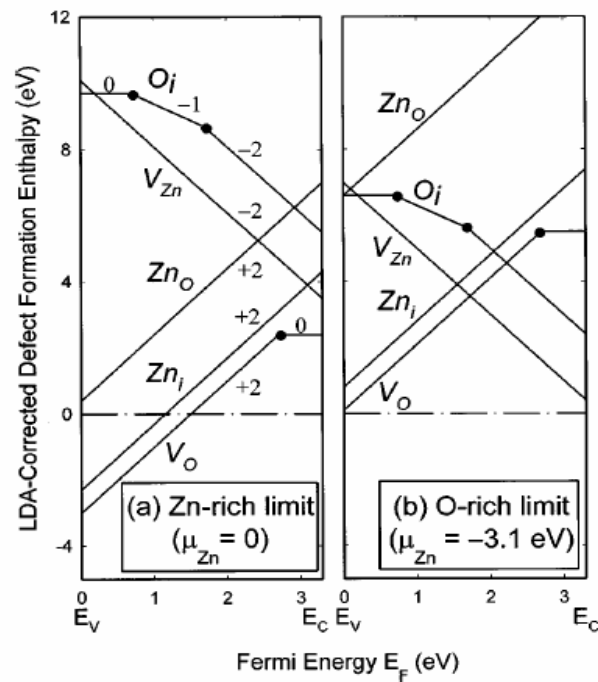


Figure 4-1 LDA defect formation enthalpies are shown in lines as a function of the Fermi energy E_F at the zinc-rich ($\mu_{Zn}=0$) and oxygen-rich ($\mu_{Zn}=-3.1$ eV) limits, respectively. The charge states of the defects are shown as -2 , -1 , 0 , and $+2$. Defect transition energies are shown as solid dots.⁵⁹

(V_{Zn}) and oxygen interstitial (O_i) remain low due to their high formation enthalpy. Nevertheless, *p*-type ZnO thin films can be realized even without doping by suppressing the donor-like defects, but the reproducibility is the main issue at the present research.^{181-184,215} Ma *et al.*¹⁸⁴ reported recently that they obtained intrinsic *p*-type ZnO thin films by tuning the oxygen partial pressure in the MOVPE. The best *p*-type sample they have obtained has a carrier concentration of $1.59 \times 10^{16} \text{ cm}^{-3}$ and carrier mobility of $3.74 \text{ cm}^2/\text{V}\cdot\text{s}$. However, the film has relatively large resistivity with $42.7 \text{ }\Omega\cdot\text{cm}$. Xiong *et al.*¹⁸³ reported intrinsic *p*-type ZnO thin films by adjusting the oxygen content in the reactive sputtering. These works have demonstrated that the intrinsic *p*-type ZnO thin films can be realized by optimizing the growth condition, such as growth method, growth temperature, precursors flow rate control.

CHAPTER 4 REALIZATION OF P-TYPE ZNO THIN FILMS

Although there have been many reports of *p*-type doping in ZnO thin films using various growth methods and various dopant elements, as shown in Table 4-1, reliable and reproducible high quality *p*-type conductivity has not yet been achieved for ZnO. This strongly suggests that the physics underlying ZnO doping engineering is subtle and poorly understood. It is hence worthwhile to carry out a detailed study on defect engineering in ZnO. In this chapter, nominal undoped, N-doped, and unintentional carbon-doped *p*-type ZnO thin films are investigated.

Table 4-1 Survey of *p*-type ZnO.

Year	Researchers	Methods	Dopants	Hall mobility (cm ² /V-s)	Hole Concentration (cm ⁻³)
1997	Minegishi <i>et al.</i> ¹⁸⁵	CVD	N	12	1.5×10^{16}
1999	Joseph <i>et al.</i> ¹⁸⁶	PLD	Ga, N	0.05-0.07	$2-4 \times 10^{19}$
2000	Aoki <i>et al.</i> ⁶⁸	CVD	P	NA	NA
2000	Guo <i>et al.</i> ¹⁸⁷	PLD	N	0.1-0.4	$3-6 \times 10^{18}$
2000	Ryu <i>et al.</i> ¹⁸⁸	Pulsed laser ablation	As	0.1-50	$1 \times 10^{18}-1 \times 10^{21}$
2002	Look <i>et al.</i> ¹⁶⁵	MBE	N	2	9×10^{16}
2002	Li <i>et al.</i> ¹⁸⁹	Thermal oxidation	N	0.098	4.16×10^{17}
2003	Singh <i>et al.</i> ¹⁹⁰	RF sputtering	Ga, N	NA	9×10^{16}
2003	Lu <i>et al.</i> ¹⁹¹	Solid source CVD	N	0.97	9.8×10^{17}
2003	Kim <i>et al.</i> ¹⁷³	RF sputtering	P	3.51	1.7×10^{19}
2003	Lu <i>et al.</i> ¹⁹²	DC reactive magnetron sputtering	N	1.3-2.4	$4 \times 10^{15}-7 \times 10^{17}$
2003	Ryu <i>et al.</i> ¹⁷⁴	Hybrid beam deposition	As	35	4×10^{17}
2003	Li <i>et al.</i> ¹⁹³	MOCVD	N	0.34	1.06×10^{18}
2004	Xu <i>et al.</i> ¹⁹⁴	MOCVD	N	0.203	1.73×10^{17}
2004	Ye <i>et al.</i> ¹⁹⁵	DC reactive magnetron sputtering	Al, N	0.3	1.1×10^{17}
2004	Zhang <i>et al.</i> ¹⁹⁶	Ultrasonic spray pyrolysis	Al, N	73.6	5.09×10^{18}
2004	Bian <i>et al.</i> ¹⁹⁷	Ultrasonic spray pyrolysis	In, N	155	2.44×10^{18}
2005	Tsukazaki <i>et al.</i> ⁷⁷	Laser MBE	N	NA	$1 \times 10^{16}-1 \times 10^{17}$
2005	So <i>et al.</i> ¹⁹⁸	Diffusion	As, P	19.04	6.94×10^{19}
2005	Vaithianathan <i>et al.</i> ¹⁹⁹	PLD	P	2.38-39.3	$5.1 \times 10^{14}-1.5 \times 10^{17}$
2005	Xiu <i>et al.</i> ²⁰⁰	MBE	Sb	20	1×10^{18}
2005	Braunstein <i>et al.</i> ²⁰¹	Ion implantation	As	6.9	2.5×10^{13}
2005	Du <i>et al.</i> ²⁰²	MOVPE	N	3-17	$5.5 \times 10^{15}-8.3 \times 10^{17}$

(continue in next page)

CHAPTER 4 REALIZATION OF P-TYPE ZNO THIN FILMS

(continue)

Year	Researchers	Methods	Dopants	Hall mobility (cm ² /V-s)	Hole Concentration (cm ⁻³)
2005	Chen <i>et al.</i> ²⁰³	MOCVD	P	0.189-0.838	2×10^{17} - 1.6×10^{18}
2005	Hwang <i>et al.</i> ²⁰⁴	RF magnetron sputtering	P	0.53-3.51	1×10^{17} - 1.7×10^{19}
2005	Zeng <i>et al.</i> ²⁰⁵	DC reactive magnetron sputtering	Li	3.47	1×10^{17}
2006	Zeng <i>et al.</i> ²⁰⁶	PLD	Li	2.65	1.44×10^{17}
2006	Wang <i>et al.</i> ²⁰⁷	DC reactive magnetron sputtering	N	0.0768	7.47×10^{18}
2006	Jiao <i>et al.</i> ²⁰⁸	Plasma-assisted MBE	N	1.5	1.3×10^{17}
2006	Yu <i>et al.</i> ²⁰⁹	RF sputtering	P	1	3.84×10^{19}
2006	Wang <i>et al.</i> ²¹⁰	RF magnetron sputtering	P	4 – 13	2.7×10^{16} - 2.2×10^{17}
2006	Nakano <i>et al.</i> ²¹¹	Sputter + annealing	N	3 – 5	1×10^{17}
2006	Kang <i>et al.</i> ²¹²	PLD	Ag	0.29-2.32	4.9×10^{16} - 6.0×10^{17}
2006	Lu <i>et al.</i> ²¹³	PLD	Li, N	0.75	8.92×10^{18}
2006	Cao <i>et al.</i> ²¹⁴	Sol-gel spin coating	N, In	0.6	9.81×10^{17}
2006	Zeng <i>et al.</i> ²¹⁵	MOCVD	NA	2.6	1.88×10^{17}
2006	Hu <i>et al.</i> ²¹⁶	RF sputtering	P	0.341	2.8×10^{17}
2006	Lu <i>et al.</i> ²¹⁷	PLD	Li	1.75	6.04×10^{17}
2006	Kumar <i>et al.</i> ²¹⁸	RF magnetron sputtering	Ga, N	< 1	3.9×10^{17}

4.2 P-type Nominal Undoped and N-doped Polycrystalline

ZnO Thin Films

4.2.1 Experiment

The ZnO thin films were grown on Al₂O₃ (0001) by MOCVD with original reactor as described in chapter 2 and 3. The deposition temperature was controlled at 350°C as the films grown at this temperature yield good structural, optical, and electrical properties.¹¹⁸ Dimethylzinc (DMZn) and ultrahigh-purity O₂ (99.9999%) were used as the zinc source and oxidizer, respectively. Nitrogen (N₂) gas was used as the carrier gas for the DMZn bubbler and the nitrous oxide (N₂O) was used for nitrogen doping. The flow rates of the DMZn and O₂ were varied such that the Zn:O ratio was maintained within 0 to 0.8 (O-rich condition). For N doping experiment, 5 sccm of N₂O gas was mixed with oxygen and then injected into the reaction chamber. The deposition time was 10 minutes and the growth rate was about 30 nm/min. The chamber pressure was maintained at about 30 mbar.

Electrical resistivity, carrier density and mobility were measured with a magnetic field of 0.32 T by van der Pauw method at room temperature. Indium contacts were heat treated at ~300°C for a few minutes for establishing reliable ohmic contact to ZnO thin films. Secondary ion mass spectrometry (SIMS) was carried out with a secondary ion mass spectrometer (TOF SIMS IV). The crystal structure of obtained films was characterized by X-ray diffraction (XRD) measurement with CuK α radiation (Siemens D5005 X-Ray Diffractometer). The optical transmission spectra were examined with a spectrophotometer (UV-2501PC). The photoluminescence (PL) spectrum was measured with a micro PL system at room temperature and excited by the 325 nm line of a He-Cd laser.

4.2.2 Results and Discussion

Figure 4-2 shows the summary of the electrical properties of ZnO thin films examined by Hall measurement at room temperature. One of the samples (with filled symbols) was grown with 5 sccm of N₂O gas with the intention of N doping. It can be seen clearly that the realization of intrinsic *p*-type ZnO thin film depends strongly on the Zn to O ratio. A change of conduction type from *n* to *p* occurs at Zn:O ratio of 0.2. As the Zn:O ratio was controlled smaller than 0.2, the *p*-type ZnO thin films can be realized. The intrinsic *p*-type ZnO thin films were also realized by several research groups by tuning the Zn:O ratio during the growth.¹⁸¹⁻¹⁸⁴ From Figure 4-2, it can be seen that the best intrinsic *p*-type ZnO thin films has low resistivity of 0.369 Ω-cm, high carrier concentration of $1.62 \times 10^{19} \text{ cm}^{-3}$ and relatively low Hall mobility of 3.14 cm²/V-s. While the *p*-type sample grown with the N₂O has carrier concentration of $1.41 \times 10^{18} \text{ cm}^{-3}$, Hall mobility of 0.264 cm²/V-s and resistivity of 16.8 Ω-cm. At the O-rich condition, acceptor-like defects, such as V_{Zn}, O_i and O_{Zn}, have lower formation enthalpies compared to those at the Zn-rich condition. The excess oxygen results in a

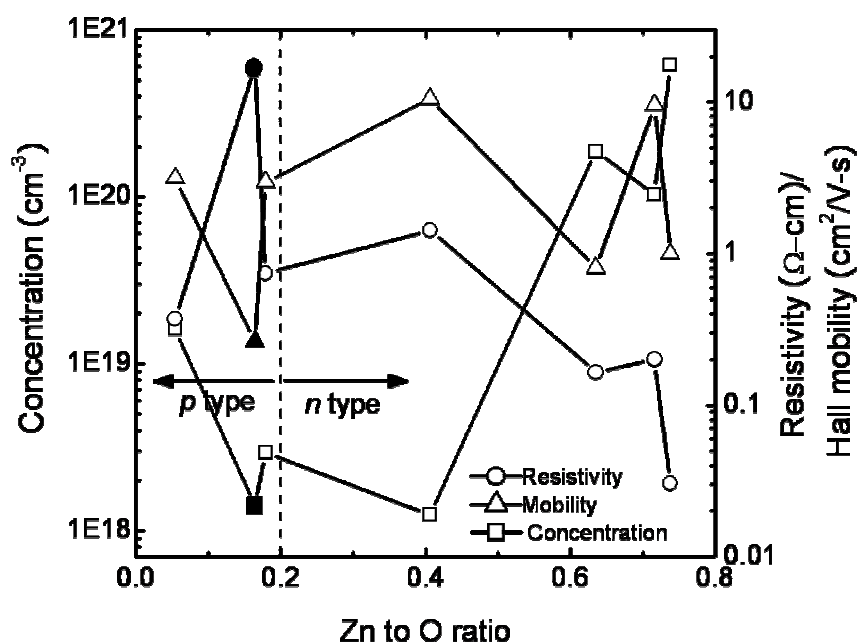
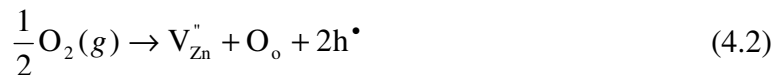
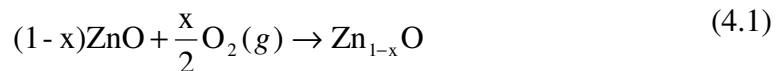


Figure 4-2 Carrier concentration, Hall mobility, and resistivity of ZnO thin films as a function of Zn:O molar ratio. Filled symbol sample was grown with 5 sccm of N₂O.

non-stoichiometric compound Zn_{1-x}O ($0 < x < 1$), which can be explained in the following chemical reactions by using Kröger-Vink notation for lattice defects:



where V_{Zn}'' is the negative charge on zinc vacancy and O_{O} is the oxygen on regular lattice site. The zinc vacancy can subsequently be ionized to “give away” holes as Eq. (4.3) and Eq. (4.4):



As a result, holes present in the V_{Zn}' and V_{Zn} can be excited and transferred to other part of crystal, which makes the ZnO *p*-type conduction intrinsically, for sample grown without N_2O .

Figure 4-3 (a) and (b) show respectively, the SIMS profiles of *p*-type ZnO thin films obtained with and without supplying N_2O gas into the chamber during growth. Secondary ions intensities of Ga and N atoms were detected using $^{71}\text{Ga}^+$ and $^{14}\text{N}^-$, respectively. Ga detection was carried out during the SIMS analysis in order to confirm the ZnO thin films are free of Ga contamination that remained in the chamber due to previous experiments with Ga doping. The N impurities were detected by using Cs sputtering gun with negative secondary ion polarity. For the sample shown in Figure 4-3 (a), though 5 sccm of N_2O gas was introduced into the chamber during the growth, the nitrogen intensity was well below the SIMS sensitivity limit (N count was too low to be detected). H. Matsui *et al.*²¹⁹ have previously shown that the solubility

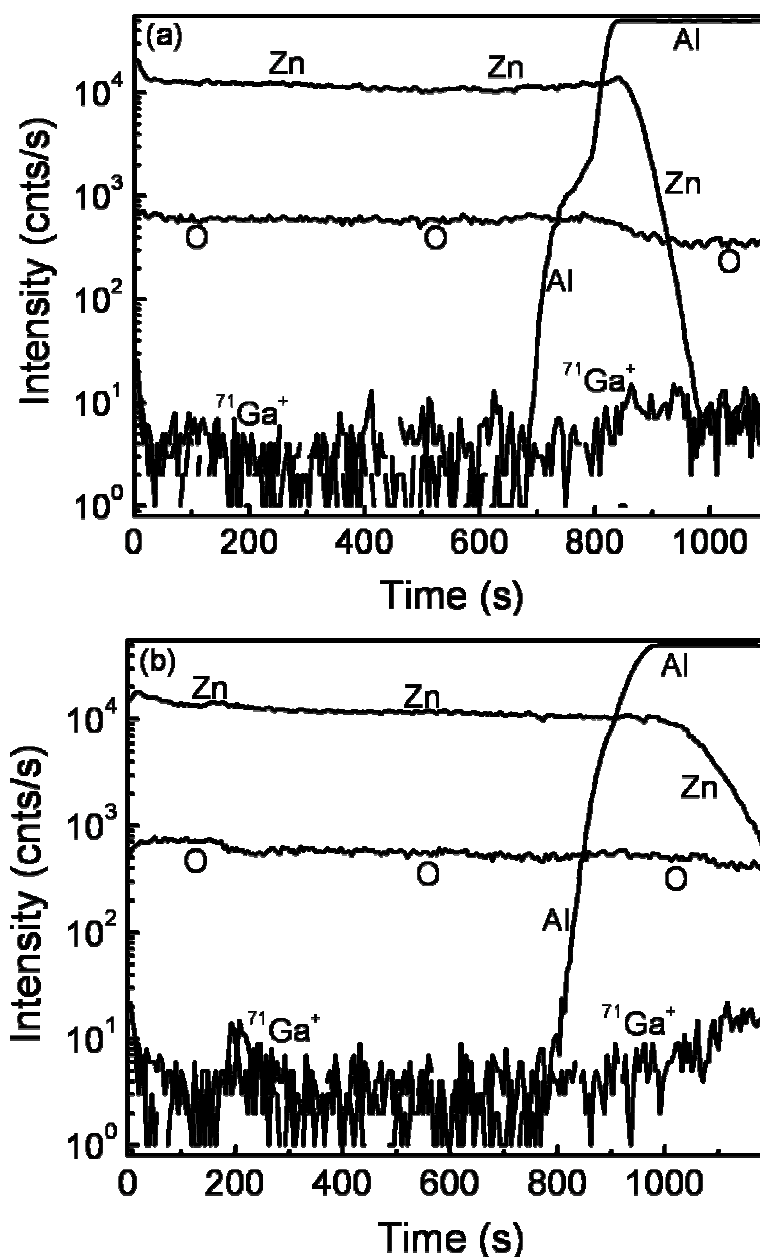


Figure 4-3 SIMS profile of the *p*-type ZnO thin films deposited on sapphire at 350°C (a) with N_2O and (b) without N_2O .

of nitrogen is low due to the poor dissociation process of N_2O at low growth temperature of 350°C. Thus, the N concentration in the ZnO thin film grown with N_2O flow should be quite low. However, the film grown with N_2O flow was yellowish in color by visual inspection, while the sample grown without N_2O flow appeared colorless. The yellowish appearance of N-doped ZnO thin film was also

reported by Nakahara *et al.*²²⁰ So, it is likely that a small amount of N was doped into the ZnO thin film grown with N_2O flow. Thus, we postulate that the *p*-type behavior of the sample grown with N_2O should be due to the N occupying O sites (N_O) as acceptors from N_2O doping, and/or the intrinsic acceptor-like defects V_{Zn} . From Figure 4-3 (b), it can be seen that the secondary ions intensities of Ga and N in undoped ZnO thin film are well below the SIMS sensitivity limit. This shows that the obtained *p*-type ZnO thin film is free of contaminants or dopants, such as Ga and N, as expected. As a result, the *p*-type behavior of the undoped ZnO sample indicates the successfully suppression of donor-like defects and formation of intrinsic *p*-type ZnO thin films.

Figure 4-4 (a) and (b) show the XRD profiles of the ZnO thin films grown on sapphire at 350°C with and without supplying N_2O gas into chamber, respectively. It can be seen that the ZnO thin films exhibit polycrystalline structure with preferential orientation along c-axis. With the introduction of N_2O gas into the chamber, the crystallinity of the film is slightly poorer. The polycrystalline structure in the obtained

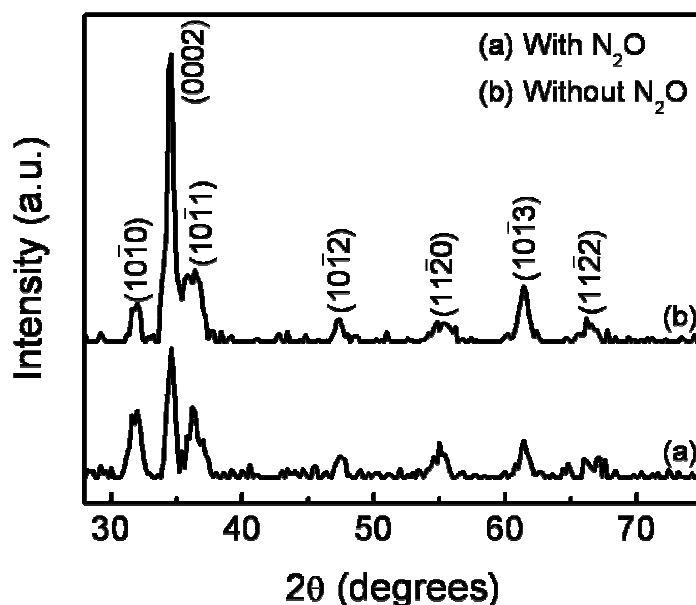


Figure 4-4 X-ray diffraction profiles of ZnO thin films grown on sapphire at 350°C (a) with N_2O and (b) without N_2O .

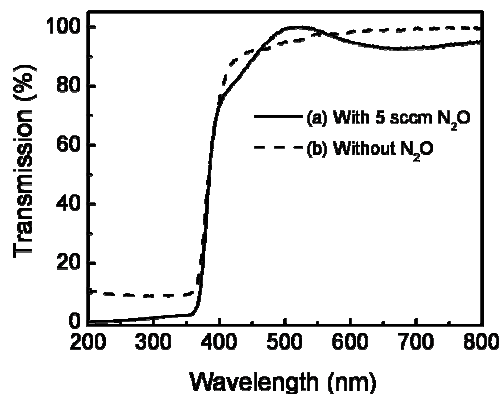


Figure 4-5 Transmittance spectra for the *p*-type ZnO thin films obtained (a) with N₂O and (b) without N₂O.

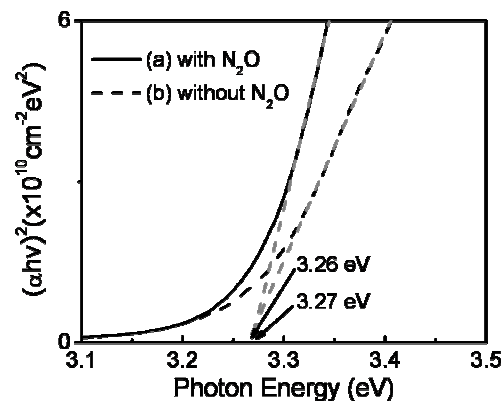


Figure 4-6 Plot of $(\alpha h\nu)^2$ versus photon energy for the ZnO thin films obtained (a) with N₂O and (b) without N₂O.

ZnO thin films is the main reason for the low Hall mobility as stated in the previous discussion.

Figure 4-5 (a) and (b) show the typical transmission spectra for the *p*-type ZnO thin films obtained with and without supplying N₂O gas, respectively. It can be seen that both the obtained films possess high transmittance close to 100% in the visible region and have sharp absorption edge. Figure 4-6 shows the relationship between the absorption coefficient and photon energy for the *p*-type ZnO thin films. The optical bandgap was determined to be 3.26 eV and 3.27 eV for the *p*-type ZnO thin films obtained with and without supplying N₂O gas, respectively by using Eq. (2.3) and Eq. (2.4).

Figure 4-7 shows the normalized room temperature PL spectra of two *p*-type ZnO thin films grown with and without N₂O flow. The fringes, which are more prominent for the sample grown without N₂O flow, are due to the interference effect from the coating of CCD detector. Comparing the samples grown with and without N₂O flow in Figure 4-7, an obvious shift in the near-band-edge emission (NBE) peak is observed. The peak of N-doped sample is at 3.330 eV, which can be attributed to

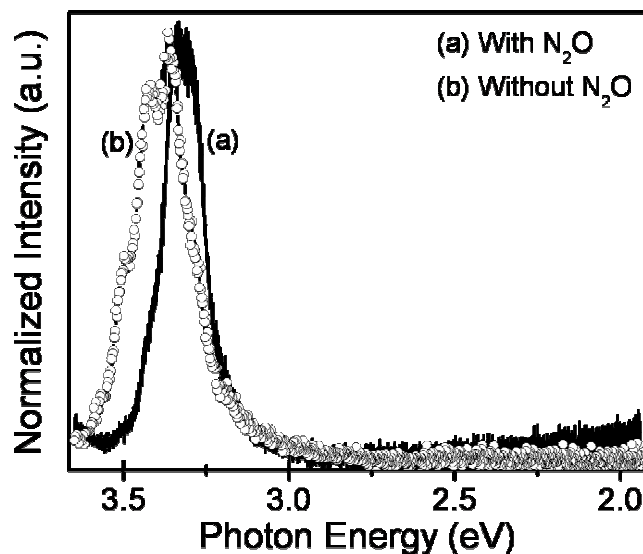


Figure 4-7 Normalized room temperature PL spectra of obtained *p*-type ZnO thin films (a) with N₂O and (b) without N₂O.

the neutral acceptor-bound exciton (A^0X) associated with N_O . While the undoped sample is peaking at 3.388 eV, which is due to the A^0X associated with V_{Zn} . The A^0X red-shifted 58 meV for N-doped sample compared to the undoped one, which indicates the N_O acceptors have higher ionization energy than V_{Zn} . Similar red-shift of emission peak at room temperature for N-doped ZnO thin film was also observed by Wang *et al.*²²¹ It is worth mentioning that the difference in PL spectra for the *p*-type ZnO thin films grown with and without N₂O flow is also an evidence that the *p*-type N-doped ZnO thin films were achieved with N₂O flow, apart from the difference in visual appearance of the two types of samples.

The origin of the green color deep-level emission (DLE) in ZnO thin films still remains debatable. Many researchers attributed the DLE in ZnO thin films to the intrinsic defects of V_o .^{19,161,184} As is seen from Figure 4-7, there is no DLE observed for both *p*-type samples. We suspect that the V_o was suppressed in the films grown at O-rich condition,¹⁸⁴ and/or passivated by hydrogen,^{222,223} which is one of the by-products of DMZn pyrolysis process. So, the undetected DLE in the *p*-type samples is

mainly due to the suppression of V_o , which has a higher formation energy at O-rich condition.^{59,168}

4.2.3 Summary

In summary, low resistivity *p*-type ZnO thin films were obtained by MOCVD with and without N₂O flow in fabrication. From SIMS measurement, the *p*-type conduction of ZnO thin films fabricated without N₂O flow is intrinsic, and mainly contributed by intrinsic acceptor-like defects, V_{Zn} . For the sample fabricated with N₂O flow, the *p*-type conductivity is primarily due to the impurities (N_O acceptors) formed by N-doping. The intrinsic *p*-type ZnO thin films can be obtained by adjusting the Zn:O ratio from 0.05 to 0.2. The best *p*-type ZnO thin films possess low resistivity of 0.369 Ω -cm and high hole concentration of $1.62 \times 10^{19} \text{ cm}^{-3}$, which is suitable for short-wavelength optoelectronic devices. This work demonstrates that *p*-type ZnO can be realized by MOCVD without doping, which proves the theoretical prediction of intrinsic *p*-type conduction and provides a guide for future works.

4.3 **Revealing p-type in Carbon-doped ZnO Thin Films**

As described previously, prominent achievements have been made recently on ZnO especially on the demonstration of ZnO homojunction LEDs,^{78,86-89} where either MBE or MOCVD was applied. Comparing to MBE, MOCVD is possibly the tool of choice for ZnO-based devices, as MOCVD enjoys lower cost, easy scaling up, and most importantly, the successful story in producing GaN-based LEDs and LDs. Nevertheless, unintentional hydrogen and carbon doping in MOCVD grown ZnO is unavoidable, as the metal organics contain organic compounds. Li *et al.*^{67,224} has reported the passivation effect of hydrogen and compensation effect of carbon in nitrogen-doped ZnO thin films grown by MOCVD. Other than which, reports on the role of unintentionally doped carbon in ZnO by MOCVD are rare. In this section, the *p*-type conductivity of ZnO thin films revealed by post-growth thermal annealing is presented and the role of carbon in immobilizing oxygen interstitials in ZnO is discussed.

4.3.1 **Experiment**

The 350 nm thick ZnO thin film was deposited on sapphire [Al₂O₃(0001)] substrates by MOCVD. Previously, highly c-axis oriented ZnO thin films were found to be zinc-rich and the subsequent annealing at high temperature leads to the formation of nanoneedles.²²⁵ In this experiment, the flow rate of DEZn was reduced from 6 to 3 sccm. The as-grown sample was cut into pieces and one of them was used as a reference of the as-grown sample. The rest of the samples were annealed in air, O₂, and N₂ ambient, respectively. The post-growth thermal annealing was performed at 800°C and at atmospheric pressure for 1 hour. The samples were loaded into the heated chamber and pulled out immediately after the annealing. The rms roughness of

the as-grown and annealed ZnO thin films was found to be in the range of 5 to 6 nm by AFM.

The crystal structure was characterized by x-ray diffraction (XRD) using Siemens D5005 x-ray diffractometer with Cu K α radiation. Electrical resistivity, carrier concentration and mobility were measured with a magnetic field of 0.32 T by a four-point probe van der Pauw method at room temperature. Indium contacts were heat treated at $\sim 100^{\circ}\text{C}$ for a few minutes for establishing reliable ohmic contact to ZnO thin films. Secondary ion mass spectrometry (SIMS) measurement was carried out using secondary ion mass spectrometer (TOF SIMS IV). The x-ray photoelectron (XPS) measurement was performed using ESCALAB 220i-XL with Al K α radiation of 1486.6 eV. The binding energy was referenced to the C 1s line at binding energy of 285.0 eV.

4.3.2 Results and Discussion

The electrical property of the as-grown and annealed ZnO thin films is tabulated in Table 4-2. All the Hall measurements were carried out with reliable ohmic contact to ZnO thin films and the typical I-V curve was shown in Figure 4-8. It is noticed that the as-grown ZnO thin film is conductive (resistivity of $0.01\ \Omega\text{-cm}$) with the majority carrier of electron (concentration of $5.7 \times 10^{18}\ \text{cm}^{-3}$). The electron conduction in the nominal undoped ZnO thin films could be due to hydrogen (H) and/or intrinsic defects, which is generally attributed to zinc interstitial (Zn_i). After annealing, the resistivity of the annealed films increases by at least two orders in magnitude. The increase of resistivity could be understood by (1) outdiffusion of H (Ref. 66) and (2) suppression and/or passivation and/or compensation of the Zn_i after annealing. Due to the highly-resistive characteristic of the air-annealed and O_2 -annealed samples, the conductivity type of the films could not be confirmed by Hall

CHAPTER 4 REALIZATION OF P-TYPE ZNO THIN FILMS

Table 4-2 Electrical property of ZnO thin films characterized by Hall effect measurement.

Annealed ambient	Resistivity ($\Omega\text{-cm}$)	Hall mobility ($\text{cm}^2/\text{V-s}$)	Carrier concentration (cm^{-3})	Conduction type
As grown	0.01	57.8	5.70×10^{18}	<i>n</i>
O ₂	68.2	5.18	8.70×10^{15}	<i>n</i>
Air	158.4	17.1	1.31×10^{15}	<i>p</i>
N ₂	2.18	20.7	5.65×10^{18}	<i>p</i>

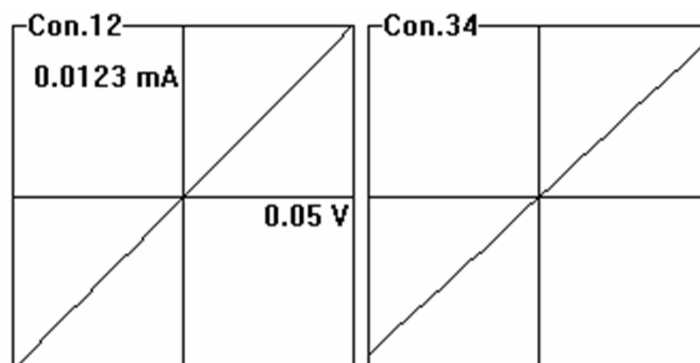


Figure 4-8 Typical I-V characteristic of ZnO films in Hall measurement. Ohmic contact was established on both the connector 1 & 2 and connector 3 & 4 in four-point probe van der Pauw method.

effect measurement. Nevertheless, the typical results are shown in Table 4-2 for reference. The ZnO thin film annealed in N₂, interestingly, shows *p*-type conduction consistently. Looking carefully on the electrical property of the N₂-annealed film, it has fairly high Hall mobility and hole concentration of 20.7 cm²/V-s and 5.65×10^{18} cm⁻³, respectively. Here we suggest that the N₂-annealed film has bi-carrier conduction behavior with majority carrier of hole. As the mobility of electron is much higher than hole's mobility (~ 200 times), the existence of electrons in the ZnO thin films will definitely affect the Hall effect measurement especially when the hole concentration is low.²²⁶

Temperature-dependent Hall effect measurement was carried out on the *p*-type C-doped ZnO thin film and the hole concentration versus temperature is shown in Figure 4-9. The experimental data (square dots) was fitted by

$$p = (N_D / N_A - 1)(g_{A1} / g_{A0}) N_V T^{3/2} \exp(-E_A / k_B T) \quad (4.5)$$

where N_D / N_A is the compensation ratio, the occupied and unoccupied state degeneracy are $g_{A1} = 1$ and $g_{A0} = 4$ respectively, N_V is $4.94 \times 10^{15} \text{ cm}^{-3} \text{ K}^{-3/2}$ by assuming the effective hole mass $m_h = m_0$, with m_0 as the electron rest mass, k_B is the Boltzman constant, and T is the absolute temperature.¹²⁸ The activation energy E_A and compensation ratio N_D / N_A was estimated to be 50.2 meV and 0.11, respectively, through the linear fitting. The N_D / N_A was found to be comparable with that in ZnO:N by Look *et al.*,¹²⁸ and better than that in ZnO:N by Tzukazaki *et al.*⁷⁷ The smaller activation energy suggested that the acceptors are shallow with about 50.2 meV above the valance band.

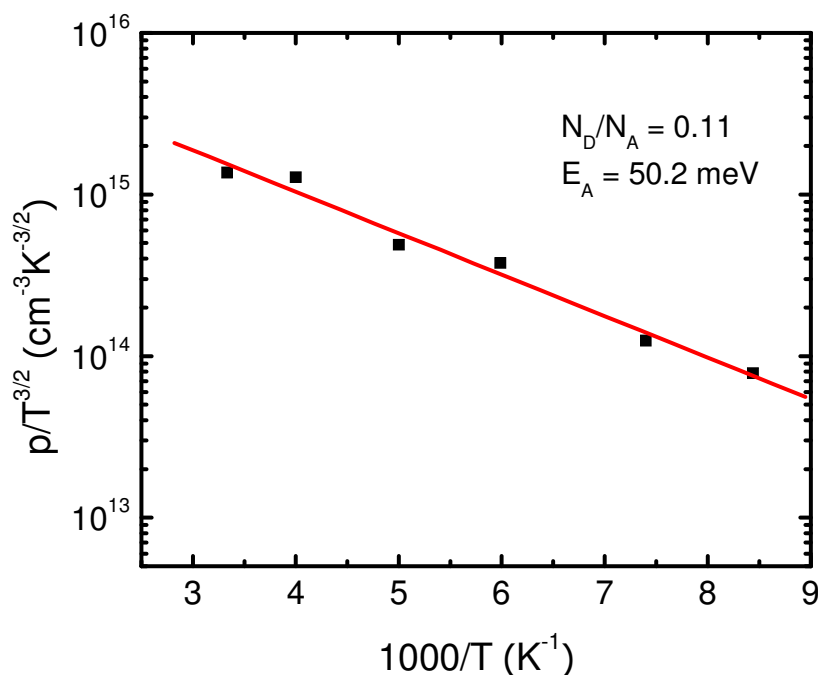


Figure 4-9 Hole concentration versus temperature of *p*-type C-doped ZnO thin film.

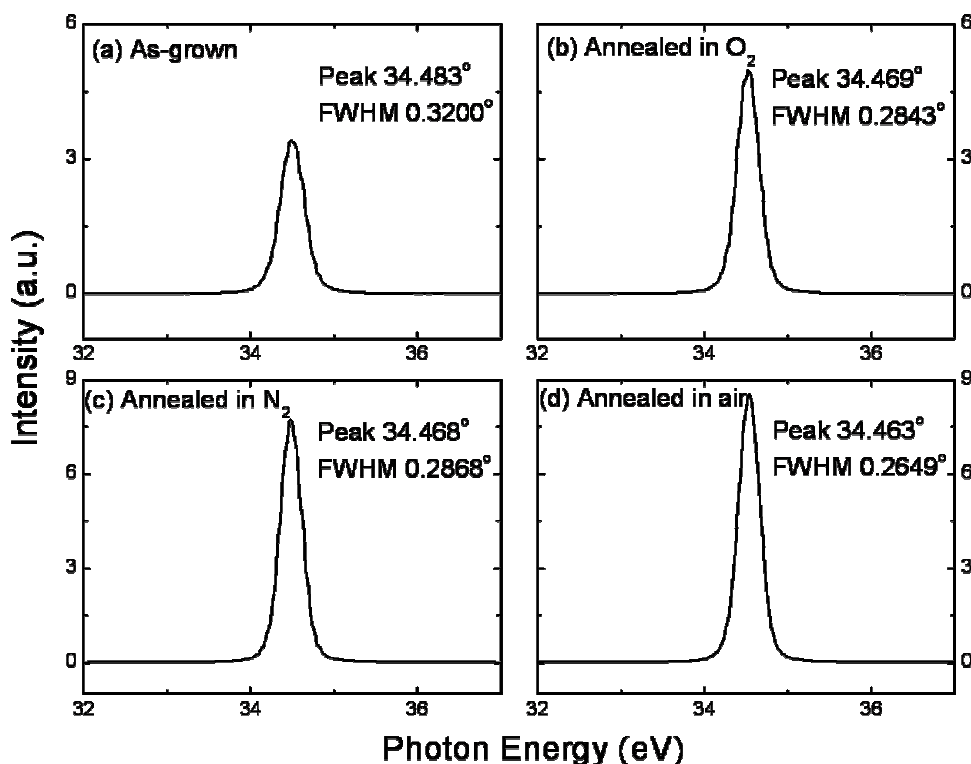


Figure 4-10 XRD spectra of as-grown and annealed ZnO thin films with different y-scale.

Peak position and FWHM of (0002) peak were indicated in the figure.

X-ray diffraction was carried out to confirm the crystal structures of the as-grown and annealed ZnO thin films. All the ZnO thin films exhibit only (0002) peak, as shown in Figure 4-10. The corresponding peak position and FWHM of the (0002) peak was indicated accordingly in the figure. As expected, the crystallinity of the ZnO thin films improved after the thermal annealing. The FWHM of (0002) peak reduces from 0.3200 degrees of as-grown films to 0.2843, 0.2868, and 0.2649 degrees after annealing in O₂, N₂, and air, respectively.

Other than carbon, which is an inevitable contaminant in MOCVD growth, no other contaminants such as In and Ga were detected in the ZnO thin films by using SIMS. Figure 4-11 shows the SIMS profiles of Zn, O, C, and Al of as-grown and annealed ZnO thin films. The difference in acquiring time for the four samples is mainly due to the measurement errors such as the stability of the sputter gun and charging

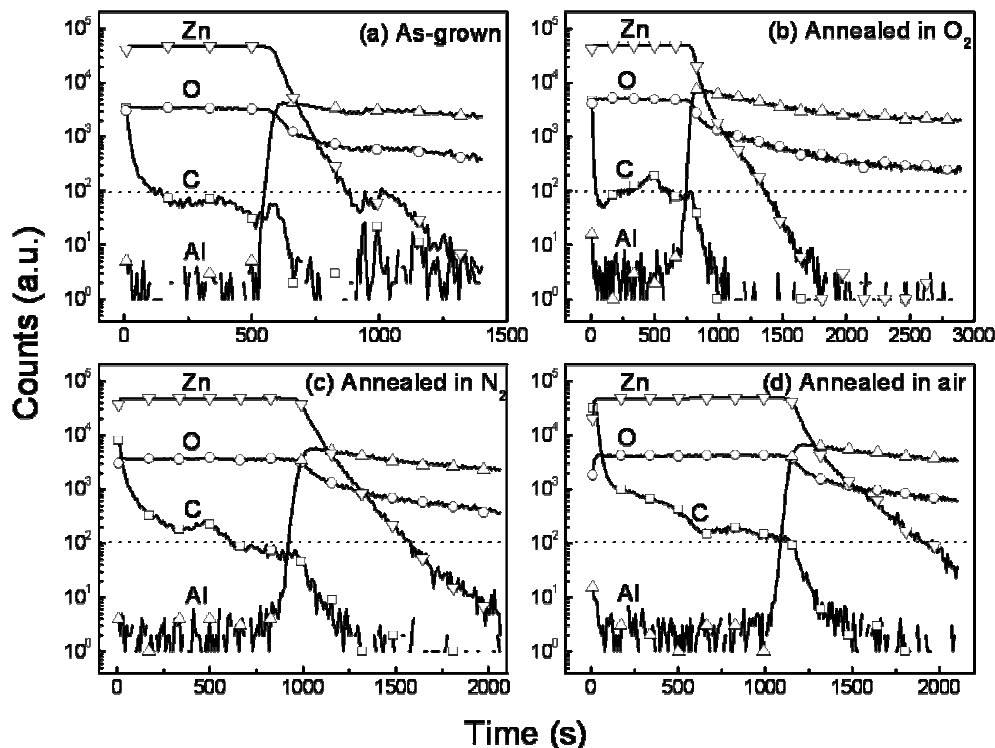


Figure 4-11 SIMS profile of as-grown and annealed ZnO thin films.

effect of the samples. It is seen that the C was doped into the ZnO thin films through the pyrolysis of the metal organic precursor. Judging the concentration of C with the aid of the inserted dotted line, it is found that the concentration of C in N_2 - and air-annealed ZnO thin films piled up at the surface. However, for weak n -type O_2 -annealed ZnO thin film, the C concentration remained or even decreased near the surface, indicating the active reaction between carbon and oxygen to form CO/CO₂ gas in high oxygen partial pressure ambient.

Figure 4-12 shows the XPS spectra which contain of C 1s and O 1s of all the ZnO thin films. For the C 1s spectra, the dotted baselines were added for better observation. Using the inserted baselines as reference, a weak peak was detected at 289.1 eV with a 2 eV of FWHM in the as-grown ZnO thin film. The peak is generally attributed to the COOR bonding that was introduced by the metal organic source.

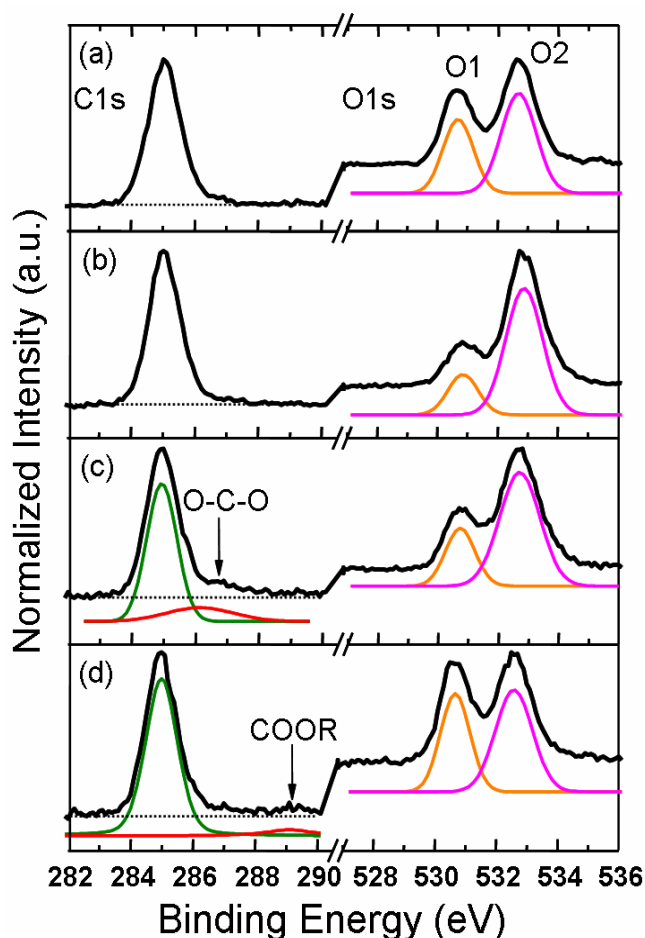


Figure 4-12 XPS spectra of C 1s and O 1s of (a) O₂-annealed, (b) air-annealed, (c) N₂-annealed and (d) as-grown ZnO thin films.

Beside the as-grown ZnO thin film, an additional peak is observed in the XPS spectra of N₂-annealed ZnO thin film. By deconvoluting the spectra, the peak is found centered at 286.1 eV with a FWHM of 1.8 eV. As the binding energy of C-OR is at 285.4 eV, the binding energy of 286.1 eV is suggested to be O-C-O complex. The O1s spectra of the ZnO thin films can be deconvoluted into two peaks centered at binding energies of 530.67 and 532.58 eV, respectively. The low binding energy at 530.67 eV, denoted by O1, corresponds to Zn-O bonding, while the higher binding energy peak located at 532.58 eV (O2) has always been regarded as absorbed oxygen species or hydroxyl.²²⁷ However, looking at the intensity of the O2 peak, it is impossible to detect such a huge amount of absorbed oxygen and hydroxyl in the

films since the films were pre-sputtered before the measurement. Hence, we believed that the O2 peak is mainly the binding energy of oxygen in the interstitial site (O_i). It is seen from Figure 4-12 that the O2 peak has comparable intensity with O1 peak in as-grown film but dominate the O1s spectra after annealing. The increase of O2 peak in annealed films suggests that the O atoms in ZnO lattice were induced and immobilized at the interstitial site by forming O-C-O complexes.

Room temperature PL was carried out to investigate the annealing effect on the ZnO thin films and is shown in Figure 4-13. The as-grown ZnO thin film exhibits two distinct emission bands, denoted as near-band-edge emission (NBE) and deep-level emission (DLE) that centered at 3.3093 and 2.4750 eV, respectively. As described in previous section, the NBE is excitonic-related emission from ZnO while the green color DLE is due to the radiative recombination of a photogenerated hole with an electron in singly ionized oxygen vacancy in ZnO thin films.¹⁹ After annealing, interestingly, an additional orange-red color DLE was observed in all

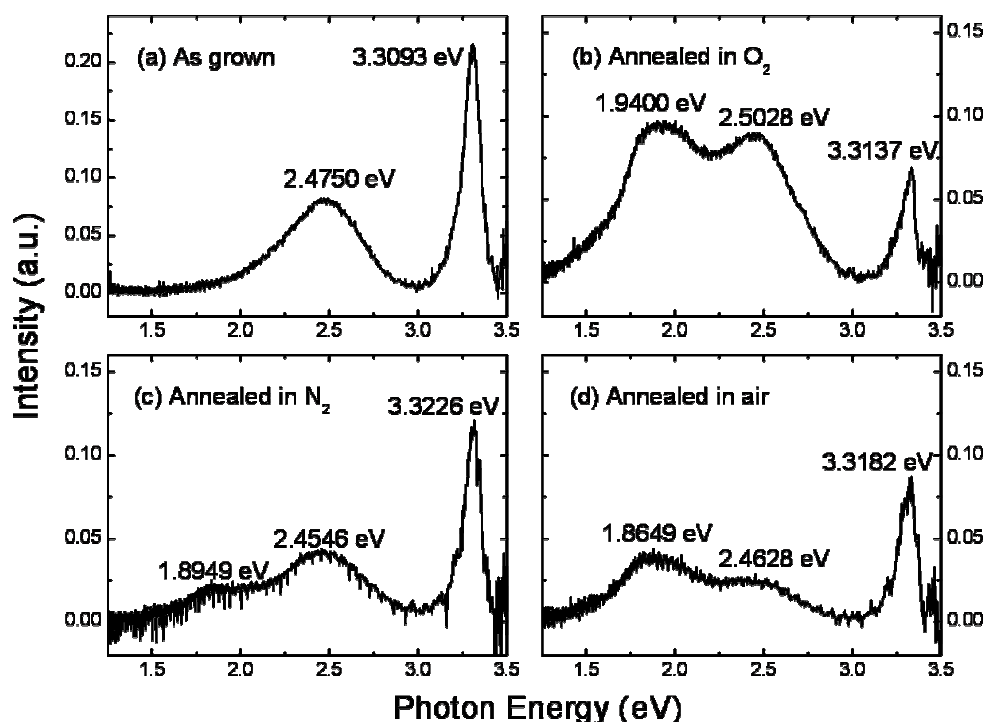


Figure 4-13 Room temperature PL spectra of as-grown and annealed ZnO thin films.

annealed films. The orange-red color DLE centered at 1.9400, 1.8949, and 1.8649 eV for O₂, N₂, and air-annealed ZnO thin films, respectively. The orange-red color DLE has been observed and attributed to the O_i-related deep acceptors.²²⁸ Combine with the electrical property measured by Hall measurement, it is noted that as the resistivity increases, the orange-red color DLE increases as well.

The cryogenic PL measurement was carried out to investigate the emission characteristic of the ZnO thin films. Figure 4-14 shows the normalize near-band-edge PL spectra of the ZnO thin films at 4.8 K. Free exciton with the A and B valence band (FX_A and FX_B) were observed at 3.375 eV and 3.387 eV, respectively in annealed films.²²⁹ The PL spectra of as-grown, O₂- and air-annealed films consist of neutral donor bound exciton (D⁰X) positioned at 3.3578, 3.3628, and 3.3610 eV, with the two-electron-satellite (TES) of the D⁰X located at 3.3321, 3.3330, and

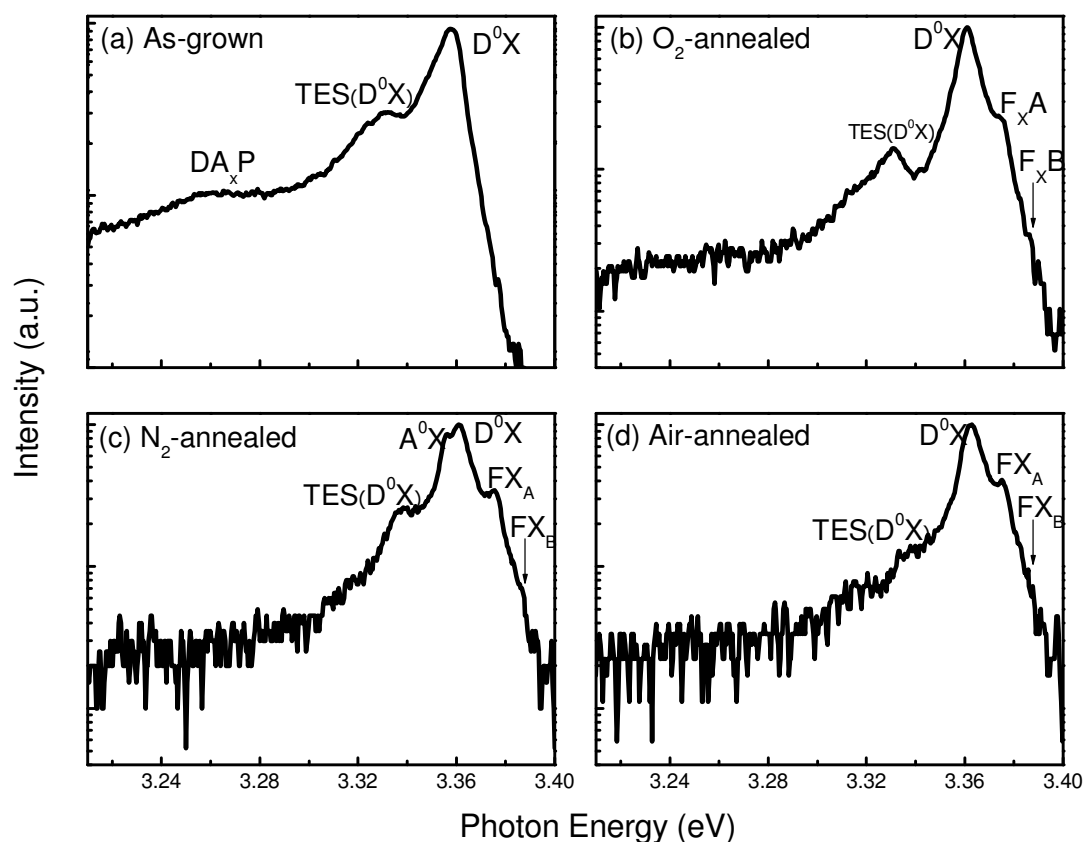


Figure 4-14 PL spectra of as-grown and annealed ZnO thin films at 4.8 K.

3.3307 eV, respectively.^{230, 231} Besides, the donor-acceptor-pair (DA_xP, with unknown acceptor) transition is found in as-grown ZnO thin films at 3.25 eV. The PL of the N₂-annealed film (Figure 4-14c), shows an additional peak position at 3.3564 eV. The peak is found to be a neutral acceptor bound exciton (A⁰X) according to Teke *et al.*²²⁹ Other than the A⁰X, D⁰X and TES(D⁰X) are also found at 3.3610 and 3.3384 eV, respectively. From the Hall effect measurement, the N₂-annealed film is found to have bi-carrier with majority of holes. Consistently, the PL measurement shows that the D⁰X intensity is comparable to A⁰X emission.

4.3.3 Summary

In summary, *p*-type unintentional carbon-doped ZnO thin films were realized after post-growth annealing. The carbon, induces and immobilizes the O_i to form O-C-O complex. The O-C-O complex has been evidently observed in XPS spectra. The acceptor in the *p*-type carbon-doped ZnO thin film is attributed to the oxygen interstitial and its A⁰X is positioned at 3.3564 eV. High carrier concentration in *p*-type ZnO thin films measured by Hall effect measurement and the coexistence of green and orange-red DLE in PL measurement might be due to the inhomogeneous of *p*-type ZnO region.

CHAPTER 5 ZNO SELF-ASSEMBLED NANOSTRUCTURES

5.1 Background

Nanostructured materials have attracted increasing interest recently due to their unique and novel properties over the bulk materials. For example, the large surface area of the nanostructures makes it a superior candidate in chemical and gas sensing application. Also, quantum confinement effect resulted from the shrinking in size will lead to new optical, electrical, and mechanical properties, which have opened up a new window for applications in optics, optoelectronics, biotechnology, chemistry, etc. In the past decades, various nanostructures have been synthesized from semiconducting oxides, such as ZnO,^{41,232,233,234} SnO₂,^{235,236} Ga₂O₃,²³⁷ and CdO.²³⁸ Among the semiconducting oxides, ZnO shows the richest nanostructural morphologies. In the past decade, in lure of the fascinating potential applications, ZnO nanostructures in zero-dimensional (0D) – quantum dots;^{133, 239 - 242} one-dimensional (1D) – wires, rods, tubes, and belts;^{41, 243-246} two-dimensional (2D) – quantum wells;^{247,248,249} and even three-dimensional (3D) – polyhedral spheres or shells,^{233,234,250-252} have been extensively synthesized and studied.

The hollow structures are expected to have wide application as reported by Jiang *et al.*²³³ and reference therein. As the hollow structures possess unique properties, they have received much attention and have been synthesized by several groups. Gao and Wang²³⁴ and Leung *et al.*²⁵⁰ have synthesized ZnO hollow spheres and shells by using solid-vapor deposition. Besides, polyhedral hollow beads and hollow microspheres have also been synthesized with the aid of ethanol droplets and PSS [poly(sodium 4-styrenesulfonate)] by Jiang *et al.*²³³ and Mo *et al.*²⁵¹ However, to our best knowledge, there is no report on ZnO hollow spheres synthesized by MOCVD.

As described previously, it is well known that the MOCVD has been practically used in optoelectronic industry to grow active layers of LEDs and LDs. The investigation of ZnO nanostructures by MOCVD has therefore attracted much attention.²⁵³⁻²⁵⁷ In this chapter, the self-assembled ZnO hollow spheres and stacking disks by MOCVD are presented. The structural and optical properties of the ZnO structures are investigated and the growth mechanism is discussed.

5.2 Experiment

The ZnO hollow spheres and stacking disks were synthesized on Si (111) wafers by MOCVD using the modified reactor and growth process as described in chapter 3. As the O₂ was obtained from the residual gas inside the chamber rather than continuously supplying O₂ gas, it is expected that the oxygen partial pressure will change with time and a near-zero oxygen partial pressure could be obtained within a particular period. The experiment was initiated by evacuating the chamber to 5×10^{-2} Torr, and then the growth was conducted at 350°C under a pressure of 25 Torr with N₂ background gas. The flow rate of the DEZn (carried by N₂) was maintained at 6 sccm and the DEZn source was kept at 5°C in a coolant water bath. The structures were collected on Si (111) wafer located just in front of the DEZn nozzle. The Si (111) wafer was cleaned by sequential ultrasonic baths of acetone, ethanol, and rinsed using de-ionized water. The ZnO nanostructures were investigated using a JEOL JSM-5910LV scanning electron microscopy (SEM) and the crystal structure was characterized by x-ray diffraction (XRD) using a Siemens D5005 x-ray diffractometer with CuK α radiation. High-resolution transmission electron microscopy (HRTEM) with accelerating voltage of 300 kV was employed to observe the lattice structure (JEOL 3010). The photoluminescence (PL) spectra of the ZnO thin films were

measured with a Renishaw 2000 micro-PL setup excited with the 325 nm line of a He-Cd laser at room temperature.

In this study, the growth was investigated as a function of time. Four samples were grown with the growth duration of 1, 5, 10, and 12 minutes, respectively at the same growth condition. The samples grown for 1 and 5 minutes have generally the same structural properties. Hence, only the 5-minute-grown sample will be discussed and compared with the samples grown for 10 and 12 minutes.

5.3 Results and Discussion

Figure 5-1 (a) and (b) show the SEM images of the film grown for 5 minutes taken with 0° and 45° viewing angle, respectively. It was observed that the film showed pillar-like structure with a diameter ranging from 150 to 200 nm. As the growth duration was prolonged to 10 minutes, the structures of the ZnO thin films changed drastically from pillar-like structures to sphere-like and disk-like structures. The samples grown for 10 and 12 minutes have the same morphology except that the 12-minute sample showed additional X-ray diffraction peaks correspond to metallic Zn.

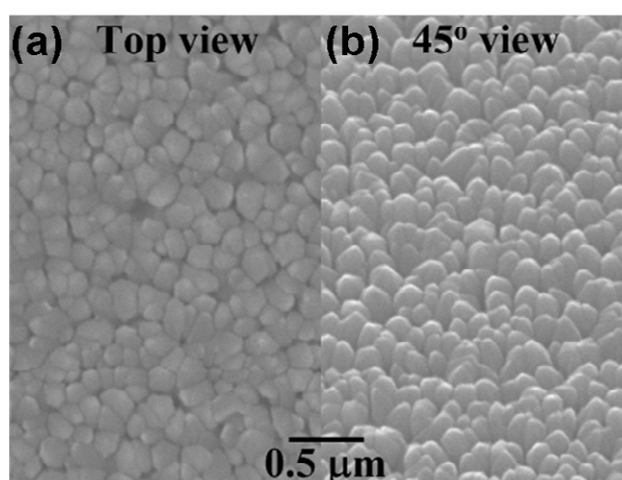


Figure 5-1 Top view and 45° view of SEM image of ZnO structures grown for 5 minutes.

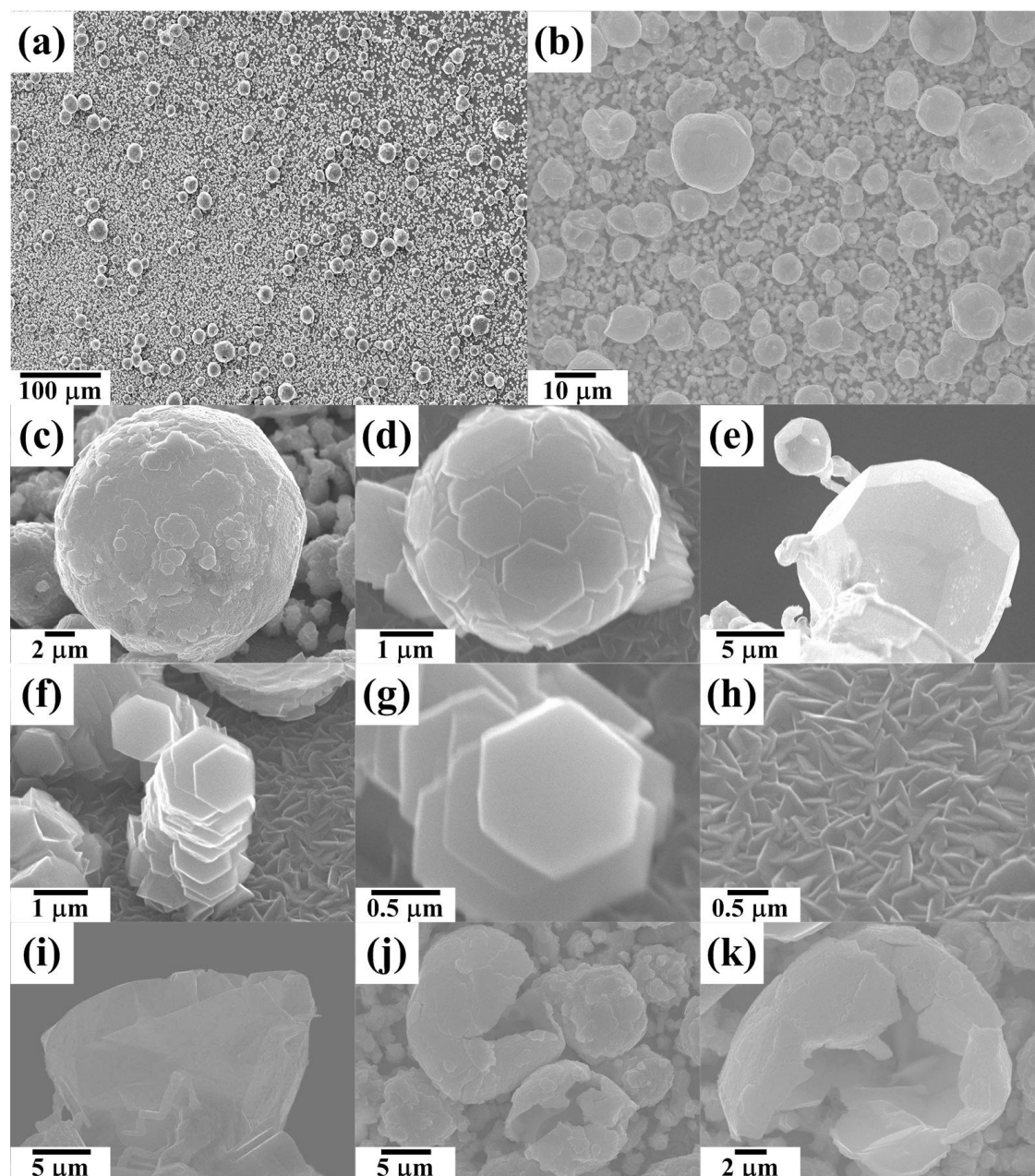


Figure 5-2 SEM images of (a-b) an overview morphology on silicon wafer. (c-e) Typical ZnO spheres with shell composed of hexagonal disks and nanocrystals. (f-h) ZnO hexagonal stacking and lying disks. (i-k) Collapsed and broken ZnO spheres.

Figure 5-2 (a) – (k) show the SEM images of the film grown for 10 minutes with various magnifications. The typical surface morphology of ZnO structure grown on Si (111) wafer is shown in Figure 5-2 (a) – (b). One may see that spherical shape structures were randomly distributed over the film. Examining the film with higher magnification, it can be seen that the ZnO structures consist of two different structures,

namely spheres and hexagonal stacking disks, as shown in Figure 5-2 (c) – (e), and Figure 5-2 (f) – (g), respectively. The spheres and hexagonal stacking disks structures were grown on a layer of disk-like ZnO thin film [Figure 5-2 (h)].

The spheres have the size ranging from several hundreds of nanometers to micrometers. Some of them are composed nicely of disk-like structures while some are composed of nanocrystals. It can be seen from Figure 5-2 (c) – (e) that some of the spheres are in polyhedral shape. Interestingly, the spheres are hollow as observed in SEM images of the collapsed and broken spheres as shown in Figure 5-2 (i) – (k). The shell thickness of the spheres was estimated to be in the range of 100 to 200 nm.

Figure 5-3 (a) – (b) and Figure 5-3 (c) – (d) show the TEM images of a broken and a fine spherical cage, respectively. The broken cage has a hollow spherical shape with the diameter of a few micrometers. It can be seen clearly from Figure 5-3 (b) that the shell of the broken cage is composed by a layer of hexagonal disks. The size of the disks was estimated to be 200 nm on the average. The inset between the Figure 5-3 (a) and (b) is the selected area electron diffraction (SAED) pattern of the shell. The incident electron beam is perpendicular to the hexagonal disks. Hence, the electron beam is along [0001] direction with a tilted angle. The SAED pattern reveals only one set of lattice, which matches that of ZnO. Figure 5-3 (c) – (d) show a fine spherical cage with diameter of 3 micrometers. Due to the presence of a structure underneath the cage, the SAED could not be performed. However, it is observed that there is a fine facet at the bottom of the spherical cage, and the shell with thickness of around 200 nm can also be clearly observed.

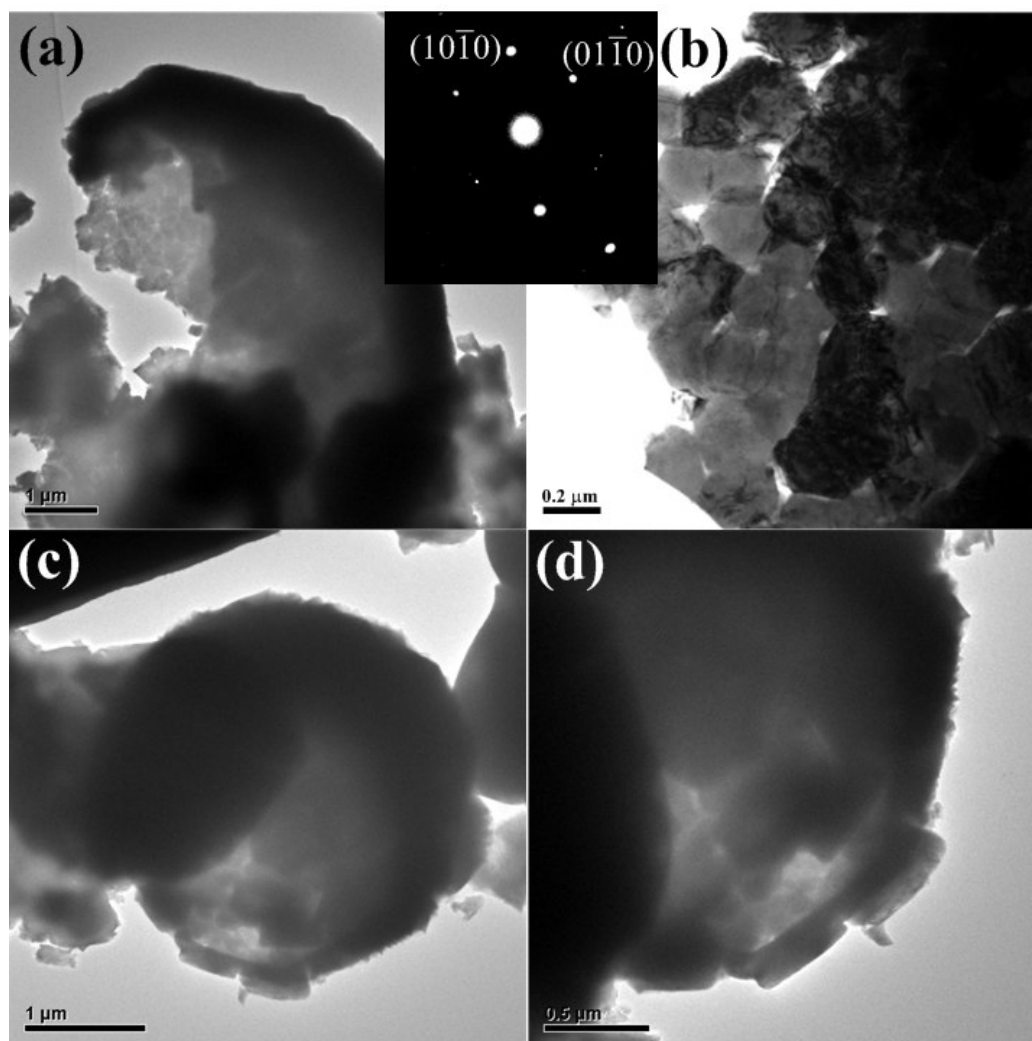


Figure 5-3 (a-b) TEM images of a broken cage and its SAED pattern (inset). (c-d) TEM images of a fine cage.

In addition to the hollow spheres, the stacking hexagonal disks are also found densely distributed over the wafer. The size of the disks ranges from 100 nm to 1 μm under the SEM observation. The TEM image of a hexagonal disk is shown in Figure 5-4 (a). Further insight into the hexagonal disk was obtained by HRTEM image and part of the edges is shown in Figure 5-4 (b). The Morie fringes that appear in the TEM images [Figure 5-4 (a) and (b)] are due to the interference of Bragg reflections of two crystal structures.²⁵⁸ It can be seen that there are two sets of lattices appeared at the edge of the hexagonal disk as is shown in Figure 5-4 (b). In fact, the SAED pattern

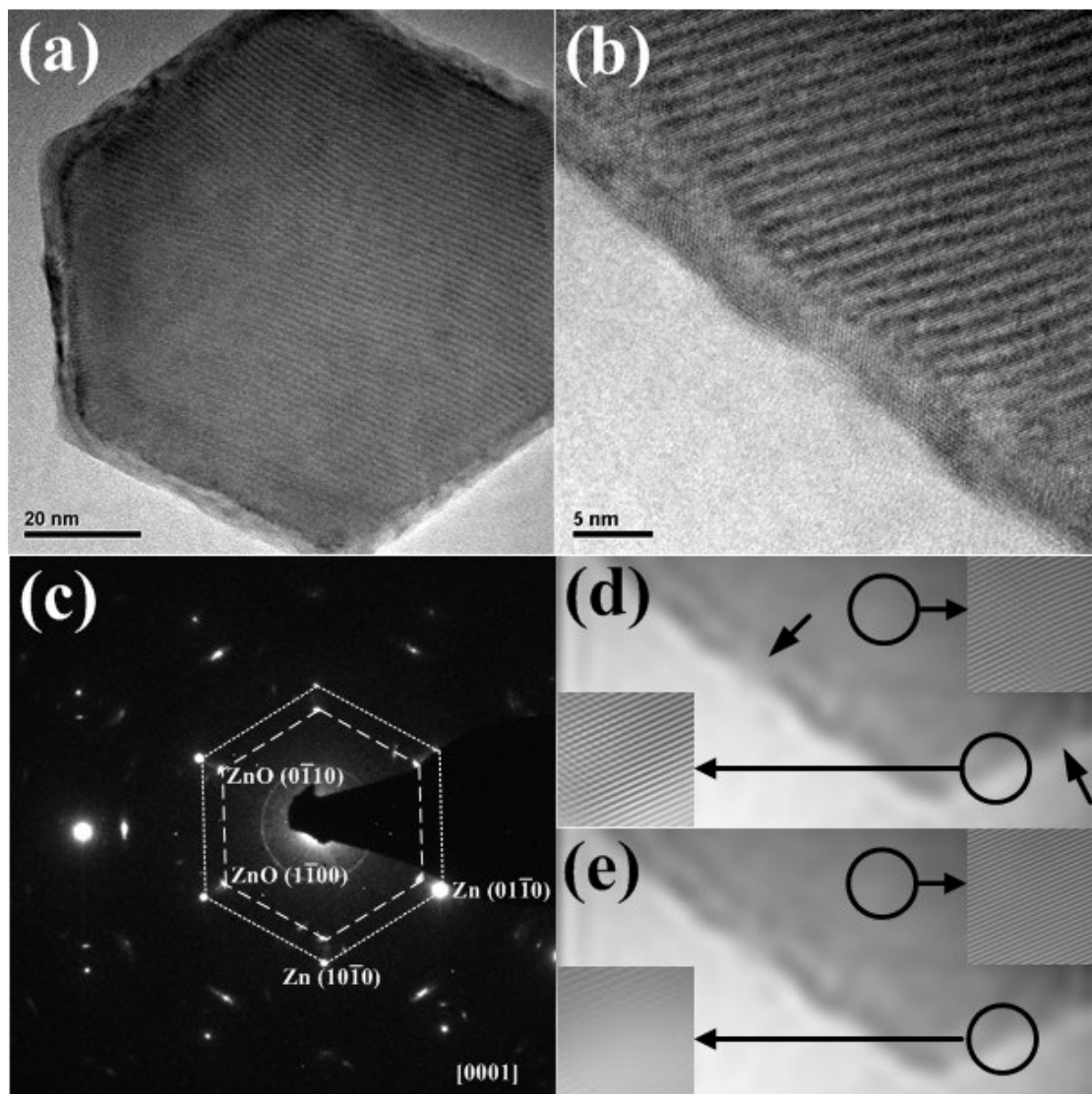


Figure 5-4 (a-b) TEM image of a typical ZnO hexagonal disk. (c) SAED pattern of the hexagonal disk showing two sets of lattice. (d-e) Lattice reconstruction by performing IFFT operation on metallic Zn and ZnO diffraction pattern, respectively. The arrowheads show the clear distinction between the two reconstructions.

in Figure 5-4 (c) evidently shows that the hexagonal disk consists of two crystal phases, i.e. metallic Zn and ZnO. An inversed fast Fourier transform (IFFT) operation was performed in order to reconstruct the lattice of metallic Zn and ZnO from the SAED pattern. Figure 5-4 (d) and (e) show the lattice reconstruction by IFFT of the metallic Zn and ZnO, respectively. It can be seen from the Figure 5-4 (d) that the

lattice reconstruction of the metallic Zn is clearly observed at the surface of the hexagonal disk especially at the edges, as indicated by arrowheads. The circled areas were enlarged to give a better observation for both Figure 5-4 (d) and (e). The observation in Figure 5-4 (d) and (e) evidently reveals the existence of metallic Zn and ZnO in the hexagonal disk structures.

The XRD measurement on the ZnO structures was carried out to confirm the composition of the structures. Figure 5-5 (a) to (c) show the XRD data of the ZnO structures grown with 5, 10, and 12 minutes, respectively. It can be seen that the ZnO structures grown within the first 10 minutes [Figure 5-5 (a) and (b)] consist of all the diffraction peaks that match with the ZnO wurtzite structure with lattice constants of $a=3.250$ and $c=5.207$ Å. The sample grown for 12 minutes consists of metallic Zn as shown in Figure 5-5 (c), indicating the formation of metallic Zn on the ZnO structures. The most intense peak in the sample grown for 10 minutes [Figure 5-5 (b)]

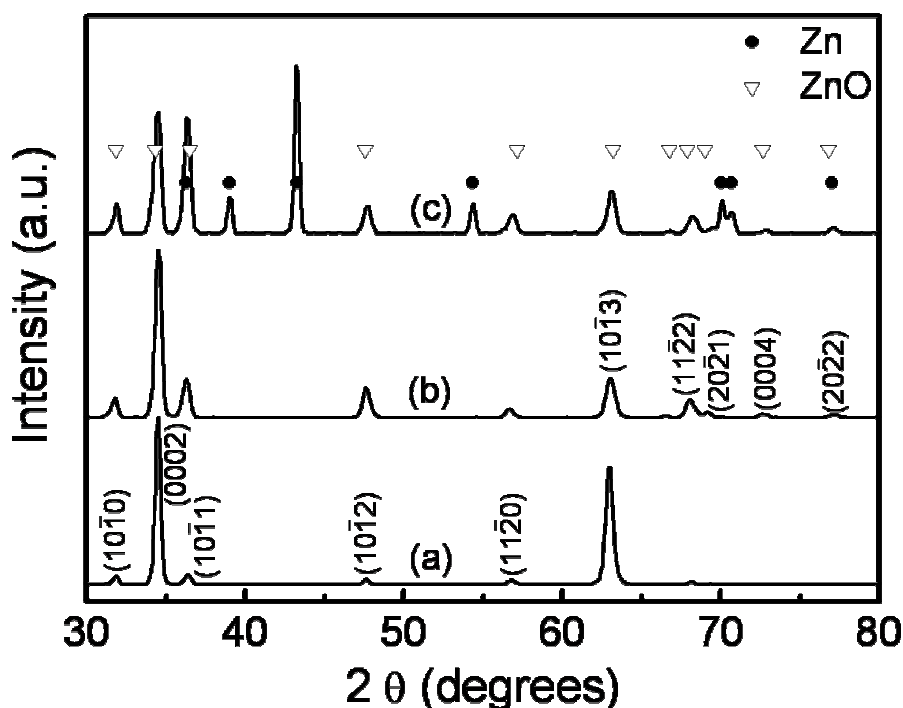


Figure 5-5 Normalized XRD of ZnO structures grown with (a) 5; (b) 10; and (c) 12 minutes.

The ZnO structures grown within 10 minutes show only ZnO related diffraction peaks.

was detected at 34.55° , which is due to the highly c-axis oriented film formed underneath the structures. Although the TEM images show that the hexagonal disks were surrounded by a layer of metallic Zn, no diffraction peaks of metallic Zn were detected. It is believed that the volume of metallic Zn in the ZnO structures is too small to be detected.

Figure 5-6 shows the normalized PL of the ZnO structures and ZnO thin film in logarithm scale. It is seen that the PL of the ZnO structures have a broader near-band-edge emission that tail up to 3.6 eV compared with those emit from ZnO thin film. However, there is no distinct blue-shift of PL emission peak in ZnO structures. This might due to the fact that the quantum confinement effect could be obvious only when the size is less than 2 nm in ZnO material. Nevertheless, the broad near-band-edge emission that tail up to 3.6 eV is due to the weak quantum confinement effect of those nanostructures.

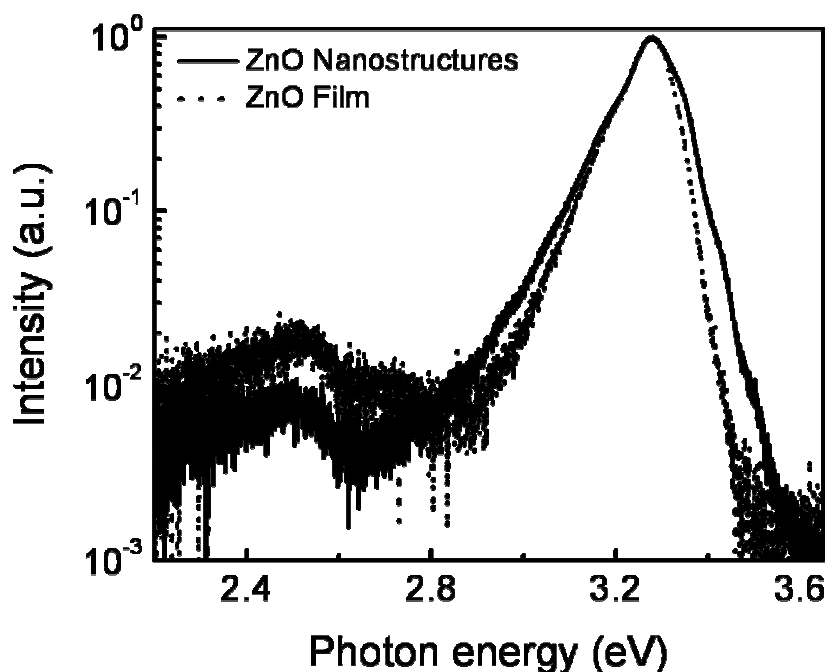


Figure 5-6 Normalized PL of ZnO structures grown with 10 minutes and ZnO thin film.

The growth mechanism of ZnO polyhedral spheres by solid-vapor deposition with the aid of SnO₂ and graphite was proposed by Gao and Wang.²³⁴ In their growth technique, the temperature used was in the range of 300 to 500°C, which was around the melting point of metallic Zn (419°C). Hence, the excess metallic Zn in the spheres was vaporized or sublimated through the mesoporous structures on the shell. In our case, the growth temperature was much lower than the melting point of the metallic Zn. Hence, the vaporization or sublimation of metallic Zn is unlikely to happen. In fact, the TEM images of the hexagonal disks reveals the truth that the structures consist of metallic Zn and ZnO, which acts as a strong evidence that the vaporization and sublimation of metallic Zn did not occur during the growth. Moreover, it is unlikely that the hollow spheres evolved from the oxidation of metallic Zn nuclei considering the fact that the hollow spheres have large diameter to thickness ratio of 50 (taking 10 μm sphere with shell thickness of 200 nm). Hence, it is unlikely to obtain such hollow spheres under this circumstance too. We speculate that in the near-zero oxygen partial pressure environment, the DEZn carried by N₂ gas accumulates on the substrate surface by forming hollow spheres or solid droplets as the result of surface energy minimization. The spheres or droplets will then be oxidized by the residue O₂ in the chamber to form ZnO hollow spheres or ZnO stacking disks.

The growth mechanism for the ZnO hollow spheres and hexagonal stacking disks structures by MOCVD system is proposed and shown in Figure 5-7. Figure 5-7 (a) shows the arriving of the precursors, i.e. DEZn and O₂ on the hot substrate. The organic ligand of DEZn is desorbed near the hot surface since the onset of pyrolysis for DEZn occurs at 332.3°C. At the initial stage of the growth, the decomposed Zn vapor will get oxidized immediately due to the rich residual O₂ in the chamber. Hence, a highly c-axis oriented ZnO thin film is formed initially at the sufficient

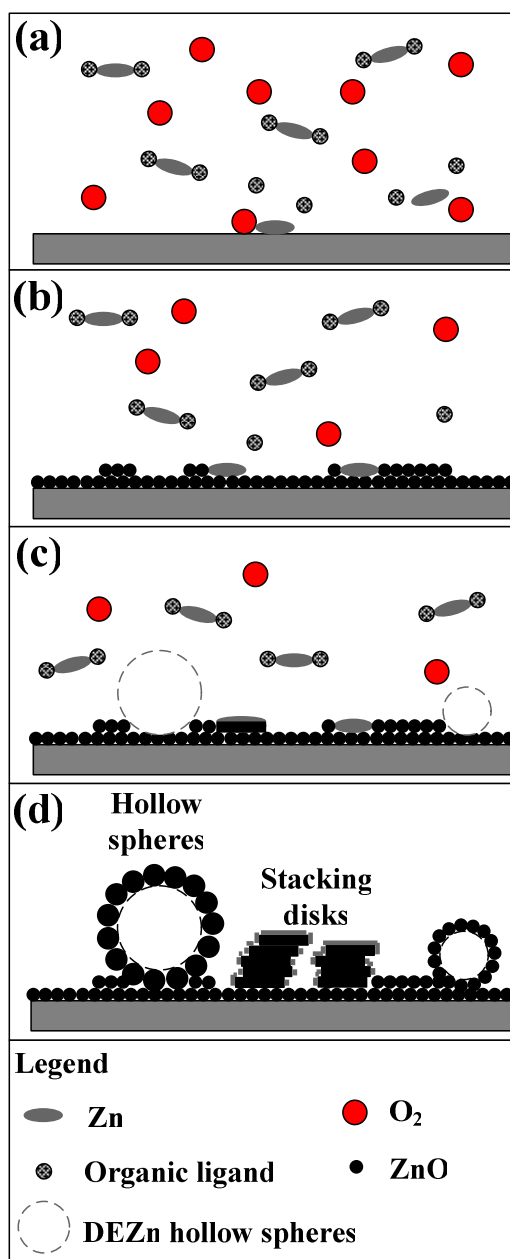
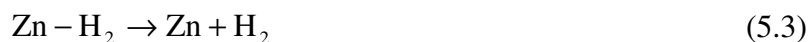
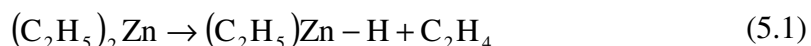


Figure 5-7 A cartoon showing the growth mechanism for the ZnO hollow spheres and stacking disks structures. (a) Both the DEZn and O₂ reach the hot substrate. (b) The DEZn were dissociated in O-rich environment and resulting in the formation of a highly c-axis textured ZnO layer. (c) As the O₂ partial pressure became less due to the formation of ZnO, the DEZn vapor accumulates and dissociate via beta hydride elimination process. The DEZn will form hollow spheres or droplets as a result of surface energy minimization. (d) Subsequent oxidation on the DEZn hollow spheres and droplets form the ZnO hollow spheres and hexagonal stacking disks. The thin metallic Zn layer on the top of the disks might be due to the Zn wetting layer that not fully oxidized due to the near-zero O₂ partial pressure environment.

supply of DEZn and O₂ [Figure 5-7 (b)]. However, at the later stage of growth, the residual O₂ became less due to the formation of ZnO thin film. In Zn-rich environment, DEZn vapor has slower oxidation rate and it may reach and accumulate on the substrate as shown in Figure 5-7 (c). The DEZn vapor may combine and form DEZn hollow spheres and droplets via beta hydride elimination progress:



The subsequent oxidation that occurs on the surface of the DEZn spheres or droplets will lead to the formation of ZnO hollow spheres and stacking disks, as shown in Figure 5-7 (d). The DEZn vapor that constantly wet the (0002) facet leads to the formation of ZnO hexagonal disks. In fact, the Zn wetting layer was evidently observed in the HRTEM characterization of the hexagonal disk (Figure 5-4). Similar observation has been reported by us previously on the ZnO disk-like structures synthesized by vapor-phase transport.²³² The disk-like structures were synthesized in a Zn-rich environment where the growth along c-axis was suppressed. In our experiment, the hollow spheres and stacking disks were obtained at the later stage of the 10-minute growth. Hence, it provides a strong support that the residue O₂ was vanishing when the growth approaching the end and the Zn-rich environment was achieved.

5.4 Summary

In summary, the ZnO hollow spheres and hexagonal stacking disks structures were synthesized by the MOCVD. The accumulation of DEZn vapor and the following beta hydride elimination process in Zn-rich environment enable the formation of ZnO hollow spheres and stacking disks. The existence of a metallic Zn layer on the structures in the prolonged growth indicates that the near-zero O₂ partial pressure was the key parameter to obtain ZnO hollow spheres and stacking disks structures.

CHAPTER 6 CONCLUSIONS AND RECOMMENDATIONS

6.1 *Conclusions*

MOCVD has been developed to specially cater for the growth of ZnO thin films and nanostructures. The pre-reaction of the precursors in gaseous phase during the growth facilitates the growth of ZnO QDs embedded films. The ZnO QDs are embedded in a form of amorphous phase ZnO matrix. The blue-shift of the optical bandgap (up to 4.06 eV) in nominally undoped ZnO thin films is observed and reported for the first time and it was found to be due to the absorption of amorphous phase ZnO. The quantum confinement of the ZnO QDs was also investigated with the dependency of QDs bandgap on dot size. The QDs size ranged from 3 to 12 nm with the most distributed QDs size of 7 nm were clearly observed by HRTEM. The broad near-band-edge emission of 3.0 to 3.6 eV from the ZnO QDs embedded films is due to the quantum confinement effect of the QDs.

In order to obtain high quality ZnO thin films, the MOCVD reactor and growth process have been modified to eliminate the pre-reaction of the precursors. In the modified reactor and growth process, highly c-axis oriented ZnO thin films were fabricated. Due to the non-uniformity injection of precursors and stationary substrate holder, the films obtained were polycrystalline. However, judging from the structural, optical, and electrical properties, the ZnO thin films obtained have good quality that is comparable to those single crystalline ZnO thin films.

Post-growth thermal annealing on MOCVD grown ZnO thin films was carried out and investigated. The surface morphology changed drastically from nanosheets to nanoneedles after annealing due to the well-known Ostwald ripening in the

CHAPTER 6 CONCLUSIONS AND RECOMMENDATIONS

temperature range of 600 to 800°C. The size and height of the nanoneedles are building up as the annealing temperature is increased from 600 to 800°C. As the annealing temperature was further increased to 900°C, other than Ostwald ripening, sintering mechanism was evidently observed. The activation energy for the Ostwald ripening was estimated in the first attempt and the value is at around 1.33 eV, which is likely to be governed by Zn atom migration. The experimental results suggest that the sintering mechanism might require higher activation energy compared to Ostwald ripening. Also, the thermal evaporation was observed and resulted in flattening of the nanoneedles. The outdiffusion of H atoms after annealing is responsible for the highly resistive ZnO thin films obtained at 600°C annealing. The subsequent annealing at higher temperatures (700 to 900°C) improved the crystallinity and in turn increased the Hall mobility compared to 600°C-annealed film. PL measurement at room temperature shows that the luminescence efficiency improves with crystallinity after annealing.

P-type conduction was demonstrated in nominal undoped and N-doped ZnO thin films. The *p*-type ZnO thin films can be obtained by adjusting the Zn:O ratio from 0.05 to 0.2. For N-doping, N₂O was deliberately introduced to dope N into the ZnO thin films. However, due to low dissociation efficiency of N₂O, the reproducibility of the *p*-type ZnO thin films is still a critical issue. Moreover, using the first generation MOCVD, the films obtained are in polycrystalline structures with abundant native defects. This will definitely further complicated the *p*-type ZnO thin films fabrication and investigation. After adopting a modified reactor and growth process, highly *c*-axis oriented ZnO thin films were achieved. *P*-type conductivity was revealed in the nominal undoped ZnO thin films after post-growth thermal annealing in N₂ ambient. The carbon, which is unavoidable in MOCVD-grown films,

immobilizes the oxygen in the interstitial site in ZnO after annealing. The O-C-O complexes and oxygen interstitial were confirmed by the XPS measurement. The cryogenic photoluminescence of the *p*-type carbon-doped film showed an additional peak at 3.3564 eV, which was attributed to the neutral acceptor bound exciton.

ZnO nanostructures, which have attracted great attention recently, were also fabricated and investigated by modified MOCVD reactor. By controlling the oxygen partial pressure, ZnO hollow spheres and hexagonal stacking disks structures were synthesized. The accumulation of DEZn vapor and the following beta hydride elimination process in Zn-rich environment enable the formation of ZnO hollow spheres and stacking disks. The existence of a metallic Zn layer on the structures in the prolonged growth indicates that the near-zero O₂ partial pressure was the key parameter to obtain ZnO hollow spheres and stacking disks structures.

6.2 Recommendations for future research

In this dissertation, all the results were based on the ZnO thin films and nanostructures grown by the first generation MOCVD system. Due to simplicity of the first generation MOCVD system, the films obtained are not single crystalline. Besides, the N-doping by using N₂O gas suffered from low dissociation efficiency and hence the *p*-type ZnO:N thin films was not investigated thoroughly.

From the experience of modifying the reactor design and growth process, a second generation of MOCVD system was designed and is being assembled. The second generation of MOCVD system is shown in Figure 6-1. In the second generation MOCVD system, a showerhead injection will be adopted in order to eliminate the pre-reaction of the precursors. For better uniformity and controllability, a rotational

CHAPTER 6 CONCLUSIONS AND RECOMMENDATIONS

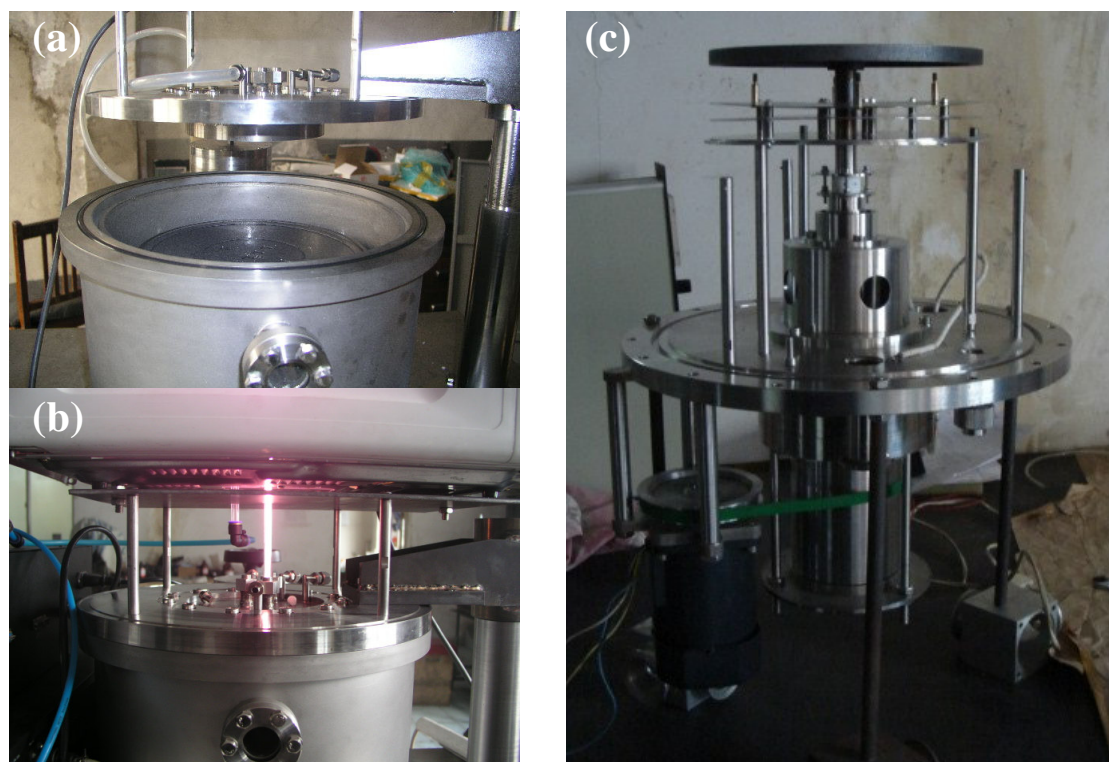


Figure 6-1 (a) Showerhead injection for MO and gas precursors. (b) Plasma ignition. (c) Rotational substrate holder with resistive coil heater that can heat up to 1000°C.

substrate holder with a maximum rotation speed of 500 rpm and a resistive heater source that can heat up to 1000°C were attached to the system. In addition, a microwave plasma source was attached to the system to increase the N doping efficiency in ZnO by dissociating the N_2 , N_2O , NO, or NH_3 gas. With the second generation MOCVD, it is expected to achieve high quality ZnO epitaxial films and *p*-type ZnO thin films could be investigated in depth.

Other than the N dopants, As, P, and Sb will be investigated parallelly in order to identify the best *p*-type dopant for ZnO. The investigation on the different *p*-type dopants by MOCVD can be performed due to the available of metal organic sources. Hence, the work is believed to have significant scientific contribution. Moreover, the preliminary results on *p*-type ZnO:C thin films have revealed that C might be a candidate to immobilize the *p*-type dopants, such as N, As, and P. Therefore, further

CHAPTER 6 CONCLUSIONS AND RECOMMENDATIONS

investigation on ZnO:C should be addressed.

Besides, one of the important tasks in ZnO research is to tailor its bandgap while reserving the crystal structure and lattice constant. In the proposed future work, bandgap engineering of ZnO alloy should be addressed by looking into different elements such as Mg, Be, Cd, Se, and S. So far, there is no report comparing these alloys efficiently with a particular growth technique. Hence, there is no firm conclusion on which elements are better for ZnO alloys. At the later stage of the research, quantum wells and *p*-type ZnO alloy films will be investigated with the combined effort of the *p*-type ZnO thin films and ZnO alloys. Last but not least, ZnO homojunctions and heterojunctions multiple quantum wells structures will be fabricated, tested, and optimized.

Journal publications

1. **S. T. Tan**, B. J. Chen, X. W. Sun, X. Hu, X. H. Zhang, and S. J. Chua, "Properties of polycrystalline ZnO thin films by metal-organic chemical-vapor deposition," *J. Cryst. Growth* **281**, 571 (2005).

2. **S. T. Tan**, B. J. Chen, X. W. Sun, M. B. Yu, X. H. Zhang, and S. J. Chua, "Realization of intrinsic *p*-type ZnO thin films by metal-organic chemical-vapor deposition," *IEEE/TMS J. Elec. Mater.* **34**, 1172 (2005).

Highlighted by TMS e-News August issue for paper of Editor's choice.

<http://www.tms.org/newsletter/archive/0508.asp>

3. **S. T. Tan**, B. J. Chen, X. W. Sun, W. J. Fan, H. S. Kwok, X. H. Zhang, and S. J. Chua, "Blueshift of optical bandgap in ZnO thin films grown by metal-organic chemical-vapor deposition," *J. Appl. Phys.* **98**, 013505 (2005).

4. **S. T. Tan**, X. W. Sun, X. H. Zhang, B. J. Chen, and S. J. Chua, "Optical properties of zinc oxide quantum dots embedded films by metal-organic chemical-vapor deposition." *Mater. Res. Soc. Symp. EE* **891**, 0891-EE10-05. (2005).

5. **S. T. Tan**, X. W. Sun, X. H. Zhang, B. J. Chen, S. J. Chua, Anna Yong, Z. L. Dong, and X. Hu, "Zinc oxide quantum dots embedded films by metal-organic vapor deposition," *J. Cryst. Growth* **290**, 518 (2006).

6. **S. T. Tan**, X. W. Sun, X. H. Zhang, S. J. Chua, B. J. Chen, and C. C. Teo, "Cluster coarsening in zinc oxide thin films by post-growth annealing" *J. Appl. Phys.* **100**, 033502 (2006).

Also selected and published in Virtual Journal of Nanoscale & Technology August 14, 2006 issue.

7. **S. T. Tan**, X. W. Sun, Z. G. Yu, P. Wu, G. Q. Lo, and D. L. Kwong, "*P*-type conduction in unintentional carbon-doped ZnO thin films" *Appl. Phys. Lett.* **91**, 072101 (2007).

8. **S. T. Tan**, X. W. Sun, X. H. Zhang, S. J. Chua, S. Y. Chow, A. M. Yong, G. Q. Lo, and D. L. Kwong, "Self assembled ZnO hollow spheres and hexagonal stacking disks by metal organic chemical vapor deposition." *Int. J. Nanotechnol.*, in press.

9. Z. W. Zhao, B. K. Tay, J. S. Chen, J. F. Hu, X. W. Sun, and **S. T. Tan**, "Optical properties of nanocluster-assembled ZnO thin films by nanocluster-beam deposition." *Appl. Phys. Lett.* **87**, 251912 (2005).

10. C. X. Xu, X. W. Sun, Z. L. Dong, **S. T. Tan**, Y. P. Cui, and B. P. Wang, "Maganese-doped zinc oxide tetratubes and their photoluminescent properties." *J. Appl. Phys.* **98**, 113513 (2005).

11. W. J. Fan, J. B. Xia, P. A. Agus, **S. T. Tan**, S. F. Yu, and X. W. Sun, "Band parameters and electronic structures of wurtzite ZnO and ZnO/ZnMgO quantum wells." *J. Appl. Phys.* **99**, 013702 (2006).

12. W. J. Fan, A. P. Abiyasa, **S. T. Tan**, S. F. Yu, X. W. Sun, J. B. Xia, Y. C. Yeo, M. F. Li, and T. C. Chong, "Electronic structures of wurtzite ZnO and ZnO/ZnMgO quantum well." *J. Cryst. Growth* **287**, 28 (2006).

13. A. Wei, X. W. Sun, C. X. Xu, Z. L. Dong, Y. Yang, **S. T. Tan**, and W. Huang, "Growth mechanism of tabular ZnO formed in aqueous solution." *Nanotechnology* **17**, 1740 (2006).

14. Chen Li, Wei Lei, Xiaobing Zhang, J. X. Wang, X. W. Sun, and **S. T. Tan**, "Fabrication and field emission properties of regular hexagonal flower-like ZnO nano-whiskers." *J. Vac. Sci. Tech. B* **25**, 590 (2007).

Conference presentations

1. International Conference on Materials for Advanced Technologies (ICMAT), Singapore, 3 July to 8 July 2005. Poster presentation, “Effects of growth temperature and precursors flow rate on the properties of ZnO thin films grown by metal-organic chemical-vapor deposition.”
2. Material Research Society (MRS) Fall Meeting, Boston, United States, 28 Nov to 2 Dec 2005. Poster presentation, “Optical properties of zinc oxide quantum dots embedded films by metal-organic chemical-vapor deposition.”
3. NanoSingapore, IEEE Conference on Emerging Technologies – Nanoelectronics, Singapore 10 Jan to 13 Jan 2006. Oral presentation, “ZnO nanostructures grown by metal-organic chemical-vapor deposition.”
4. 2nd Material Research Society – Singapore (MRS-S) Conference on Advanced Materials, Singapore, 18 Jan to 20 Jan 2006. Poster presentation, “Ostwald ripening of zinc oxide by post-growth annealing.”
5. Institute of High Performance Computing (IHPC) Science & Engineering Colloquium, 22 Aug 2006. Oral presentation, “Unintentionally carbon-doped ZnO thin films by MOCVD.”
6. Symposium on Microelectronics, Singapore, 29 Sept 2006. Oral presentation, “*P*-type conduction in nominal undoped ZnO thin films by post-growth thermal annealing.”
7. Asia Display, Shanghai, China, 12 March to 15 March 2007. Oral presentation, “*P*-type carbon-doped ZnO thin films by MOCVD.”

AWARDS

Awards

1. Best paper award in Asia Display 2007, “*P*-type carbon-doped ZnO thin films by MOCVD”.
2. Second prize in A*STAR Science and Engineering Research Council (SERC) Inter-Research Institutes poster symposium 2005, “Blueshift of optical bandgap in ZnO thin films grown by metal-organic chemical-vapor deposition”.
3. First prize in Institute of Materials Research and Engineering (IMRE) postgraduate students poster competition 2005, “ZnO nanocrystals grown by metal-organic chemical-vapor deposition.”

BIBLIOGRAPHY

Bibliography

-
- ¹ http://nobelprize.org/nobel_prizes/physics/laureates/1956/index.html
- ² R. W. Brander, "A review of the merits of direct and indirect gap semiconductors for electroluminescence devices," *Rev. Phys. Tech.* **3**, 145 (1972).
- ³ <http://www.lucint.com/minds/transistor/inventors.html>
- ⁴ <http://www.LightEmittingDiodes.org>
- ⁵ B. Niesing, "Blue diode laser science," *Fraunhofer Magazine* **2**, 14 (2001).
- ⁶ Communication with Exploit Technologies Pte. Ltd., Singapore.
- ⁷ <http://www.toptica.com/index.php?categorie=1&itemid=125>
- ⁸ http://www.otherpower.com/otherpower_lighting.html
- ⁹ <http://www.conceptscm.net/scanmark/sm4.htm>
- ¹⁰ <http://www.se-world.info/datenblatt.php?product=62>
- ¹¹ http://www.scoreboards.net/video_indoor.htm
- ¹² T. Hirao, M. Furuta, H. Furuta, T. Matsuda, T. Hiramatsu, H. Hokari, and M. Yoshida, "High mobility top-gate zinc oxide thin-film transistors (ZnO-TFTs) for active-matrix liquid crystal displays," *SID 06 Digest*, 18 (2006).
- ¹³ http://www.optowire.com/COHR/cohr_AVIA355X.html
- ¹⁴ http://www.teq.ch/it/products/boards_cont.html
- ¹⁵ http://www.artofthestate.co.uk/london_photos/Traffic_Light_Sculpture.htm
- ¹⁶ S. Okubo, <http://www.nonydesigns.com/site/780912/page/668531>
- ¹⁷ <http://encyclopedia.thefreedictionary.com/Times%20Square>
- ¹⁸ http://www.pbase.com/livaldi/red_bridge
- ¹⁹ K. Vanheusden, C. H. Seager, W. L. Warren, D. R. Tallant, and J. A. Voigt, "Correlation between photoluminescence and oxygen vacancies in ZnO phosphors," *Appl. Phys. Lett.* **68**, 403 (1996).
- ²⁰ Y. K. Park, J. Y. Han, M. G. Kwak, H. Yang, S. H. Ju, and W. S. Cho, "Effect of coupling structure of Eu on the photoluminescent characteristics for ZnO:EuCl₃ phosphors," *Appl. Phys. Lett.* **72**, 668 (1998).
- ²¹ G. D. Mahan, "Intrinsic defects in ZnO varistors," *J. Appl. Phys.* **54**, 3825 (1983).
- ²² S. Ezhilvalavan, and T. R. N. Kutty, "High-frequency capacitance resonance of ZnO-based varistor ceramics," *Appl. Phys. Lett.* **69**, 3540 (1996).
- ²³ K. Keis, E. Magnusson, H. Lindstrom, S. E. Lindquist, and A. Hagfeldt, "5% efficient photoelectrochemical solar cell based on nanostructured ZnO electrodes," *Solar Energy Mater. and Solar Cells* **73**, 51 (2002).

BIBLIOGRAPHY

- ²⁴ M. Izaki, and T. Omi, "Transparent zinc oxide films prepared by electrochemical reaction," *Appl. Phys. Lett.* **68**, 2439 (1996).
- ²⁵ P. Petrou, R. Singh, and D. E. Brodie, "The use of ZnO in transparent type MIS solar cells," *Appl. Phys. Lett.* **35**, 930 (1979).
- ²⁶ D. Gruber, F. Kraus, and J. Muller, "A novel gas sensor design based on CH₄/H₂/H₂O plasma etched ZnO thin films," *Sensors and Actuators B* **92**, 81 (2003).
- ²⁷ H. Nanto, T. Minami, and S. Takata, "Zinc-oxide thin-film ammonia gas sensors with high sensitivity and excellent selectivity," *J. Appl. Phys.* **60**, 482 (1986).
- ²⁸ X. W. Sun, and H. S. Kwok, "Optical properties of epitaxially grown zinc oxide films on sapphire by pulsed laser deposition," *J. Appl. Phys.* **86**, 408 (1999).
- ²⁹ R. F. Xiao, H. B. Liao, N. Cue, X. W. Sun, and H. S. Kwok, "Growth of *c*-axis oriented gallium nitride thin films on an amorphous substrate by the liquid-target pulsed laser deposition technique," *J. Appl. Phys.* **80**, 4226 (1996).
- ³⁰ R. L. Hoffman, B. J. Norris, and J. F. Wager, "ZnO-based transparent thin-film transistors," *Appl. Phys. Lett.* **82**, 733 (2003).
- ³¹ P. F. Carcia, R. S. Mclean, M. H. Reilly, and G. Nunes, Jr., "Transparent ZnO thin-film transistor fabricated by rf magnetron sputtering," *Appl. Phys. Lett.* **82**, 1117 (2003).
- ³² E. M. C. Fortunato, P. M. C. Barquinha, A. C. M. B. G. Pimentel, A. M. F. Goncalves, A. J. S. Marques, R. F. P. Martins, and L. M. N. Pereira, "Wide bandgap high-mobility ZnO thin-film transistors produced at room temperature," *Appl. Phys. Lett.* **85**, 2541 (2004).
- ³³ S. C. Jain, M. Willander, J. Narayan and R. Van Overstraeten, "III-nitrides: Growth, characterization, and properties," *J. Appl. Phys.* **87**, 965 (2000).
- ³⁴ H. Amano, M. Kito, K. Hiramatsu, and I. Akasaki, "*P*-type conduction in Mg-doped GaN treated with low-energy electron beam irradiation," *Jpn. J. Appl. Phys. Part II* **28**, L2112 (1989).
- ³⁵ S. Nakamura, N. Iwasa, M. Senoh, and T. Mukai, "Hole compensation mechanism of *p*-type GaN films," *Jpn. J. Appl. Phys.* **31**, 1258 (1992).
- ³⁶ S. Nakamura, M. Senoh, N. Iwasa, and S. Nagahama, "High-brightness InGaN blue, green and yellow light-emitting diodes with quantum-well structures," *Jpn. J. Appl. Phys. Part II* **34**, L797 (1995).
- ³⁷ H. P. Maruska, "A brief history of GaN blue light-emitting diodes," http://www.onr.navy.mil/sci_tech/31/312/ncsr/materials/gan/maruskastory.asp.
- ³⁸ S. Nakamura, M. Senoh, S. Nagahama, N. Iwasa, T. Yamada, T. Matsushita, H. Kiyoku, and Y. Sugimoto, "InGaN-based multi-quantum-well structure laser diodes," *Jpn. J. Appl. Phys. Part II* **35**, L74 (1996).

BIBLIOGRAPHY

-
- ³⁹ S. Nakamura, M. Senoh, S. Nagahama, N. Iwasa, T. Yamada, T. Matsushita, H. Kiyoku, and Y. Sugimoto, "InGaN multi-quantum-well structure laser diodes with cleaved mirror cavity facets," *Jpn. J. Appl. Phys. Part II* **35**, L217 (1996).
- ⁴⁰ S. Nakamura, M. Senoh, S. Nagahama, N. Iwasa, T. Yamada, T. Matsushita, Y. Sugimoto, and H. Kiyoku, "Room-temperature continuous-wave operation of InGaN multi-quantum-well structure laser diodes with a lifetime of 27 hours," *Appl. Phys. Lett.* **70**, 1417 (1997).
- ⁴¹ M. H. Huang, S. Mao, H. Feick, H. Yan, Y. Wu, H. Kind, E. Weber, R. Russo, and P. Yang, "Room-temperature ultraviolet nanowire nanolasers," *Science* **292**, 1897 (2001).
- ⁴² Robert F. Service, "Will UV lasers beat the blues?" *Science* **276**, 895 (1997).
- ⁴³ X. W. Sun, S. F. Yu, C. X. Xu, C. Yuen, B. J. Chen, and S. Li, "Room-temperature ultraviolet lasing from zinc oxide microtubes," *Jpn. J. Appl. Phys. Part II* **42**, L1229 (2003).
- ⁴⁴ H. Cao, Y. G. Zhao, S. T. Ho, E. W. Seelig, Q. H. Wang, and R. P. H. Chang, "Random laser action in semiconductor powder," *Phys. Rev. Lett.* **82**, 2278 (1999).
- ⁴⁵ H. Cao, X. Jiang, Y. Ling, J. Y. Xu, and C. M. Soukoulis, "Mode repulsion and mode coupling in random lasers," *Phys. Rev. B* **67**, 161101 (2000).
- ⁴⁶ Z. K. Tang, G. K. L. Wong, P. Yu, M. Kawasaki, A. Ohtomo, H. Koinuma, and Y. Segawa, "Room-temperature ultraviolet laser emission from self-assembled ZnO microcrystallite thin films," *Appl. Phys. Lett.* **72**, 3270 (1998).
- ⁴⁷ D. M. Bagnall, Y. F. Chen, Z. Zhu, T. Yao, S. Koyama, M. Y. Shen, and T. Goto, "Optically pumped lasing of ZnO at room temperature," *Appl. Phys. Lett.* **70**, 2230 (1997).
- ⁴⁸ P. Zu, Z. K. Tang, G. K. L. Wong, M. Kawasaki, A. Ohtomo, H. Koinuma, and Y. Segawa, "Ultraviolet spontaneous and stimulated emissions from ZnO microcrystallite thin films at room temperature," *Solid State Commu.* **103**, 459 (1997).
- ⁴⁹ T. Makino, Y. Segawa, M. Kawasaki, A. Ohtomo, R. Shiroki, K. Tamura, T. Yasuda, and H. Koinuma, "Bandgap engineering based on $\text{Mg}_x\text{Zn}_{1-x}\text{O}$ and $\text{Cd}_y\text{Zn}_{1-y}\text{O}$ ternary alloy films," *Appl. Phys. Lett.* **78**, 1237 (2001).
- ⁵⁰ Y. R. Ryu, T. S. Lee, J. A. Lubguban, A. B. Corman, H. W. White, J. H. Leem, M. S. Han, Y. S. Park, C. J. Youn, and W. J. Kim, "Wide-bandgap oxide alloy: BeZnO," *Appl. Phys. Lett.* **88**, 052103 (2006).
- ⁵¹ T. Jansseune, "Indium price soars as demand for displays continues to grow," <http://www.compoundsemiconductor.net/articles/magazine/11/5/5/1/CSind3%5F05%2D05>.
- ⁵² D. C. Look, "Recent advances in ZnO materials and devices," *Mater. Sci. Eng. B* **80**, 383 (2001).
- ⁵³ S. J. Pearton, D. P. Norton, K. Ip, Y. W. Heo, and T. Steiner, "Recent advances in processing of ZnO," *J. Vac. Sci. Technol. B* **22**, 932 (2004).

BIBLIOGRAPHY

-
- ⁵⁴ U. Ozgur, Ya. I. Alivov, C. Liu, A. Teke, M. A. Reshchikov, S. Dogan, V. Avrutin, S. J. Cho, and H. Morkoc, "A comprehensive review of ZnO materials and devices," *J. Appl. Phys.* **98**, 041301 (2005).
- ⁵⁵ Z. L. Wang, "Zinc oxide nanostructures: growth, properties and applications," *J. Phys.: Condens. Matter* **16**, R829 (2004).
- ⁵⁶ S. W. Kim, S. Fujita, and S. Fujita, "Self-organized ZnO quantum dots on SiO₂/Si substrates by metalorganic chemical-vapor deposition," *Appl. Phys. Lett.* **81**, 5036 (2002).
- ⁵⁷ W. J. Fan, J. B. Xia, P. A. Agus, S. T. Tan, S. F. Yu, and X. W. Sun, "Band parameters and electronic structures of wurtzite ZnO and ZnO/ZnMgO quantum wells," *J. Appl. Phys.* **99**, 013702 (2006).
- ⁵⁸ S. B. Zhang, S. H. Wei, and Alex Zunger, "A phenomenological model for systematization and prediction of doping limits in II-VI and I-III-VI₂ compounds," *J. Appl. Phys.* **83**, 3192 (1998).
- ⁵⁹ S. B. Zhang, S. H. Wei, and Alex Zunger, "Intrinsic *n*-type versus *p*-type doping asymmetry and the defect physics of ZnO," *Phys. Rev. B* **63**, 075205 (2001).
- ⁶⁰ Y. F. Yan, S. B. Zhang, and S. T. Pantelides, "Control of doping by impurity chemical potentials: Predictions for *p*-type ZnO," *Phys. Rev. Lett.* **86**, 5723 (2001).
- ⁶¹ C. H. Park, S. B. Zhang, and Su-Huai Wei, "Origin of *p*-type doping difficulty in ZnO: The impurity perspective," *Phys. Rev. B* **66**, 073202 (2002).
- ⁶² I. W. Tao, M. Jurkovic, and W. I. Wang, "Doping of ZnTe by molecular beam epitaxy," *Appl. Phys. Lett.* **64**, 1848 (1994).
- ⁶³ J. H. Chang, T. Takai, B. H. Koo, J. S. Song, T. Handa, and T. Yao, "Aluminum-doped *n*-type ZnTe layers grown by molecular-beam epitaxy," *Appl. Phys. Lett.* **79**, 785 (2001).
- ⁶⁴ R. Kalish, "The search for donors in diamond," *Diamond Relat. Mater.* **10**, 1749 (2001).
- ⁶⁵ C. G. Van de Walle, "Hydrogen as a cause of doping in zinc oxide," *Phys. Rev. Lett.* **85**, 1012 (2000).
- ⁶⁶ K. Ip, M. E. Overberg, Y. W. Heo, D. P. Norton, S. J. Pearton, S. O. Kucheyev, C. Jagadish, J. S. Williams, R. G. Wilson, and J. M. Zavada, "Thermal stability of ion-implanted hydrogen in ZnO," *Appl. Phys. Lett.* **81**, 3996 (2002).
- ⁶⁷ X. N. Li, B. Keyes, S. Asher, S. B. Zhang, S. H. Wei, T. J. Coutts, S. Limpijumnong, and C. G. Van de Walle, "Hydrogen passivation effect in nitrogen-doped ZnO thin films," *Appl. Phys. Lett.* **86**, 122107 (2005).
- ⁶⁸ T. Aoki, Y. Hatanaka, and D. C. Look, "ZnO diode fabricated by excimer-laser doping," *Appl. Phys. Lett.* **76**, 3257 (2000).

BIBLIOGRAPHY

-
- ⁶⁹ H. Hosono, H. Ohta, K. Hayashi, M. Orita, and M. Hirano, "Near UV emitting diodes based on a transparent *p-n* junction composed of heteroepitaxially grown *p*-SrCu₂O₂ and *n*-ZnO," *J. Cryst. Growth* **237**, 496 (2002).
- ⁷⁰ Q. X. Yu, B. Xu, Q. H. Wu, Y. Liao, G. Z. Wang, R. C. Fang, H. Y. Lee, and C. T. Lee, "Optical properties of ZnO/GaN heterostructure and its near-ultraviolet light-emitting diode," *Appl. Phys. Lett.* **83**, 4713 (2003).
- ⁷¹ Ya. I. Alivov, J. E. Van Nostrand, D. C. Look, M. V. Chukichev, and B. M. Ataev, "Observation of 430 nm electroluminescence from ZnO/GaN heterojunction light-emitting diodes," *Appl. Phys. Lett.* **83**, 2943 (2003).
- ⁷² Ya. I. Alivov, E. V. Kalinina, A. E. Cherenkov, D. C. Look, B. M. Ataev, A. K. Omaev, M. V. Chukichev, and D. M. Bagnall, "Fabrication and characterization of *n*-ZnO/*p*-AlGaIn heterojunction light-emitting diodes on 6H-SiC substrates," *Appl. Phys. Lett.* **83**, 4719 (2003).
- ⁷³ C. X. Wang, G. W. Yang, T. C. Zhang, H. W. Liu, Y. H. Han, J. F. Luo, C. X. Gao, and G. T. Zou, "Fabrication of transparent *p-n* heterojunction diodes by *p*-diamond film and *n*-ZnO thin film," *Diamond and Related Mater.* **12**, 1548 (2003).
- ⁷⁴ K. Ip, Y. W. Heo, D. P. Norton, S. J. Pearton, J. R. LaRoche, and F. Ren, "Zn_{0.9}Mg_{0.1}O/ZnO *p-n* junctions grown by pulsed-laser deposition," *Appl. Phys. Lett.* **85**, 1169 (2004).
- ⁷⁵ A. Osinsky, J. W. Dong, M. Z. Kauser, B. Hertog, A. M. Dabiran, P. P. Chow, S. J. Pearton, O. Lopatiuk, and L. Chernyak, "MgZnO/AlGaIn heterostructure light-emitting diodes" *Appl. Phys. Lett.* **85**, 4272 (2004).
- ⁷⁶ S. F. Chichibu, T. Ohmori, N. Shibata, T. Koyama, and T. Onuma, "Greenish-white electroluminescence from *p*-type CuGaS₂ heterojunction diodes using *n*-type ZnO as an electron injector," *Appl. Phys. Lett.* **85**, 4403 (2005).
- ⁷⁷ A. Tsukazaki, A. Ohtomo, T. Onuma, M. Ohtani, T. Makino, M. Sumiya, K. Ohtani, S. F. Chichibu, S. Fuke, Y. Segawa, H. Ohno, H. Koinuma, and M. Kawasaki, "Repeated temperature modulation epitaxy for *p*-type doping and light-emitting diode based on ZnO," *Nature Mater.* **4**, 42 (2005).
- ⁷⁸ A. Tsukazaki, M. Kubota, A. Ohtomo, T. Onuma, K. Ohtani, H. Ohno, S. F. Chichibu, and M. Kawasaki, "Blue light-emitting diode based on ZnO," *Jpn J. Appl. Phys.* **44**, L643 (2005).
- ⁷⁹ S. K. Hazra, and S. Basu, "ZnO *p-n* junctions produced by a new route," *Solid State Elec.* **49**, 1158 (2005).

BIBLIOGRAPHY

-
- ⁸⁰ H. Y. Xu, Y. C. Liu, Y. X. Liu, C. S. Xu, C. L. Shao, and R. Mu, "Ultraviolet electroluminescence from *p*-GaN/*i*-ZnO/*n*-ZnO heterojunction light-emitting diodes," Appl. Phys. B **80**, 871 (2005).
- ⁸¹ D. K. Hwang, S. H. Kang, J. H. Lim, E. J. Yang, J. Y. Oh, J. H. Yang, and S. J. Park, "*P*-ZnO/*n*-GaN heterostructure ZnO light-emitting diodes," Appl. Phys. Lett. **86**, 222101 (2005).
- ⁸² S. W. Jang, J. J. Chen, B. S. Kang, F. Ren, D. P. Norton, S. J. Pearton, J. Lopata, and W. S. Hobson, "Formation of *p-n* homojunctions in *n*-ZnO bulk single crystals by diffusion from a Zn₃P₂ source," Appl. Phys. Lett. **87**, 222113 (2005).
- ⁸³ S. Y. Lee, E. S. Shim, H. S. Kang, S. S. Pang, and J. S. Kang, "Fabrication of ZnO thin film diode using laser annealing," Thin Solid Films **473**, 31 (2005).
- ⁸⁴ C. Yuen, S. F. Yu, S. P. Lau, Rusli, and T. P. Chen, "Fabrication of *n*-ZnO:Al/*p*-SiC(4H) heterojunction light-emitting diodes by filtered cathodic vacuum arc technique," Appl. Phys. Lett. **86**, 241111 (2005).
- ⁸⁵ S. J. Jiao, Z. Z. Zhang, Y. M. Lu, D. Z. Shen, B. Yao, J. Y. Zhang, B. H. Li, D. X. Zhao, and X. W. Fan, and Z. K. Tang, "ZnO *p-n* junction light-emitting diodes fabricated on sapphire substrates," Appl. Phys. Lett. **88**, 031911 (2006).
- ⁸⁶ W. Liu, S. L. Gu, J. D. Ye, S. M. Zhu, S. M. Liu, X. Zhou, R. Zhang, Y. Shi, Y. D. Zheng, Y. Hang, and C. L. Zhang, "Blue-yellow ZnO homostructural light-emitting diode realized by metalorganic chemical-vapor deposition technique," Appl. Phys. Lett. **88**, 092101 (2006).
- ⁸⁷ M. Pan, R. Rondon, J. Cloud, V. Rengarajan, W. Nemeth, A. Valencia, J. Gomez, N. Spencer, and J. Nause, "ZnO based light-emitting diodes growth and fabrication," Proc. of SPIE **6122**, 61220M (2006).
- ⁸⁸ W. Z. Xu, Z. Z. Ye, Y. J. Zeng, L. P. Zhu, B. H. Zhao, L. Jiang, J. G. Lu, H. P. He, and S. B. Zhang, "ZnO light-emitting diode grown by plasma-assisted metal organic chemical vapor deposition," Appl. Phys. Lett. **88**, 173506 (2006).
- ⁸⁹ Y. Ryu, T. Lee, J. A. Lubguban, H. W. White, B. Kim, Y. Park, and C. Youn, "Next generation of oxide photonic devices: ZnO-based ultraviolet light-emitting diodes," Appl. Phys. Lett. **88**, 241108 (2006).
- ⁹⁰ X. Li, Y. Yan, T. A. Gessert, C. L. Perkins, D. Young, C. Dehart, M. Young, and T. J. Coutts, "Chemical-vapor deposition-formed *p*-type ZnO thin films," J. Vac. Sci. Technol. A **21**(4), 1342 (2003).
- ⁹¹ B. P. Zhang, K. Wakatsuki, N. T. Binh, N. Usami, and Y. Segawa, "Effects of growth temperature on the characteristics of ZnO epitaxial films deposited by metalorganic chemical-vapor deposition," Thin Solid Films **449**, 12 (2004).

BIBLIOGRAPHY

- ⁹² J. Dai, H. Liu, W. Fang, L. Wang, Y. Pu, and F. Jiang, "Comparisons of structural and optical properties of ZnO thin films grown on (0001) sapphire and GaN/(0001) sapphire template by atmospheric-pressure MOCVD," *Mater. Sci. Eng. B* **127**, 280 (2006).
- ⁹³ J. Ye, S. Gu, S. Zhu, T. Chen, L. Hu, F. Qin, R. Zhang, Y. Shi, and Y. Zheng, "The growth and annealing of single crystalline ZnO thin films by low-pressure MOCVD," *J. Cryst. Growth* **243**, 151 (2002).
- ⁹⁴ D. C. Look, D. C. Reynolds, C. W. Litton, R. L. Jones, D. B. Eason, and G. Cantwell, "Characterization of homoepitaxial *p*-type ZnO grown by molecular beam epitaxy," *Appl. Phys. Lett.* **81**, 1830 (2002).
- ⁹⁵ Y. Chen, D. M. Bagnall, H. J. Koh, K. T. Park, K. Hiraga, Z. Zhu, and T. Yao, "Plasma assisted molecular beam epitaxy of ZnO on *c*-plane sapphire: Growth and characterization," *J. Appl. Phys.* **84**, 3912 (1998).
- ⁹⁶ K. Nakahara, H. Takasu, P. Fons, A. Yamada, K. Iwata, K. Matsubara, R. Hunger, and S. Niki, "Growth of N-doped and Ga+N-codoped ZnO thin films by radical source molecular beam epitaxy," *J. Cryst. Growth* **237**, 503 (2002).
- ⁹⁷ N. Izyumskaya, V. Avrutin, W. Schoch, A. El-Shaer, F. Reub, Th. Grubber, and A. Waag, "Molecular beam epitaxy of high-quality ZnO using hydrogen peroxide as an oxidant," *J. Cryst. Growth* **269**, 356 (2004).
- ⁹⁸ D. Ehrentraut, H. Sato, M. Miyamoto, T. Fukada, M. Nikl, K. Maeda, and I. Niikura, "Fabrication of homoepitaxial ZnO films by low-temperature liquid-phase epitaxy," *J. Cryst. Growth* **287**, 367 (2006).
- ⁹⁹ H. Sato, D. Ehrentraut, and T. Fukuda, "Growth of $\text{Mg}_x\text{Zn}_{1-x}\text{O}/\text{ZnO}$ heterostructures by liquid phase epitaxy," *Jpn. J. Appl. Phys.* **45**, 190 (2006).
- ¹⁰⁰ S. P. Lau, H. Yang, S. F. Yu, C. Yuen, E. S. P. Leong, H. Li, and H. H. Hng, "Flexible ultraviolet random lasers based on nanoparticles," *Small* **1**, 956 (2005).
- ¹⁰¹ E. S. P. Leong and S. F. Yu, "Ultraviolet random lasing action in *p*-SiC(4H)/*i*-ZnO-SiO₂ nanocomposite/*n*-ZnO:Al heterojunction diodes," *Adv. Mater.* **18**, 1685 (2006).
- ¹⁰² E. S. P. Leong, S. F. Yu and S. P. Lau, "Directional edge-emitting UV random laser diodes," *Appl. Phys. Lett.* **89**, 221109 (2006).
- ¹⁰³ T. David, S. Goldsmith, and R. L. Boxman, "*p*-type Sb-doped ZnO thin films prepared with filtered vacuum arc deposition," [arXiv:cond-mat/0502150v1](https://arxiv.org/abs/cond-mat/0502150v1) (2005).
- ¹⁰⁴ T. David, S. Goldsmith, and R. L. Boxman, "Dependence of zinc oxide thin film properties on filtered vacuum arc deposition parameters," *J. Phys. D: Appl. Phys.* **38**, 2407 (2005).
- ¹⁰⁵ A. V. Singh, R. M. Mehra, A. Wakahara, and A. Yoshida, "*P*-type conduction in codoped ZnO thin films," *J. Appl. Phys.* **93**, 396 (2003).

BIBLIOGRAPHY

- ¹⁰⁶ E. M. C. Fortunato, Pedro M. C. Barquinha, A. C. M. B. G. Pimentel, A. M. F. Goncalves, A. J. S. Marques, L. M. N. Pereira, and R. F. P. Martins, "Fully transparent ZnO thin-film transistor produced at room temperature," *Adv. Mater.* **17**, 590 (2005).
- ¹⁰⁷ J. M. Bian, X. M. Li, X. D. Gao, W. D. Yu, and L. D. Chen, "Deposition and electrical properties of N-In codoped *p*-type ZnO thin films by ultrasonic spray pyrolysis," *Appl. Phys. Lett.* **84**, 541 (2004).
- ¹⁰⁸ R. Triboulet, and J. Perriere, "Epitaxial growth of ZnO thin films," *Prog. Cryst. Growth Charact. Mater.* **47**, 65 (2003).
- ¹⁰⁹ <http://isiwebofknowledge.com>, using keywords in topic field "ZnO AND MOCVD" and constraint the publication year to 2004, 2005 and 2006, respectively.
- ¹¹⁰ J. I. Langford, A. Boultif, J. P. Auffredic, and D. Louer, "The use of pattern decomposition to study the combined X-ray diffraction effects of crystallite size and stacking faults in ex-oxalate zinc oxide," *J. Appl. Cryst.* **26**, 22 (1993).
- ¹¹¹ G. K. Williamson and W. H. Hall, *Acta Metall.* **1**, 22 (1953).
- ¹¹² M. K. Kim, S. N. Lee, N. M. Park and S. J. Park, "Metalorganic molecular beam epitaxy of GaN thin films on a sapphire substrate," *Jpn. J. Appl. Phys.* **39**, 6170 (2000).
- ¹¹³ C. Yuen, S. F. Yu, E. S. P. Leung, H. Y. Yang, S. P. Lau and H. H. Hng, "Formation condition of random laser cavities in annealed ZnO epilayers," *IEEE J. Quantum Electron.* **41**, 970 (2005).
- ¹¹⁴ J. Tauc, *Amorphous and Liquid Semiconductors*, Plenum, London (1974).
- ¹¹⁵ E. A. David and N. F. Mott, *Phil. Mag.* **22**, 903 (1970).
- ¹¹⁶ S. T. Tan, B. J. Chen, X. W. Sun, W. J. Fan, H. S. Kwok, X. H. Zhang, and S. J. Chua, "Blueshift of optical bandgap in ZnO thin films grown by metal-organic chemical-vapor deposition," *J. Appl. Phys.* **98**, 013505 (2005).
- ¹¹⁷ J. G. Lu, Z. Z. Ye, L. Wang, J. Y. Huang and B. H. Zhao, "Structural, electrical and optical properties of N-doped ZnO thin films synthesized by SS-CVD," *Mat. Sci. Semicon. Proc.* **5**, 491 (2003).
- ¹¹⁸ S. T. Tan, B. J. Chen, X. W. Sun, X. Hu, X. H. Zhang, and S. J. Chua, "Properties of polycrystalline ZnO thin films by metal-organic chemical-vapor deposition," *J. Cryst. Growth* **281**, 571 (2005).
- ¹¹⁹ Y. Kayanuma, "Quantum-size effects of interacting electrons and holes in semiconductor microcrystals with spherical shape," *Phys. Rev. B* **38**, 9797 (1988).
- ¹²⁰ K. K. Kim, N. Koguchi, Y. W. Ok, T. Y. Seong and S. J. Park, "Fabrication of ZnO quantum dots embedded in an amorphous oxide layer," *Appl. Phys. Lett.* **84**, 3810 (2004).
- ¹²¹ S. J. Pearton, D. P. Norton, K. Ip, Y. W. Heo, T. Steiner, "Recent progress in processing and properties of ZnO," *Prog. Mater. Sci.* **50**, 293 (2005).

BIBLIOGRAPHY

-
- ¹²² G. Beni and T. M. Rice, "Theory of electron-hole liquid in semiconductors," *Phys. Rev. B* **18**, 768 (1978).
- ¹²³ Y. Arakawa, and H. Sakaki, "Multidimensional quantum well laser and temperature dependence of its threshold current," *Appl. Phys. Lett.* **40**, 939 (1982).
- ¹²⁴ J. G. Lu, Z. Z. Ye, J. Y. Huang, L. P. Zhu, B. H. Zhao, Z. L. Wang, and Sz. Fujita, "ZnO quantum dots synthesized by a vapor phase transport process," *Appl. Phys. Lett.* **88**, 063110 (2006).
- ¹²⁵ V. A. Fonoberov, K. A. Alim, A. A. Balandin, F. Xiu, and J. Liu, "Photoluminescence investigation of the carrier recombination processes in ZnO quantum dots and nanocrystals," *Phys. Rev. B* **73**, 165317 (2006).
- ¹²⁶ S. W. Kim, S. Fujita, and S. Fujita, "Self-organized ZnO quantum dots on SiO₂/Si substrates by metalorganic chemical vapor deposition," *Appl. Phys. Lett.* **81**, 5036 (2002).
- ¹²⁷ Z. W. Zhao, B. K. Tay, J. S. Chen, J. F. Hu, X. W. Sun, and S. T. Tan, "Optical properties of nanocluster-assembled ZnO thin films by nanocluster-beam deposition," *Appl. Phys. Lett.* **87**, 251912 (2005).
- ¹²⁸ D. C. Look, D. C. Reynolds, C. W. Litton, R. L. Jones, D. B. Eason, and G. Cantwell, "Characterization of homoepitaxial *p*-type ZnO grown by molecular beam epitaxy," *Appl. Phys. Lett.* **81**, 1830 (2002).
- ¹²⁹ A. B. M. A. Ashrafi, I. Suemune, H. Kumano, and S. Tanaka, "Nitrogen-doped *p*-type ZnO layers prepared with H₂O vapor-assisted metalorganic molecular-beam epitaxy," *Jpn. J. Appl. Phys.* **41**, L1281 (2002).
- ¹³⁰ Y. Zhang, B. Lin, X. Sun, and Z. Fu, "Temperature-dependent photoluminescence of nanocrystalline ZnO thin films grown on Si (100) substrates by the sol-gel process," *Appl. Phys. Lett.* **86**, 131910 (2005).
- ¹³¹ S. T. Tan, B. J. Chen, X. W. Sun, M. B. Yu, X. H. Zhang, and S. J. Chua, "Realization of intrinsic *p*-type ZnO thin films by metal-organic chemical-vapor deposition," *IEEE/TMS J. Elec. Mater.* **34**, 1172 (2005).
- ¹³² X. Wang, S. Yang, X. Yang, D. Liu, Y. Zhang, J. Wang, J. Yin, D. Liu, H. C. Ong, and G. Du, "ZnO thin film grown on silicon by metal-organic chemical vapor deposition," *J. Cryst. Growth* **243**, 13 (2002).
- ¹³³ K. K. Kim, N. Koguchi, Y. W. Ok, T. Y. Seong, and S. J. Park, "Fabrication of ZnO quantum dots embedded in an amorphous oxide layer," *Appl. Phys. Lett.* **84**, 3810 (2004).
- ¹³⁴ S. Aggarwal, A. P. Monga, S. R. Perusse, R. Ramesh, V. Ballarotto, E. D. Williams, B. R. Chalamala, Y. Wei, and R. H. Reuss, "Spontaneous ordering of oxide nanostructures," *Science* **287**, 2235 (2000).

BIBLIOGRAPHY

- ¹³⁵ S. Johnson, A. Markwitz, M. Rudolphi, and H. Baumann, "Nanostructuring of silicon (100) using electron beam rapid thermal annealing," *J. Appl. Phys.* **96**, 605 (2004).
- ¹³⁶ W. Ostwald, "On the assumed isomerism of red and yellow mercury oxide and the surface-tension of solid bodies," *Z. Phys. Chem.* **34**, 495 (1900).
- ¹³⁷ I. M. Lifshitz, and V. V. Slyozov, "The kinetics of precipitation from supersaturated solid solution," *J. Chem. Solids Phys.* **19**, 35 (1961).
- ¹³⁸ C. Wagner, *Z. Elektrochem.* **65**, 581 (1961).
- ¹³⁹ J. Alkemper, V. A. Snyder, N. Akaiwa, and P. W. Voorhees, "Dynamics of late-stage phase separation: A test of theory," *Phys. Rev. Lett.* **82**, 2725 (1999).
- ¹⁴⁰ A. J. Ardell, "The effect of volume fraction on particle coarsening: Theoretical considerations," *Acta Metall.* **20**, 61 (1972).
- ¹⁴¹ R. C. Dorward, "Precipitate coarsening during overaging of Al-Zn-Mg-Cu alloy," *Mater. Sci. Technol.* **15**, 1133 (1999).
- ¹⁴² Z. Liliental-Weber, X. W. Lin, J. Washburn, and W. Schaff, "Rapid thermal annealing of low-temperature GaAs layers," *Appl. Phys. Lett.* **66**, 2086 (1995).
- ¹⁴³ X. Weng, S. J. Clarke, W. Ye, S. Kumar, R. S. Goldman, A. Daniel, R. Clarke, J. Holt, J. Sipowska, A. Francis, and V. Rotberg, "Evolution of structural and optical properties of ion-beam synthesized GaAsN nanostructures," *J. Appl. Phys.* **92**, 4012 (2002).
- ¹⁴⁴ R. A. Bennett, D. M. Tarr, and P. A. Mulheran, "Ripening processes in supported and pinned nanoclusters – experiment, simulation and theory," *J. Phys.: Condens. Matter* **15**, S3139 (2003).
- ¹⁴⁵ Y. F. Lu, H. Q. Ni, Z. H. Mai, and Z. M. Ren, "The effects of thermal annealing on ZnO thin films grown by pulsed laser deposition," *J. Appl. Phys.* **88**, 498 (2000).
- ¹⁴⁶ J. D. Ye, S. L. Gu, F. Qin, S. M. Zhou, S. M. Liu, X. Zhou, W. Liu, L. Q. Hu, R. Zhang, Y. Shi, Y. D. Zheng, and Y. D. Ye, "MOCVD growth and properties of ZnO thin films using dimethylzinc and oxygen," *Appl. Phys. A* **81**, 809 (2004).
- ¹⁴⁷ Y. T. Zhang, G. T. Du, X. Q. Wang, W. C. Li, X. T. Yang, Y. Ma, B. J. Zhao, H. J. Yang, D. L. Liu, and S. R. Yang, "X-ray photoelectron spectroscopy study of ZnO thin films grown by metal-organic chemical vapor deposition," *J. Cryst. Growth* **252**, 180 (2003).
- ¹⁴⁸ M. Ohring, *Materials Science of Thin Films: Deposition and Structure*, 2nd ed. (Academic Press, San Diego, 2001), pp. 386-400.
- ¹⁴⁹ P. Wynblatt, and N. A. Gjostein, "Particle growth in model supported metal-catalysts, 1. Theory," *Acta Metall.* **24**, 1165 (1976).
- ¹⁵⁰ K. M. Unruh, T. E. Huber, and C. A. Huber, "Melting and freezing behavior of indium metal in porous glasses," *Phys. Rev. B* **48**, 9021 (1993).

BIBLIOGRAPHY

-
- ¹⁵¹ S. L. Lai, J. Y. Guo, V. Petrova, G. Ramanath, and L. H. Allen, "Size-dependent melting properties of small tin particles: Nanocalorimetric measurements," *Phys. Rev. Lett.* **77**, 99 (1996).
- ¹⁵² B. D. Yao, Y. F. Chan, and N. Wang, "Formation of ZnO nanostructures by a simple way of thermal evaporation," *Appl. Phys. Lett.* **81**, 757 (2002).
- ¹⁵³ C. X. Xu and X. W. Sun, "Field emission from zinc oxide nanopins," *Appl. Phys. Lett.* **83**, 3806 (2003).
- ¹⁵⁴ G. W. Tomlins, J. L. Routbort, and T. O. Mason, "Zinc self-diffusion, electrical properties, and defect structure of undoped, single crystal zinc oxide," *J. Appl. Phys.* **87**, 117 (2000).
- ¹⁵⁵ A. Krost, J. Christen, N. Oleynik, A. Dadgar, S. Deiter, J. Blasing, A. Krtischil, D. Forster, F. Bertram, and A. Diez, "Ostwald ripening and flattening of epitaxial ZnO layers during *in situ* annealing in metalorganic vapor phase epitaxy," *Appl. Phys. Lett.* **85**, 1496 (2004).
- ¹⁵⁶ S. B. Zhang, S. H. Wei, and Alex Zunger, "Intrinsic *n*-type versus *p*-type doping asymmetry and the defect physics of ZnO," *Phys. Rev. B* **63**, 075205 (2001).
- ¹⁵⁷ Chris G. Van de Walle, "Defect analysis and engineering in ZnO," *Physica B* **308-310**, 899 (2001).
- ¹⁵⁸ Anderson Janotti, and Chris G. Van de Walle, "Oxygen vacancies in ZnO," *Appl. Phys. Lett.* **87**, 122102 (2005).
- ¹⁵⁹ Chris G. Van de Walle, "Hydrogen as a cause of doping in zinc oxide," *Phys. Rev. Lett.* **85**, 1012 (2000).
- ¹⁶⁰ Z. Q. Chen, S. Yamamoto, M. Maekawa, A. Kawasuso, X. L. Yuan, and T. Sekiguchi, J. "Postgrowth annealing of defects in ZnO studied by positron annihilation, x-ray diffraction, Rutherford backscattering, cathodoluminescence, and Hall measurements," *Appl. Phys.* **94**, 4807 (2003).
- ¹⁶¹ H. S. Kang, J. S. Kang, J. W. Kim, and S. Y. Lee, "Annealing effect on the property of ultraviolet and green emissions of ZnO thin films," *J. Appl. Phys.* **95**, 1246 (2004).
- ¹⁶² G. F. Neumark, "Achievement of well conducting wide bandgap semiconductors: Role of solubility and nonequilibrium impurity incorporation," *Phys. Rev. Lett.* **62**, 1800 (1989).
- ¹⁶³ A. Kobayashi, O. F. Sankey, and John D. Dow, "Deep energy levels of defects in the wurtzite semiconductors AlN, CdS, CdSe, ZnS, and ZnO," *Phys. Rev. B* **28**, 946 (1983).
- ¹⁶⁴ A. Valentini, F. Quaranta, M. Rossi, and G. Battaglin, "Preparation and characterization of Li-doped ZnO thin films," *J. Vac. Sci. Technol. A* **9**, 286 (1991).
- ¹⁶⁵ D. C. Look, D. C. Reynolds, C. W. Litton, R. L. Jones, D. B. Eason, and G. Cantwell, "Characterization of homoepitaxial *p*-type ZnO grown by molecular beam epitaxy," *Appl. Phys. Lett.* **81**, 1830 (2002).

BIBLIOGRAPHY

-
- ¹⁶⁶ E. -C. Lee and K. J. Chang, "Possible *p*-type doping with group-I elements in ZnO," Phys. Rev. B **70**, 115210 (2004).
- ¹⁶⁷ M. G. Wardle, J. P. Goss, and P. R. Briddon, "Theory of Li in ZnO: A limitation for Li-based *p*-type doping," Phys. Rev. B **71**, 155205 (2005).
- ¹⁶⁸ E.-C. Lee, Y.-S. Kim, Y.-G. Jin, and K. J. Chang, "Compensation mechanism for N acceptors in ZnO," Phys. Rev. B **64**, 085120 (2001).
- ¹⁶⁹ K. Minegishi, Y. Koiwai, Y. Kikuchi, K. Yano, M. Kasuga, and A. Shimizu, "Growth of *p*-type zinc oxide films by chemical vapor deposition," Jpn. J. Appl. Phys. **36**, L1453 (1997).
- ¹⁷⁰ T. Yamamoto, and H. Katayama-Yoshida, "Solution using a codoping method to unipolarity for the fabrication of *p*-type ZnO," Jpn. J. Appl. Phys. **38**, L166 (1999).
- ¹⁷¹ T. Yamamoto, and H. Katayama-Yoshida, "Physics and control of valence states in ZnO by codoping method," Physica B **302-303**, 155 (2000).
- ¹⁷² T. Yamamoto, "Codoping for the fabrication of *p*-type ZnO," Thin Solid Films **420**, 100 (2002).
- ¹⁷³ K. K. Kim, H. S. Kim, D. K. Hwang, H. H. Lim, and S. J. Park, "Realization of *p*-type ZnO thin films via phosphorus doping and thermal activation of the dopant," Appl. Phys. Lett. **83**, 63 (2003).
- ¹⁷⁴ Y. R. Ryu, T. S. Lee, and H. W. White, "Properties of arsenic-doped *p*-type ZnO grown by hybrid beam deposition," Appl. Phys. Lett. **83**, 87 (2003).
- ¹⁷⁵ D. C. Look, G. M. Renlund, R. H. Burgener II, and J. R. Sizelove, "As-doped *p*-type ZnO produced by an evaporation/sputtering process," Appl. Phys. Lett. **85**, 5269 (2006).
- ¹⁷⁶ S. Limpijumnong, S. B. Zhang, S.-H. Wei, and C. H. Park, "Doping by large-size-mismatched impurities: The microscopic origin of arsenic- or antimony-doped *p*-type zinc oxide," Phys. Rev. Lett. **92**, 155504 (2004).
- ¹⁷⁷ U. Wahl, E. Rita, J. G. Correia, A. C. Marques, E. Alves, and J. C. Soares, "Direct evidence for As as a Zn-site impurity in ZnO," Phys. Rev. Lett. **95**, 215503 (2005).
- ¹⁷⁸ V. Vaithianathan, B. -T. Lee, K. Asokan, and S. S. Kim, "Characterization of As-doped, *p*-type ZnO by x-ray absorption near-edge structure spectroscopy," Appl. Phys. Lett. **88**, 112103 (2006).
- ¹⁷⁹ F. X. Xiu, Z. Yang, L. J. Mandalapu, D. T. Zhao, J. L. Liu, and W. P. Beyermann, "High-mobility Sb-doped *p*-type ZnO by molecular-beam epitaxy," Appl. Phys. Lett. **87**, 152101 (2005).
- ¹⁸⁰ E. C. Lee, Y. S. Kim, Y. G. Jin, and K. J. Chang, "Compensation mechanism for N acceptors in ZnO," Phys. Rev. B **64**, 085120 (2001).

BIBLIOGRAPHY

-
- ¹⁸¹ T. V. Butkhuzi, A. V. Bureyev, A. N. Georgobiani, N. P. Kekelidze, and T. G. Khulordava, "Optical and electrical properties of radical beam gettering epitaxy grown *n*- and *p*-type ZnO single crystals," *J. Crys. Growth* **117**, 366 (1992).
- ¹⁸² A. N. Georgobiani, M. B. Kotlyarevskii, V. V. Kidalov, L. S. Lepnev, and I. V. Rogozin, "Luminescence of native-defect *p*-type ZnO," *Inorg. Mater.* **37**, 1095 (2001).
- ¹⁸³ G. Xiong, J. Wilkinson, B. Mischuck, S. Tuzemen, K. B. Ucer, and R. T. Williams, "Control of *p*- and *n*-type conductivity in sputter deposition of undoped ZnO," *Appl. Phys. Lett.* **80**, 1195 (2002).
- ¹⁸⁴ Y. Ma, G. T. Du, S. R. Yang, Z. T. Li, B. J. Zhao, X. T. Yang, T. P. Yang, Y. T. Zhang, and D. L. Liu, "Control of conductivity type in undoped ZnO thin films grown by metalorganic vapor phase epitaxy," *J. Appl. Phys.* **95**, 6268 (2004).
- ¹⁸⁵ K. Minegishi, Y. Koiwai, Y. Kikuchi, K. Yano, M. Kasuga, and A. Shimizu, "Growth of *p*-type zinc oxide films by chemical vapor deposition," *Jpn. J. Appl. Phys.* **36**, L1453 (1997).
- ¹⁸⁶ M. Joseph, H. Tabata, and T. Kawai, "*P*-type electrical conduction in ZnO thin films by Ga and N codoping," *Jpn. J. Appl. Phys.* **38**, L1205 (1999).
- ¹⁸⁷ X. L. Guo, H. Tabata, and T. Kawai, "Pulsed laser reactive deposition of *p*-type ZnO thin film enhanced by an electron cyclotron resonance source," *J. Crys. Growth* **223**, 135 (2001).
- ¹⁸⁸ Y. R. Ryu, S. Zhu, D. C. Look, J. M. Wrobel, H. M. Jeong, and H. W. White, "Synthesis of *p*-type ZnO thin films," *J. Crys. Growth* **216**, 330 (2002).
- ¹⁸⁹ B. S. Li, Y. C. Liu, Z. Z. Zhi, D. Z. Shen, Y. M. Lu, J. Y. Zhang, X. W. Fan, R. X. Mu, and Don O. Henderson, "Optical properties and electrical characterization of *p*-type ZnO thin films prepared by thermally oxidizing Zn₃N₂ thin films," *J. Mater. Res.* **18**, 1 (2003).
- ¹⁹⁰ A. V. Singh, R. M. Mehra, A. Wakahara, and Yoshida, "*P*-type conduction in codoped ZnO thin films," *J. Appl. Phys.* **93**, 396 (2003).
- ¹⁹¹ J. G. Lu, Z. Z. Ye, L. Wang, J. Y. Huang, and B. H. Zhao, "Structural, electrical and optical properties of N-doped ZnO thin films synthesized by SS-CVD," *Mat. Sci. Semicon. Proc.* **5**, 491 (2003).
- ¹⁹² J. G. Lu, Y. Z. Zhang, Z. Z. Ye, L. Wang, B. H. Zhao, and J. Y. Huang, "*P*-type ZnO thin films deposited by DC reactive magnetron sputtering at different ammonia concentrations," *Matt. Lett.* **57**, 3311 (2003).
- ¹⁹³ X. Li, Y. Yan, T. A. Gessert, C. L. Perkins, D. Young, C. DeHart, M. Young, and T. J. Coutts, "Chemical vapor deposition-formed *p*-type ZnO thin films," *J. Vac. Sci. Technol. A* **21**(4), 1342 (2003).

BIBLIOGRAPHY

-
- ¹⁹⁴ W. Z. Xu, Z. Z. Ye, T. Zhou, B. H. Zhao, L. P. Zhu, and J. Y. Huang, "Low-pressure MOCVD growth of *p*-type ZnO thin films by using NO as the dopant source," *J. Cryst. Growth* **265**, 133 (2004).
- ¹⁹⁵ Z. Z. Ye, Z. G. Fei, J. G. Lu, Z. H. Zhang, L. P. Zhu, B. H. Zhao, and J. Y. Huang, "Preparation of *p*-type ZnO thin films by Al + N-codoping method," *J. Cryst. Growth* **265**, 127 (2004).
- ¹⁹⁶ C. Y. Zhang, X. M. Li, J. M. Bian, W. D. Yu, and X. D. Gao, "Structural and electrical properties of nitrogen and aluminum codoped *p*-type ZnO thin films," *Solid State Commun.* **132**, 75 (2004).
- ¹⁹⁷ J. M. Bian, X. M. Li, X. D. Gao, W. D. Yu, and L. D. Chen, "Deposition and electrical properties of N-In codoped *p*-type ZnO thin films by ultrasonic spray pyrolysis," *Appl. Phys. Lett.* **84**, 541 (2004).
- ¹⁹⁸ S. J. So, and C. B. Park, "Diffusion of phosphorus and arsenic using ampoule-tube method on undoped ZnO thin films and electrical and optical properties of *p*-type ZnO thin films," *J. Cryst. Growth* **285**, 606 (2005).
- ¹⁹⁹ V. Vaithianathan, B. T. Lee, and S. S. Kim, "Pulsed-laser-deposited *p*-type ZnO thin films with phosphorus doping," *J. Appl. Phys.* **98**, 043519 (2005).
- ²⁰⁰ F. X. Xiu, Z. Yang, L. J. Mandalapu, D. T. Zhao, and J. L. Liu, "Photoluminescence study of Sb-doped *p*-type ZnO thin films by molecular-beam epitaxy," *Appl. Phys. Lett.* **87**, 252102 (2005).
- ²⁰¹ G. Braunstein, A. Muraviev, H. Saxena, N. Dhere, V. Richter, and R. Kalish, "*P*-type doping of zinc oxide by arsenic ion implantation," *Appl. Phys. Lett.* **87**, 192103 (2005).
- ²⁰² G. T. Du, Y. Ma, Y. T. Zhang, and T. P. Yang, "Preparation of intrinsic and N-doped *p*-type thin films by metalorganic vapor phase epitaxy," *Appl. Phys. Lett.* **87**, 213103 (2005).
- ²⁰³ F. G. Chen, Z. Z. Ye, W. Z. Xu, B. H. Zhao, L. P. Zhu, and J. G. Lv, "Fabrication of *p*-type ZnO thin films via MOCVD method by using phosphorus as dopant source," *J. Cryst. Growth* **281**, 458 (2005).
- ²⁰⁴ D. K. Hwang, H. S. Kim, J. H. Lim, J. Y. Oh, J. H. Yang, S. J. Park, K. K. Kim, D. C. Look, and Y. S. Park, "Study of the photoluminescence of phosphorus-doped *p*-type ZnO thin films grown by radio-frequency magnetron sputtering," *Appl. Phys. Lett.* **86**, 151917 (2005).
- ²⁰⁵ Y. J. Zeng, Z. Z. Ye, W. Z. Xu, L. L. Chen, D. Y. Li, L. P. Zhu, B. H. Zhao, and Y. L. Hu, "Realization of *p*-type ZnO thin films via monodoping of Li acceptor," *J. Cryst. Growth* **283**, 180 (2005).

BIBLIOGRAPHY

-
- ²⁰⁶ Y. J. Zeng, Z. Z. Ye, W. Z. Xu, D. Y. Li, J. G. Lu, L. P. Zhu, and B. H. Zhao, "Dopant source choice for formation of *p*-type ZnO:Li acceptor," Appl. Phys. Lett. **88**, 062107 (2006).
- ²⁰⁷ C. Wang, Z. G. Ji, J. H. Xi, J. Du, and Z. Z. Ye, "Fabrication and characteristics of the low-resistive *p*-type ZnO thin films by DC reactive magnetron sputtering," Mater. Lett. **60**, 912 (2006).
- ²⁰⁸ S. J. Jiao, Z. Z. Zhang, Y. M. Lu, D. Z. Shen, B. Yao, J. Y. Zhang, B. H. Li, D. X. Zhao, X. W. Fan, and Z. K. Tang, "ZnO *p-n* junction light-emitting diodes fabricated on sapphire substrates," Appl. Phys. Lett. **88**, 031911 (2006).
- ²⁰⁹ Z. G. Yu, P. Wu, and H. Gong, "Control of *p*- and *n*-type conductivities in P doped ZnO thin films by using radio-frequency sputtering," Appl. Phys. Lett. **88**, 132114 (2006).
- ²¹⁰ P. Wang, N. Chen, and Z. G. Yin, "P-doped *p*-type ZnO thin films deposited on Si substrate by radio-frequency magnetron sputtering," Appl. Phys. Lett. **88**, 152102 (2006).
- ²¹¹ Y. Nakano, T. Morikawa, T. Ohwaki, and Y. Taga, "Electrical characterization of *p*-type N-doped ZnO thin films prepared by thermal oxidation of sputtered Zn₃N₂ films," Appl. Phys. Lett. **88**, 172103 (2006).
- ²¹² H. S. Kang, B. D. Ahn, J. H. Kim, G. H. Kim, S. H. Lim, H. W. Chang, and S. Y. Lee, "Structural, electrical, and optical properties of *p*-type ZnO thin films with Ag dopant," Appl. Phys. Lett. **88**, 202108 (2006).
- ²¹³ J. G. Lu, Y. Z. Zhang, Z. Z. Ye, L. P. Zhu, L. Wang, B. H. Zhao, and Q. L. Liang, "Low-resistivity, stable *p*-type ZnO thin films realized using a Li-N dual-acceptor doping method," Appl. Phys. Lett. **88**, 222114 (2006).
- ²¹⁴ Y. Cao, L. Miao, S. Tanemura, M. Tanemura, Y. Kuno, and Y. Hayashi, "Low resistivity *p*-ZnO thin films fabricated by sol-gel spin coating," Appl. Phys. Lett. **88**, 251116 (2006).
- ²¹⁵ Y. J. Zeng, Z. Z. Ye, W. Z. Xu, J. G. Lu, H. P. He, L. P. Zhu, B. H. Zhao, Y. Che, and S. B. Zhang, "*P*-type behavior in nominally undoped ZnO thin films by oxygen plasma growth," Appl. Phys. Lett. **88**, 262103 (2006).
- ²¹⁶ G. Hu, H. Gong, E. F. Chor, and P. Wu, "ZnO homojunctions grown by cosputtering ZnO and Zn₃P₂ targets," Appl. Phys. Lett. **89**, 021112 (2006).
- ²¹⁷ J. G. Lu, Y. Z. Zhang, Z. Z. Ye, Y. J. Zeng, H. P. He, L. P. Zhu, J. Y. Huang, L. Wang, J. Yuan, B. H. Zhao, and X. H. Li, "Control of *p*- and *n*-type conductivities in Li-doped ZnO thin films," Appl. Phys. Lett. **89**, 112113 (2006).
- ²¹⁸ M. Kumar, T. -H. Kim, S. -S. Kim, and B. -T. Lee, "Growth of epitaxial *p*-type ZnO thin films by codoping of Ga and N," Appl. Phys. Lett. **89**, 112103 (2006).
- ²¹⁹ H. Matsui, H. Saeki, T. Kawai, H. Tabata, and B. Mizobuchi, "N doping using N₂O and NO sources: From the viewpoint of ZnO," J. Appl. Phys. **95**, 5882 (2004).

BIBLIOGRAPHY

-
- ²²⁰ K. Nakahara, H. Takasu, P. Fons, A. Yamada, K. Iwata, K. Matsubara, R. Hunger, S. Niki, "Growth of N-doped and Ga plus N-codoped ZnO thin films by radical source molecular beam epitaxy," *J. Cryst. Growth* **237**, 503 (2002).
- ²²¹ X. Q. Wang, S. R. Yang, J. Z. Wang, M. T. Li, X. Y. Jiang, G. T. Du, X. Liu, R. P. H. Chang, "Nitrogen doped ZnO thin film grown by the plasma-assisted metal-organic chemical vapor deposition," *J. Cryst. Growth* **226**, 123 (2001).
- ²²² I. Ozerov, M. Arab, V. I. Safarov, W. Marine, S. Giorgio, M. Sentis, L. Nanai, "Enhancement of exciton emission from ZnO nanocrystalline films by pulsed laser annealing," *Appl. Surface Sci.* **226**, 242 (2004).
- ²²³ Y. M. Strzhemechny, J. Nemergut, P. E. Smith, J. Bae, D. C. Look, L. J. Brillson, "Remote hydrogen plasma processing of ZnO single crystal surfaces," *J. Appl. Phys.* **94**, 4256 (2003).
- ²²⁴ X. Li, S. E. Asher, S. Limpijumnong, S. B. Zhang, S. -H. Wei, T. M. Barnes, T. J. Coutts, and R. Noufi, "Unintentional doping and compensation effects of carbon in metal-organic chemical-vapor deposition fabricated ZnO thin films," *J. Vac. Sci. Technol. A* **24**, 1213 (2006).
- ²²⁵ S. T. Tan, X. W. Sun, X. H. Zhang, S. J. Chua, B. J. Chen and C. C. Teo, "Cluster coarsening in zinc oxide thin films by post-growth annealing," *J. Appl. Phys.* **100**, 033502 (2006).
- ²²⁶ D. C. Look, "Electrical and optical properties of *p*-type ZnO," *Semicond. Sci. Technol.* **20**, S55 (2005).
- ²²⁷ C. -M. Pradier, C. Hinnen, K. Jansson, L. Dahl, M. Nygren, and A. Flodstrom, "Structural and surface characterization of perovskite-type oxides; influence of A and B substitutions upon oxygen binding energy," *J. Mater. Sci.* **33**, 3187 (1998).
- ²²⁸ Y. W. Heo, K. Ip, S. J. Pearton, and D. P. Norton, "The near band-edge emission and photoconductivity response of phosphorus-doped ZnO thin films grown by pulsed laser deposition," *Phys. Stat. Sol. A* **201**, 1500 (2004).
- ²²⁹ A. Teke, U. Ozgur, S. Dogan, X. Gu, H. Morkoc, B. Nemeth, J. Nause, and H. O. Everitt, "Excitonic fine structure and recombination dynamics in single-crystal ZnO," *Phys. Rev. B* **70**, 195207 (2004).
- ²³⁰ B. K. Meyer, H. Alves, D. M. Hofmann, W. Kriegseis, D. Forster, F. Bertram, J. Christen, A. Hoffmann, M. Starbburg, M. Dworzak, U. Haboeck, and A. V. Rodina, "Bound exciton and donor-acceptor pair recombinations in ZnO," *Phys. Stat. Sol. b* **241**, 231 (2004).
- ²³¹ D. C. Reynolds, D. C. Look, B. Jogai, C. W. Litton, T. C. Collins, W. Harsch, and G. Cantwell, "Neutral-donor-bound-exciton complexes in ZnO crystals," *Phys. Rev. B* **57**, 12151 (1998).

BIBLIOGRAPHY

-
- ²³² C. X. Xu, X. W. Sun, Z. L. Dong and M. B. Yu, "Zinc oxide nanodisk," *Appl. Phys. Lett.* **85**, 3878 (2004).
- ²³³ Z. Y. Jiang, Z. X. Xie, X. H. Zhang, S. C. Lin, T. Xu, S. Y. Xie, R. B. Huang and L. S. Zheng, "Synthesis of single-crystalline ZnO polyhedral submicrometer-sized hollow beads using laser-assisted growth with ethanol droplets as soft templates," *Adv. Mater.* **16**, 904 (2004).
- ²³⁴ P. X. Gao and Z. L. Wang, "Mesoporous polyhedral cages and shells formed by textured self-assembly of ZnO nanocrystals," *J. Am. Chem. Soc.* **125**, 11299 (2003).
- ²³⁵ Y. J. Chen, Q. H. Li, Y. X. Liang, T. H. Wang, Q. Zhao and D. P. Yu, "Field-emission from long SnO₂ nanobelt arrays," *Appl. Phys. Lett.* **85**, 5682 (2004).
- ²³⁶ L. Shi, Q. Hao, C. Yu, N. Mingo, X. Kong and Z. L. Wang, "Thermal conductivities of individual tin dioxide nanobelts," *Appl. Phys. Lett.* **84**, 2638 (2004).
- ²³⁷ C. H. Liang, G. W. Meng, G. Z. Wang, Y. W. Wang, L. D. Zhang and S. Y. Zhang, "Catalytic synthesis and photoluminescence of β -Ga₂O₃ nanowires," *Appl. Phys. Lett.* **78**, 3202 (2001).
- ²³⁸ X. Liu, C. Li, S. Han, J. Han and C. Zhou, "Synthesis and electronic transport studies of CdO nanoneedles," *Appl. Phys. Lett.* **82**, 1950 (2003).
- ²³⁹ S. W. Kim, S. Fujita, and S. Fujita, "Self-organized ZnO quantum dots on SiO₂/Si substrates by metalorganic chemical vapor deposition," *Appl. Phys. Lett.* **81**, 5036 (2002).
- ²⁴⁰ Z. W. Zhao, B. K. Tay, J. S. Chen, J. F. Hu, X. W. Sun, and S. T. Tan, "Optical properties of nanocluster-assembled ZnO thin films by nanocluster-beam deposition," *Appl. Phys. Lett.* **87**, 251912 (2005).
- ²⁴¹ X. H. Zhang, S. J. Chua, A. M. Yong, S. Y. Chow, H. Y. Yang, S. P. Lau, and S. F. Yu, "Exciton radiative lifetime in ZnO quantum dots embedded in SiO_x matrix," *Appl. Phys. Lett.* **88**, 221903 (2006).
- ²⁴² V. A. Fonoberov, K. A. Alim, A. A. Balandin, F. Xiu, and J. Liu, "Photoluminescence investigation of the carrier recombination processes in ZnO quantum dots and nanocrystals," *Phys. Rev. B* **73**, 165317 (2006).
- ²⁴³ C. X. Xu and X. W. Sun, "Field emission from zinc oxide nanopins," *Appl. Phys. Lett.* **83**, 3806 (2003).
- ²⁴⁴ C. X. Xu, X. W. Sun, Z. L. Dong, S. T. Tan, Y. P. Cui, and B. P. Wang, "Manganese-doped zinc oxide tetrahedra and their photoluminescent properties," *J. Appl. Phys.* **98**, 113513 (2005).
- ²⁴⁵ Z. W. Pan, Z. R. Dai, and Z. L. Wang, "Nanobelts of semiconducting oxides," *Science* **291**, 1947 (2001).

BIBLIOGRAPHY

- ²⁴⁶ Z. L. Wang, and J. H. Song, "Piezoelectric nanogenerators based on zinc oxide nanowire arrays," *Science* **312**, 242 (2006).
- ²⁴⁷ W. I. Park, G. C. Yi, M. Y. Kim and S. J. Pennycook, "Quantum confinement observed in ZnO/ZnMgO nanorod heterostructures," *Adv. Mater.* **15**, 526 (2003).
- ²⁴⁸ B. P. Zhang, N. T. Binh, K. Wakatsuki, C. Y. Liu, Y. Segawa and N. Usami, "Growth of ZnO/MgZnO quantum wells on sapphire substrates and observation of the two-dimensional confinement effect," *Appl. Phys. Lett.* **86**, 032105 (2005).
- ²⁴⁹ Th. Gruber, C. Kirchner, P. Kling, and F. Reuss, "ZnMgO epilayers and ZnO – ZnMgO quantum wells for optoelectronic applications in the blue and UV spectra region," *Appl. Phys. Lett.* **84**, 5359 (2004).
- ²⁵⁰ Y. H. Leung, K. H. Tam, A. B. Djuricic, M. H. Xie, W. K. Chan, D. Lu and W. K. Ge, "ZnO nanoshells: Synthesis, structure, and optical properties," *J. Cryst. Growth* **283**, 134 (2005).
- ²⁵¹ M. Mo, Jimmy C. Yu, L. Zhang and S-K. A. Li, "Self-assembly of ZnO nanorods and nanosheets into hollow microhemispheres and microspheres," *Adv. Mater.* **17**, 756 (2005).
- ²⁵² X. Xia, L. Zhu, Z. Ye, G. Yuan, B. Zhao and Q. Qian, "Novel ZnO micoballs synthesized via pyrolysis of zinc-acetate in oxygen atmosphere," *J. Cryst. Growth* **282**, 506 (2005).
- ²⁵³ W. I. Park, D. H. Kim, and G. C. Yi, "Metalorganic vapor-phase epitaxial growth of vertically well-aligned ZnO nanorods," *Appl. Phys. Lett.* **80**, 4232 (2002).
- ²⁵⁴ W. I. Park, G. C. Yi, M. Kim, and S. J. Pennycook, "ZnO nanoneedles grown vertically on Si substrates by non-catalytic vapor-phase epitaxy," *Adv. Mater.* **14**, 1841 (2002).
- ²⁵⁵ J. Zhong, G. Saraf, S. Muthukumar, H. Chen, Y. Chen, and Y. Lu, "ZnO nanotips grown on silicon substrates by metal-organic chemical-vapor deposition," *IEEE/TMS J. Elec. Mater.* **33**, 654 (2004).
- ²⁵⁶ S. Muthukumar, H. Sheng, J. Zhong, Z. Zhang, N. W. Emanetoglu, and Y. Lu, "Selective MOCVD growth of ZnO nanotips," *IEEE T. Nanotechnol.* **2**, 1536 (2003).
- ²⁵⁷ M. C. Jeong, B. Y. Oh, O. H. Nam, T. Kim, and J. M. Myoung, "Three-dimensional ZnO hybrid nanostructures for oxygen sensing application," *Nanotechnology* **17**, 526 (2006).
- ²⁵⁸ X. Y. Kong, Y. Ding, and Z. L. Wang, "Metal-semiconductor Zn-ZnO core-shell nanobelts and nanotubes," *J. Phys. Chem. B* **108**, 570 (2004).